Topological Analysis of Patterns

A Thesis
Presented to
The Academic Faculty

by

Marcio Fuzeto Gameiro

In Partial Fulfillment
of the Requirements for the Degree
Doctor of Philosophy

School of Mathematics
Georgia Institute of Technology
August 2005

Topological Analysis of Patterns

Approved by:

Dr. Konstantin Mischaikow, Advisor
School of Methematics
Georgia Institute of Technology

Dr. Michael Schatz
School of Physics
Georgia Institute of Technology

Dr. Luca Dieci
School of Methematics
Georgia Institute of Technology

Dr. Andrzej Szymczak
College of Computing
Georgia Institute of Technology

Dr. Guillermo Goldsztein
School of Methematics
Georgia Institute of Technology

Date Approved: June 13, 2005

DEDICATION

To Daniel.

ACKNOWLEDGEMENTS

First and foremost I would like to thank Konstantin for all his help and patience. Besides being a great advisor, he always gave me a great amount of advice and encouragement whenever I needed.

I would not be here today if it were not for Hildebrando Rodrigues. In addition to being a great M.S. advisor he was the first one to encourage me to come to Georgia Tech, and gave me tremendous help to achieve such a goal. For him I have special thanks. It was only through his efforts combined with the help of Konstantin and Jack Hale, that it was possible for me to come to Georgia Tech. I will always be indebted to them.

Also back in Brazil I would like to thank Alexandre and Gaspar for the great amount of help and incentive during my stay at the ICMC-USP.

I would like to thank the following people with whom I had the pleasure to work and the opportunity to learn from: Bill Kalies, Tom Wanner, Kapil Krishan, Michael Schatz, Erik Boczko, and Pete Manolios.

I owe many thanks to Bill Kalies and Pawel Pilarczyk for providing the homology programs used in this thesis, as well as helping me to learn how to use them.

I also want to thank all my friends at Tech. In special I would like to mention Jorge, Jose Luiz, Suleyman, and Kapil.

Many special thanks go to Eliane for understanding (almost always, with respect to some measure) that I had to work when I should be expending time with her and Daniel, and for all the help she gave me. The ways in which she helped me are too many to list here.

Finally I would like to thank CAPES, Brazil, for the financial support during my Ph.D.

TABLE OF CONTENTS

LIST OF FIGURES

SUMMARY

We use computational homology to characterize the geometry of complicated time-dependent patterns. Homology provides very basic topological (geometrical) information about the patterns, such as the number of components (pieces) and the number of holes. For 3-dimensional patterns it also provides the number of voids. We apply these techniques to patterns generated by experiments on spiral defect chaos, as well as to numerically simulated patterns in the Cahn-Hilliard theory of phase separation and on spiral wave patterns in excitable media. These techniques allow us to distinguish patterns at different parameter values, to detect complicated dynamics through the computation of positive Lyapunov exponents and entropies, to compare experimental data with numerical simulations, to quantify boundary effects on finite size domains, among other things.

CHAPTER I

INTRODUCTION

As the title says, this thesis is about patterns. So it seems appropriate to start it by discussing patterns, but rather than trying to explain or define what a pattern is, let us *look* at some patterns: Figures 1, 2, and 3 show some examples. For the moment it is not important what these patterns mean or how they are produced (this will be discussed latter). For now let us just assume we have the ability to produce such patterns. They may be produced in a laboratory by means of an experiment (as is the case of Figure 1), or by numerical simulations of differential equations (as is the case of Figures 2, and 3), or by any other means.

Figure 1: Spiral defect chaos patterns.

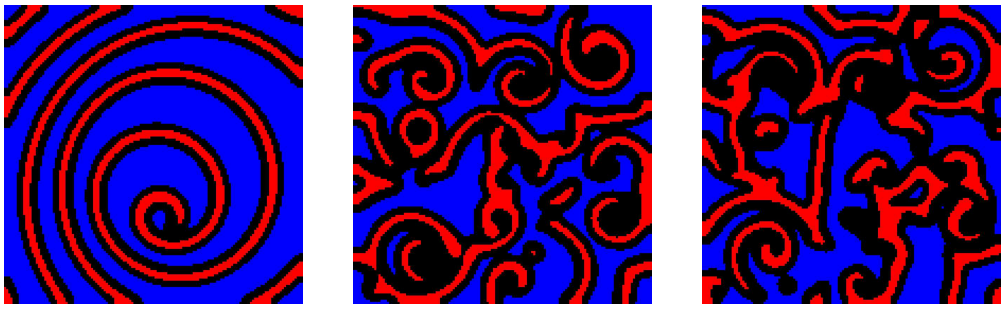

Figure 2: Spiral wave patterns in excitable media.

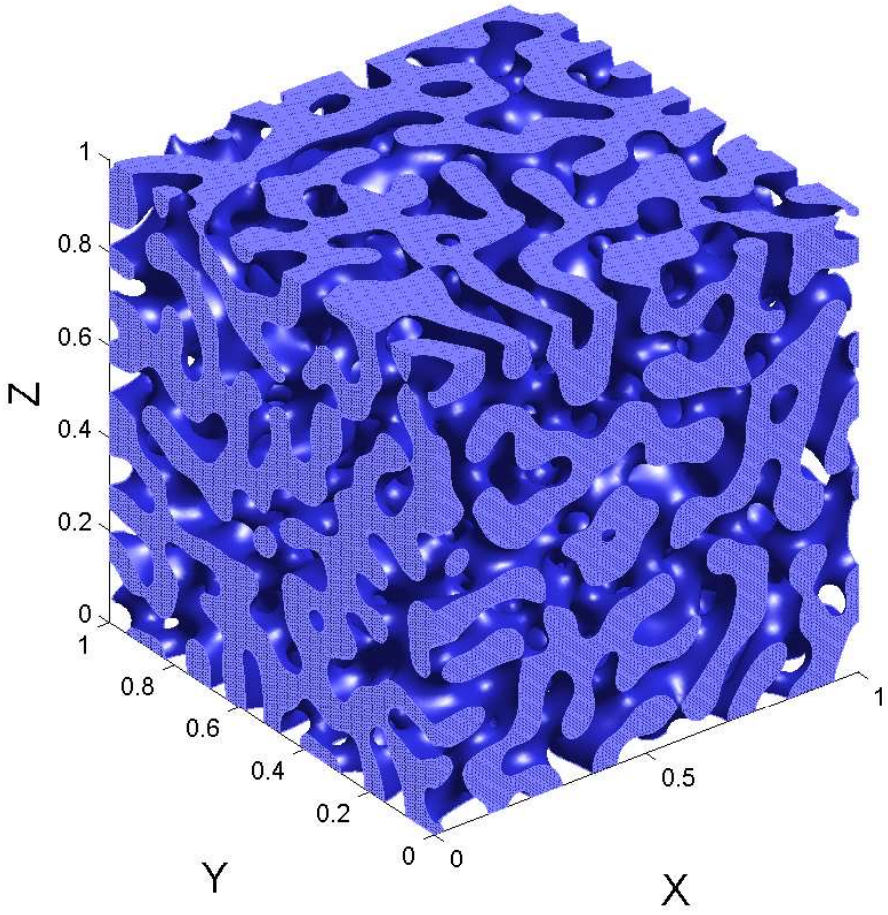

Figure 3: Patterns generated by the Cahn-Hilliard model.

Once again, as the title says, this thesis is about *analysis* of patterns. It means we do not want to just produce these nice looking pictures, but we want to analyze them (learn something from them). The process of generating patterns as shown above can be seen as a way of expressing (usually in a reduced form) the information produced by the underlying system. In general these patterns carry a great amount of information, and so are extremely useful to understand the dynamics of the system. The problem is that, in most cases, the quantity of information in such patterns is too great to be amenable to direct analysis. Therefore it is necessary to reduce the amount of information while still preserving enough information to allow one to draw interesting conclusions about the original system.

One of the simplest nontrivial set of information one can extract from patterns is some very basic

topological (geometrical) information such as the number of components (pieces) and the number of holes (tunnels for 3-dimensional patterns). This is exactly what *homology* does. So in this thesis we propose to use homology to extract these basic topological informations from the patterns, and use this information to draw conclusions about the dynamics of the system. As we are going to see in the remaining of the thesis, in many cases this reduced set of topological information still preserves enough information to allow one to draw interesting conclusions about the underlying system.

At this point one might ask: Why use homology (whatever that is) when all we want to do is something as trivial as counting the number of components and holes? The answer is threefold: (1) While it is true that for 2-dimensional patterns one could do this simply by visual inspection, for more complicated 3-dimensional patterns (as the one in Figure 3) visualization is not of much help; (2) We want to extract the topology of thousands of patterns, and so we need to be able to do this in an automated and efficient way. We therefore want to exploit the fact that there are efficient algorithms to compute homology, which are capable of handling large amounts of data; (3) While it is possible to use some computational tricks to do these computations in dimensions up to three, we want to benefit from the fact that the available homology algorithms are dimension independent, which allow us to add time as an extra dimension (as will be discussed latter) and possibly do computations in dimensions four or higher.

Before we go into the specifics of what homology is and how to compute it, let us look with a little more detail what kind of patterns we want to compute the homology of and why we care about them. While we are going to present next just a few examples, it is important to stress that the techniques presented in this thesis can, in principle, be applied to virtually any system that generates complicated time-dependent patterns. We will next present three examples. In the first one (spiral defect chaos) the patterns are generated experimentally. In the other two the patterns are produced by simulations (numerical solutions of differential equations). The difference between them is that in the second example (Cahn-Hilliard theory of phase separation) we consider patterns on the spatial domain only, while in the last example (spiral wave patterns) we need to combine space and time to produce patterns in the space-time domain.

1.1 Spiral Defect Chaos in Rayleigh-Bénard Convection

Rayleigh-Bénard convection refers to the following phenomenon of fluid convection: A thin layer of fluid is confined between two plates (the bottom plate and the top plate). The bottom plate is heated while the top plate is kept at a constant (colder) temperature. When the temperature difference, ΔT, between the two plates exceeds a critical threshold, ΔT_c, the onset of fluid motion occurs. The flow organizes into a pattern of convective rolls where hot regions of the fluid move upward and cold regions flow downward. For ΔT close to the critical value ΔT_c the rolls essentially form parallel strips (Figure 4). When ΔT is sufficiently large, the system enters on a weakly turbulent state known as *Spiral Defect Chaos* (SDC). In this state the convection rolls become spatially disordered and exhibit complex time dependence (Figure 4).

Having the experimental data, a natural question to ask is: What kind of information can we extract from the data? For example, can we decide if two data sets were obtained at different parameter values? The system control parameter used in our experiments is the *reduced Rayleigh number* $\epsilon = (\Delta T - \Delta T_c)/\Delta T_c$. As we can see from Figure 6 this may not be immediately clear by simple visual inspection.

Figure 4: Images of convective flow in Rayleigh-Bénard convection at ϵ close to the onset of convection (left image) and at larger values of ϵ (two right images) at which SDC can be observed. The dark regions correspond to hot upflow, and the bright regions to cold downflow.

The equations governing the fluid flow in an ideal Rayleigh-Bénard convection are the well known *Navier-Stokes* equations [16]. Due to the difficulty of numerically solving the Navier-Stokes

equations, a simpler model, known as the *Boussinesq approximation*, is often used. In the Boussinesq approximation all the properties of the fluid, with the exception of the density in the driving buoyancy term, are considered independent of the temperature. The equations describing Rayleigh-Bénard convection in the Boussinesq approximation are

$$\begin{aligned} \frac{1}{P}\left[\frac{\partial \boldsymbol{u}}{\partial t} + (\boldsymbol{u}\cdot\nabla)\boldsymbol{u}\right] &= -\nabla p + T\hat{\boldsymbol{y}} + \nabla^2 \boldsymbol{u} \\ \frac{\partial T}{\partial t} + \boldsymbol{u}\cdot\nabla T &= Rw + \nabla^2 T \\ \nabla\cdot\boldsymbol{u} &= 0 \end{aligned} \tag{1}$$

where $\boldsymbol{u} = (u, v, w)$ is the velocity, and T denotes the departure from a linear temperature profile. The dimensionless numbers R and P are, respectively, the Rayleigh and the Prandtl numbers [25].

Equations (1) can be used to numerically simulate SDC patterns. One then might ask whether we can compare the experimental data with numerically simulated data and decide if there are any fundamental differences. Patterns simulated by (1) are visually very similar to the experimental ones (compare Figure 5 with Figure 6 (c)). In Chapter 3 we use computational homology as a possible way to try to address these and other questions.

Figure 5: Pattern in SDC obtained by numerical simulation of (1). Image from Mark Paul's web page [58]. The image is produced by numerically solving (1) and thresholding the temperature.

Let us now discuss what are the exact regions we want to compute homology of, and what is the output of the homology computations. The first step is to convert the intensity images to binary images by thresholding the images at some appropriate value. The resulting binary images (Figure 6), are used as input to the computation of homology. In what follows, $X(n, \epsilon)$ represents the n^{th} binary image in a time series at the reduced Rayleigh number ϵ. Moreover, $X^{hot}(n, \epsilon)$ and

$X^{cold}(n, \epsilon)$ denote the hot flow and cold flow regions, respectively, of $X(n, \epsilon)$.

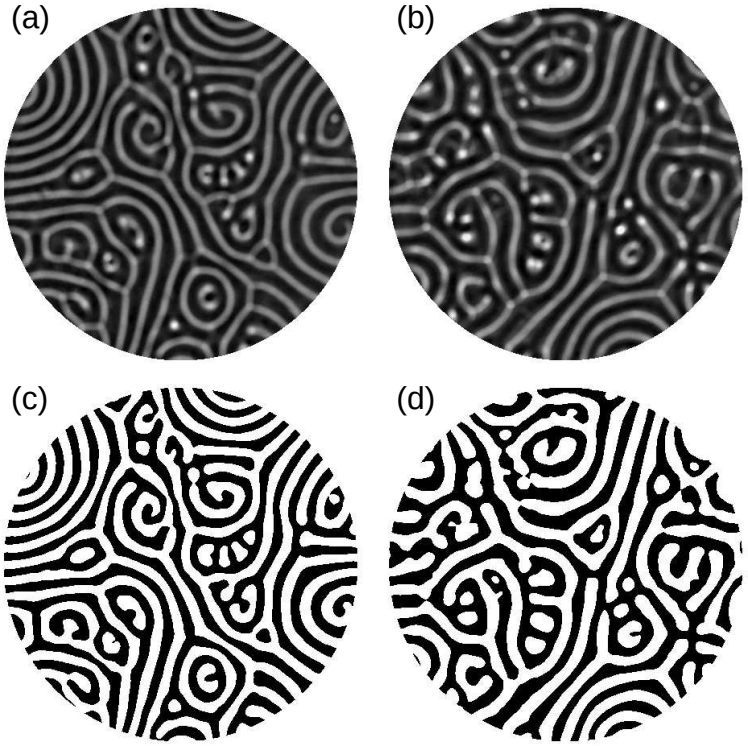

Figure 6: Images of spiral defect chaos convection patterns at reduced Rayleigh numbers $\epsilon \approx 1.0$ (a) and $\epsilon \approx 2.0$ (b) are converted to binary valued images [(c) and (d), respectively] by thresholding the data at the median value of intensity.

Homology theory will be discussed in Chapter 2. For now let us just say that the homology of a structure X in two dimensions (e.g., $X^{hot}(n, \epsilon)$ or $X^{cold}(n, \epsilon)$) is characterized by two nonnegative integers β_i, $i = 0, 1$ called *Betti numbers*, where β_0 counts the number of connected components (pieces) of X, and β_1 is equal to the number of holes (loops) in X. A concrete illustration of this classification applied to convection patterns is given in Figure 7. We compute homology of a time series of images, and get time series of Betti numbers. We then do statistic analysis on these time series of Betti numbers to extract dynamic information about the system. This approach applied to SDC will be discussed in Chapter 3, where we will see that it seems to be very useful to extract dynamic information from the patterns.

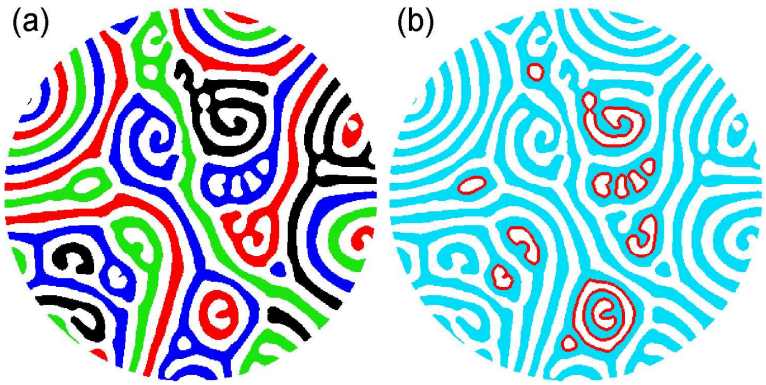

Figure 7: Betti numbers for the X^{hot} region shown in Figure 6 (c). Image (a) shows the $\beta_0^{hot} = 34$ distinct components, with neighboring components distinguished by different colors. Image (b) indicates the boundaries of the $\beta_1^{hot} = 13$ holes.

1.2 Cahn-Hilliard Theory of Phase Separation

The kinetics of phase separation in alloys has drawn considerable interest in recent years. Most alloys of commercial interest owe their properties to specific microstructures which are generated through special processing techniques, such as phase separation mechanisms. In quenched binary alloys, for example, one typically observes phase separation due to a nucleation and growth process, or alternatively, due to spinodal decomposition [7, 10, 11]. While the former process involves a thermally activated nucleation step, spinodal decomposition can be observed if the alloy is quenched into the unstable region of the phase diagram. The resulting inherent instability leads to composition fluctuations, and thus to instantaneous phase separation. Common to both mechanisms is the fact that the generated microstructures usually are thermodynamically unstable and will change in the course of time — thereby affecting the material properties. In order to describe these and other processes, one generally relies on models given by nonlinear evolution equations. Many of these models are phenomenological in nature, and it is therefore of fundamental interest to study how well the equations agree with experimental observations.

The first model for spinodal decomposition in binary alloys is due to Cahn and Hilliard [7, 10]. Their mean field approach leads to a nonlinear evolution equation for the relative concentration difference $u = \rho_A - \rho_B$, where ρ_A and ρ_B denote the relative concentrations of the two components,

i.e., $\rho_A + \rho_B = 1$. The Ginzburg-Landau free energy is given by

$$E_\gamma(u) = \int_\Omega \left(\Psi(u) + \frac{\gamma}{2} |\nabla u|^2 \right) dx, \tag{2}$$

where Ω is a bounded domain, and the positive parameter γ is related to the root mean square effective interaction distance. The bulk free energy, Ψ, is a double well potential, typically

$$\Psi(u) = \frac{1}{4} \left(u^2 - 1 \right)^2. \tag{3}$$

Taking the variational derivative $\delta E_\gamma / \delta u$ of the Ginzburg-Landau free energy (2) with respect to the concentration variable u, we obtain the chemical potential

$$\mu = -\gamma \Delta u + \frac{\partial \Psi}{\partial u}(u),$$

and thus the Cahn-Hilliard equation $\partial u / \partial t = \Delta \mu$, i.e.,

$$\frac{\partial u}{\partial t} = -\Delta \left(\gamma \Delta u - \frac{\partial \Psi}{\partial u}(u) \right), \tag{4}$$

subject to no-flux boundary conditions for both μ and u. Due to these boundary conditions, any mass flux through the boundary is prohibited, and therefore the mass m is conserved.

One drawback of the deterministic partial differential equation (4) is that it completely ignores thermal fluctuations. To remedy this, Cook [14] extended the model by adding a random fluctuation term ξ, i.e., he considered the stochastic Cahn-Hilliard-Cook model

$$\frac{\partial u}{\partial t} = -\Delta \left(\gamma \Delta u - \frac{\partial \Psi}{\partial u}(u) \right) + \sigma \cdot \xi, \tag{5}$$

where

$$\langle \xi(t, x) \rangle = 0, \qquad \langle \xi(t_1, x_1) \xi(t_2, x_2) \rangle = \delta(t_1 - t_2) \delta(x_1 - x_2).$$

Here $\sigma > 0$ is a measure for the intensity of the fluctuation. Both the deterministic and the stochastic model produce patterns which are qualitatively similar to the microstructures observed during spinodal decomposition [8].

Even though both models are based on deep physical insight, they are phenomenological models. Many researchers have therefore studied how well the models agree with experimental observations. See for example [4, 24, 30, 49], as well as the references therein.

We solve (5) numerically and, once again, threshold the data to generate patterns. Since $u(x,t)$ represents the relative concentration difference between the two materials, a natural way to threshold the data is by constructing the sets

$$X^+(t) := \{x \in \Omega \mid u(t,x) > 0\} \quad \text{and} \quad X^-(t) := \{x \in \Omega \mid u(t,x) < 0\},$$

which represent the regions in the alloy where one or the other material dominates. Figure 8 shows a plot of these regions, obtained by numerically solving (5) with a random initial condition.

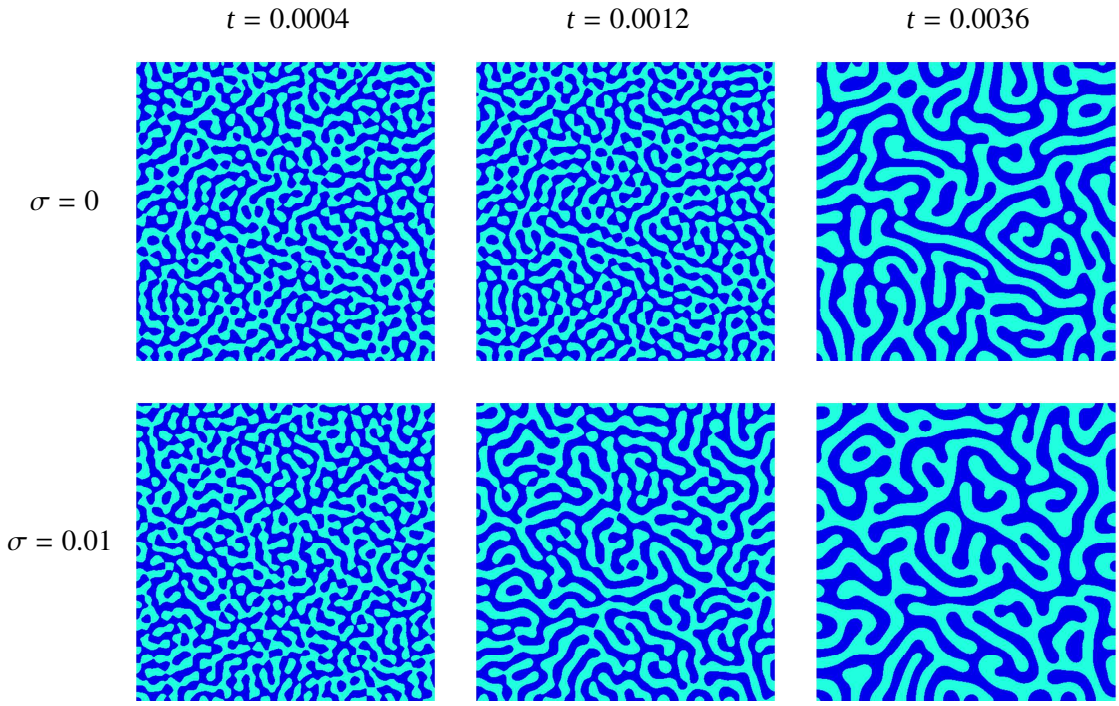

Figure 8: Microstructures obtained from the Cahn-Hilliard-Cook model (5). The top row shows solution snapshots for the deterministic case $\sigma = 0$, the bottom row is for noise intensity $\sigma = 0.01$. In both cases we used $\gamma^{1/2} = 0.005$ and $m = 0$. The set $X^+(t)$ is shown in dark blue and $X^-(t)$ in light blue.

Visual inspection reveals that the patterns are very similar at $t = 0.0004$, and $t = 0.0036$. At $t = 0.0012$ we can observe that the pattern for the stochastic case ($\sigma > 0$) is coarser grained than the one for the deterministic case ($\sigma = 0$). But do these patterns represent the characteristic behavior of (5)? Or are these differences just artifacts from the fact that we are looking at just one solution of a (gradient) stochastic partial differential equation with random initial condition? If there are any fundamental differences between the deterministic and the stochastic cases, can we quantify them?

Can we determine the parameters at which a given sequence of patterns were generated? Can we determine how realistically the simulated data compares to experimental data? Which system, the stochastic or the deterministic, is a better model for experimental data? Can we characterize the morphology changes due to other parameters (such as mass for example) variation? Once again homology seems to be very useful in answering some of these questions as it will be discussed in Chapter 4.

Real materials are 3-dimensional objects. So if we want to study realistic models or experimental data we need to consider 3-dimensional patterns. Let us close this section with some examples of 3-dimensional patterns generated from (5) on a 3-dimensional domain. Since now the patterns are 3-dimensional, extracting information by direct visualization is even harder. Figure 9 shows the set $X^+(t)$ and Figure 10 shows the isosurface

$$X^0(t) := \{x \in \Omega \mid u(t,x) = 0\}.$$

The homology of a 3-dimensional structure, such as $X^0(t)$, is characterized by three integers: β_0 which still counts the number of components, β_1 which now counts the number of tunnels through the structure, and β_2 which counts the number of voids (cavities) in the structure. The homology of Figure 10 tells us that the entire structure is formed by one single component ($\beta_0 = 1$), there are 1701 tunnels through the structure ($\beta_1 = 1701$), and there are no voids ($\beta_2 = 0$).

1.3 Excitable Media and Spiral Waves

As mentioned in the beginning of this chapter, to analyze spiral wave patterns, we will "look" at them in the space-time domain, rather than in the space domain only, as it was done in the previous examples. We are interested in analyzing 2-dimensional wave patterns, but to develop our intuition as to why we need to include time we will first consider the 1-dimensional Gray-Scott model, and then we will consider the 2-dimensional FitzHugh-Nagumo system.

1.3.1 The Gray-Scott Model

The Gray-Scott system models the chemical reactions $U + 2V \to 3V$ and $V \to P$ in a gel reactor, where U and V are two chemical species, V catalyzes its own reaction with U, and P is an inert product. Letting u and v denote the concentrations of U and V, respectively, the Gray-Scott model

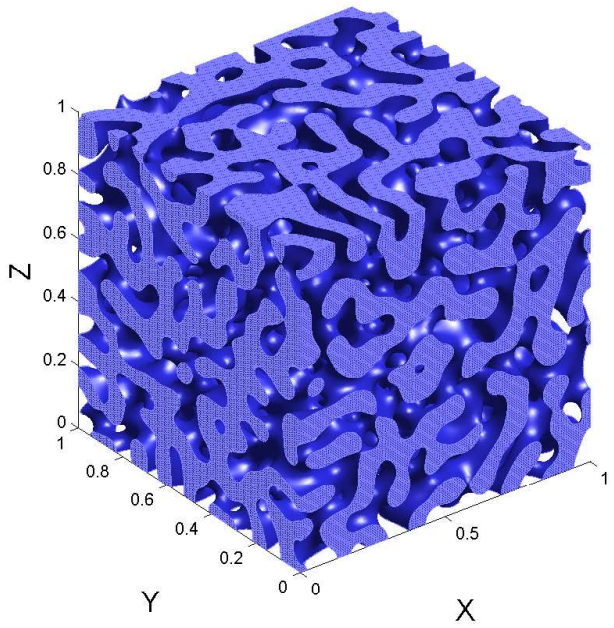

Figure 9: Patterns showing the set $X^+(t) = \{x \in \Omega \mid u(t,x) > 0\}$ obtained by numerically solving (5) on a 3-dimensional domain with a random initial condition.

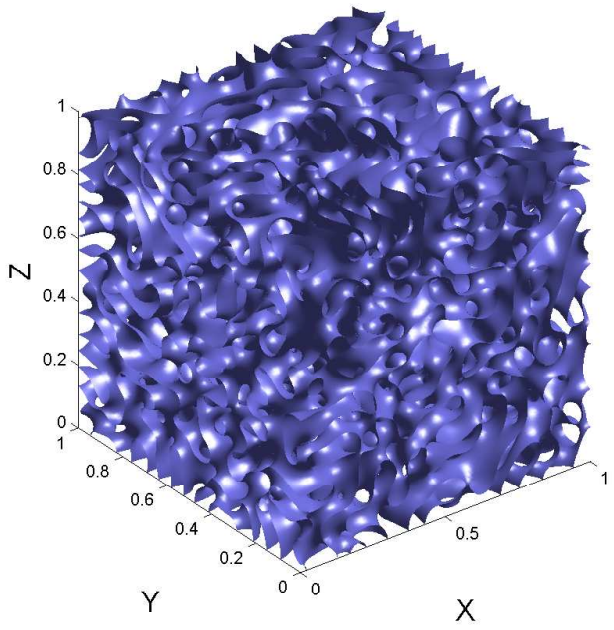

Figure 10: Plot of isosurface $X^0(t) := \{x \in \Omega \mid u(t,x) = 0\}$ corresponding to the solution used in Figure 9.

is given by

$$\begin{aligned} u_t &= d_1 u_{xx} - uv^2 + F(1-u) \\ v_t &= d_2 v_{xx} + uv^2 - (F+k)v \end{aligned} \tag{6}$$

where d_1 and d_2 are the diffusion coefficients, F is the in-flow rate of U from outside, and $F + k$ the removal rate of V from the reaction field (see [56, 73]). We consider (6) on the 1-dimensional domain $\Omega = [0, 1.6]$ with Neumann boundary condition and with $d_1 = 2 \times 10^{-5}$, $d_2 = 10^{-5}$, $F = 0.035$, and $k = 0.05632$ at which complicated spatio-temporal dynamics has been reported [56, 55]. This system will be studied in Chapter 5. Numerical solutions of (6) are shown in Figure 11.

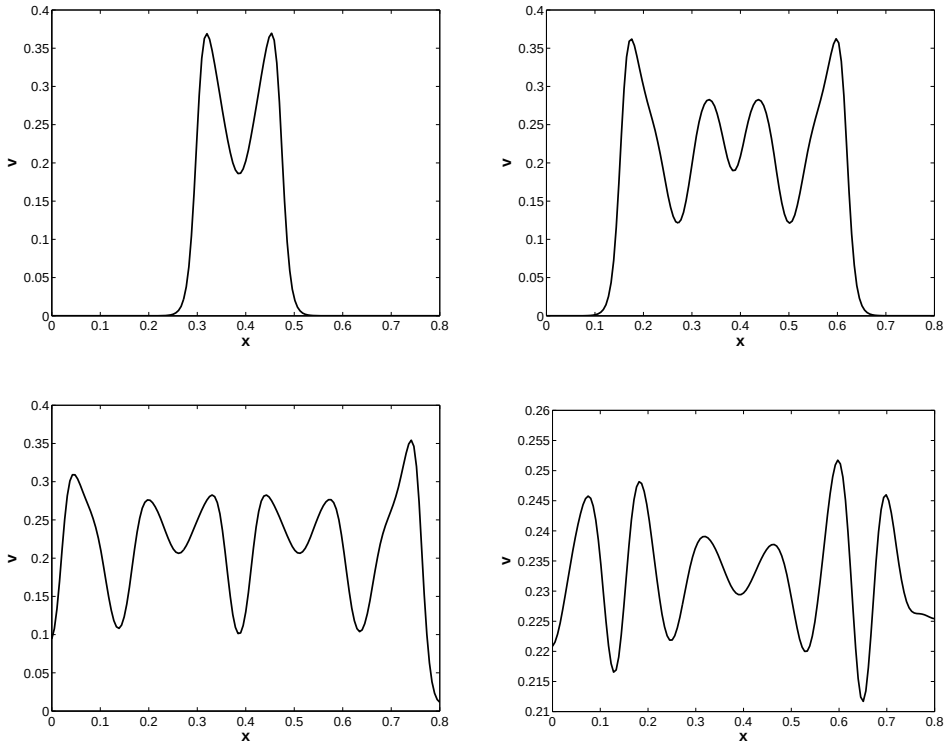

Figure 11: Several snapshots of a numerical solution $v(x, t)$ of (6).

Our aim is to understand the time evolution of the solutions of (6). If we just threshold the solution plotted in Figure 11 for each time step, we get 1-dimensional patterns with just a few number of components. In other words, the topology of the 1-dimensional thresholded regions would be very simple. What makes (6) interesting is the interaction between the pulses (humps) shown in Figure 11 (see [56, 55]). To try to capture these interactions we need to look at the solutions in space-time, instead of just looking at snapshots of the solution. So we visualize the

solutions by plotting $v(x,t)$ as a 2-dimensional surface as is done on the left diagram of Figure 12. If we now threshold the the data, and consider the set

$$E(t) = \{x \in \Omega \mid v(x,t) \geq 0.23\},$$

we generate patterns (Figure 12 right) that capture the spatial-temporal evolution of the system. These are the patterns we want to compute the homology of.

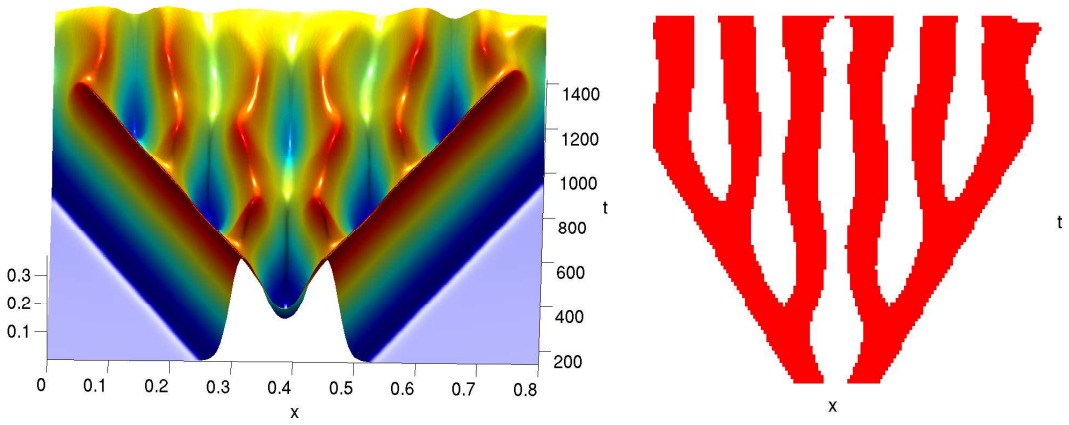

Figure 12: Time evolution (left) and corresponding 2-dimensional pattern (right) of a numerical solution $v(x,t)$ of (6). On the right diagram the colored region correspond to the excited media defined by $v \geq 0.23$.

To understand how such patterns capture the hump interactions, let us consider the pattern in Figure 13. This pattern was generated in the same way as the one in Figure 12, only for a longer time interval and with a different initial condition. In this pattern we highlight the holes in black, and plot the different components in different colors. A geometrical interpretation for this pattern is as follows: The colored regions correspond to humps in the solutions, and different components correspond to humps that never collide. As for the holes, consider the leftmost hole in Figure 13 for example; it arises from the division of one hump into two humps which separate for some amount of time and then coalesce together at a later point in time.

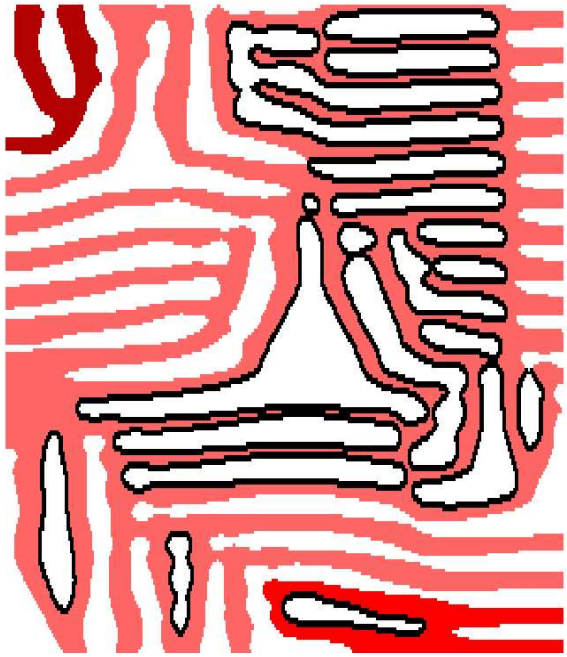

Figure 13: The black and gray (black and red) region indicates the evolution of the pattern of the excited media defined by $v \geq 0.23$.

1.3.2 The FitzHugh-Nagumo System

Consider the FitzHugh-Nagumo system

$$\begin{aligned} u_t &= \Delta u + \epsilon^{-1} u(1-u)(u - \tfrac{v+\gamma}{\alpha}) \\ v_t &= u^3 - v, \end{aligned} \tag{7}$$

which is a model for excitable media (see [2]) and will be considered in Chapter 5. Let us fix $\alpha = 0.75$, $\gamma = 0.06$, and use Neumann boundary conditions. Initially let us take the rectangular domain $\Omega = [0, 80] \times [0, 80]$. Once again, we solve (7) numerically, threshold the data, and define the excited media at time t as the set of points

$$E(t) = \{x \in \Omega \mid u(x, t) \geq 0.9\}.$$

Several plots of the thresholded data are shown on Figure 14, where the excited media is presented in red.

As we can see from Figure 14 the patterns generated by (7) vary greatly as we change the parameter ϵ. Just by visualization it may be hard to decide, for example, if the patterns in the two

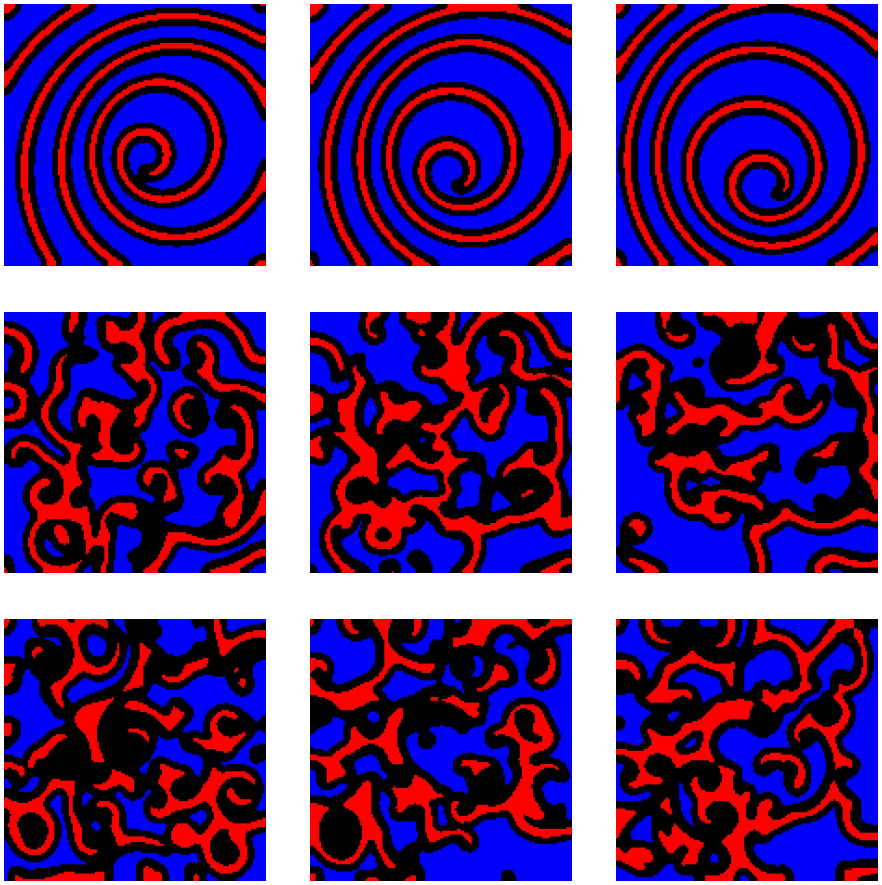

Figure 14: Wave patterns generated by (7). The light gray (red) region corresponds to excited points ($u \geq 0.9$), dark gray (blue) to the quiescent region ($u \leq 0.1$), and black to the reaction zone ($0.1 < u < 0.9$).

bottom rows correspond to different parameters or to the same parameter at different times. The homology of each one of the patterns in Figure 14 is very simple: just a few components and holes. So to be able to extract useful information we need analyze how things change in the space-time domain. As for the Gray-Scott model we compute homology of the excited regions, only that now each frame of the movie is 2-dimensional so when we add time as an extra dimension we get a 3-dimensional object, as it is shown in Figure 15.

In Chapter 5 we will compute homology of such patterns and extract time series of Betti numbers. These time series will allow us to compute Lyapunov exponents and an entropy. We will also use these time series to characterize the patterns at different parameter values.

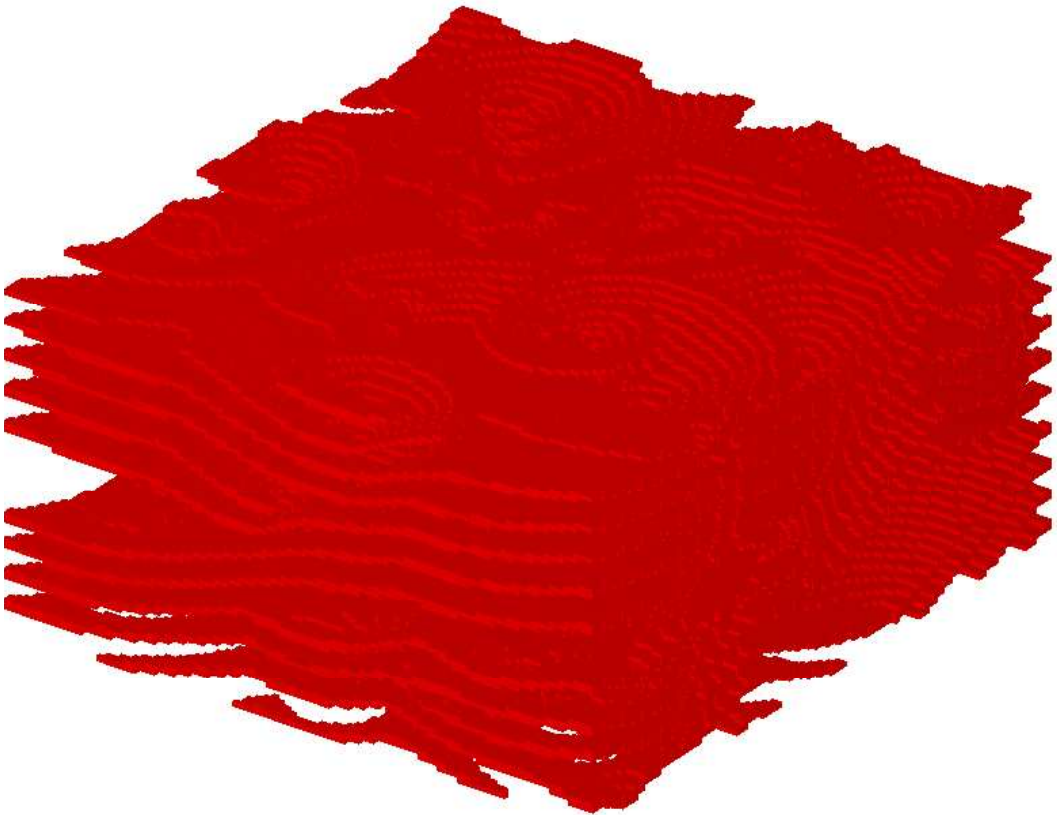

Figure 15: 3-dimensional representation of the excited regions generated by (7).

1.4 Thesis Outline

This thesis is organized as follows: In Chapter 2 we give a brief overview of homology theory and discuss algorithms for the computation of homology. In this chapter we also have a brief discussion about how the errors in the numerical approximations of the partial differential equations or the noise in the experiments affect the outcome of the homology computation. In Chapter 3 we discuss spiral defect chaos and the topological results obtained for this system. The experiments on SDC were performed by Kapilanjan Krishan and Michael Schatz in Michael Schatz's laboratory at Georgia Tech. In Chapter 4 we briefly describe the Cahn-Hilliard theory of phase separation and discuss how homology can be used to analyze this system. The material of this chapter is joint work with

Konstantin Mischaikow and Thomas Wanner and has been published in [23]. Finally in Chapter 5 we describe the use of homology to analyze patterns arising in excitable media. The material of this chapter is joint work with Konstantin Mischaikow and William Kalies and has been published in [22].

CHAPTER II

COMPUTATIONAL HOMOLOGY

In this chapter we present a brief description of *homology theory*. Homology is part of a branch of mathematics called *algebraic topology*. The main theme in algebraic topology is to assign algebraic objects to a given topological space, and then use these algebraic objects to draw conclusions about the given topological space. In particular homology theory assigns to a topological space X a sequence of abelian groups $H_i(X)$, $i = 0, 1, 2, \ldots$, called the *homology groups* of X. The precise way in which this is done depends essentially on which class of topological spaces one wants to define homology of and how these spaces are represented. For a discussion of several homology theories see [66, 54, 47, 33]. In this thesis we will discuss *Cubical Homology*. In this theory the topological spaces are represented as a collection of cubes, which is the natural setting for the kinds of spaces we consider. In Section 2.1 we will present the basic definition of cubical homology theory, in Section 2.2 we will present the algorithms used to compute homology, in Section 2.3 we will discuss a possible approach to handle the errors introduced by the cubical approximation, and finally in Section 2.4 we will discuss the advantages (and disadvantages) of using homology to analyze patterns.

2.1 Cubical Homology

In this section we present a brief description of cubical homology. For more details see [33]. As mentioned above the spaces we will consider consist of a collection of cubes. So let us start by precisely defining what kind of cubes we consider.

Definition 2.1.1. *An* elementary interval *is an interval $I \subset \mathbb{R}$ of the form*

$$I = [l, l + 1] \quad or \quad I = [l, l]$$

for some $l \in \mathbb{Z}$. We write

$$[l] = [l, l]$$

for intervals containing a single point, and call these intervals degenerate. *Intervals of the form* $[l, l+1]$ *are called* nondegenerate.

Definition 2.1.2. *An* elementary cube *Q is a finite product of elementary intervals, that is,*

$$Q = I_1 \times I_2 \times \cdots \times I_d \subset \mathbb{R}^d,$$

where each I_i is an elementary interval. The set of all elementary cubes in $\mathbb{R}^d$ is denoted by $\mathcal{K}^d$. The set of all elementary cubes is denoted by $\mathcal{K}$, that is,

$$\mathcal{K} := \bigcup_{d=1}^{\infty} \mathcal{K}^d.$$

Definition 2.1.3. *Let $Q = I_1 \times I_2 \times \cdots \times I_d \subset \mathbb{R}^d$ be an elementary cube. The* embedding number *of Q is defined to be d and is denoted by $emb(Q)$. The interval I_i is referred to as the ith* component *of Q and is written as $I_i(Q)$. The* dimension *of Q is defined to be the number of nondegenerate components in Q and is denoted $dim(Q)$. We refer to an elementary cube Q with $dim(Q) = k$ as a k-cube and denote*

$$\mathcal{K}_k := \{Q \in \mathcal{K} \mid dim(Q) = k\},$$

and

$$\mathcal{K}_k^d := \mathcal{K}_k \cap \mathcal{K}^d.$$

Some examples of elementary cubes in $\mathbb{R}$ and $\mathbb{R}^2$ are shown in Figure 16.

We can now define the class of topological spaces for which we will define homology.

Definition 2.1.4. *A set $X \subset \mathbb{R}^d$ is called a* cubical complex *if X can be written as a finite union of elementary cubes.*

Given a cubical complex $X \subset \mathbb{R}^d$, we define

$$\mathcal{K}(X) := \{Q \in \mathcal{K} \mid Q \subset X\}$$

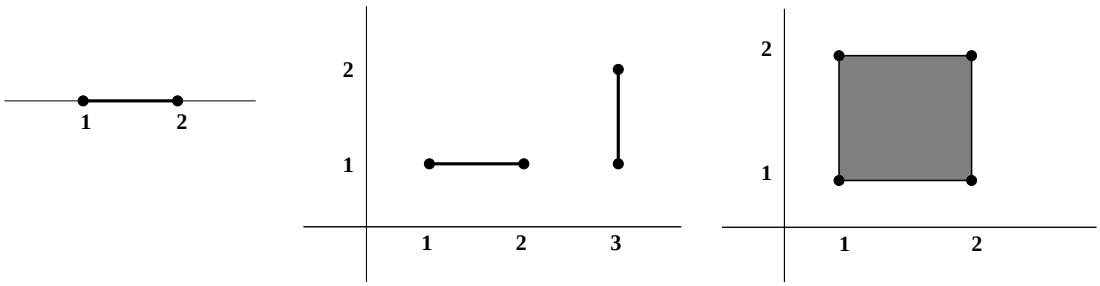

Figure 16: The elementary 1-cube $[1,2] \subset \mathbb{R}$ (left), the elementary 1-cubes $[1,2] \times [1] \subset \mathbb{R}^2$ and $[3] \times [1,2] \subset \mathbb{R}^2$ (middle), and the elementary 2-cube $[1,2] \times [1,2] \subset \mathbb{R}^2$ (right).

and

$$\mathcal{K}_k(X) := \{Q \in \mathcal{K}(X) \mid \dim(Q) = k\}.$$

Sometimes we use the notation $\mathcal{K}^d(X)$ for $\mathcal{K}(X)$ as a reminder that $X \subset \mathbb{R}^d$. We also denote $\mathcal{K}_k^d(X) := \mathcal{K}^d(X) \cap \mathcal{K}_k(X)$. The elements of $\mathcal{K}_0(X)$ are called the *vertices* of X and the elements of $\mathcal{K}_1(X)$ the *edges* of X. More generally, the elements of $\mathcal{K}_k(X)$ are the *k-cubes* of X.

As we mentioned in the beginning of this chapter, we want to assign algebraic objects (abelian groups) to topological spaces. The first step is to assign algebraic objects to the elementary cubes. This is done as follows.

Definition 2.1.5. *With each elementary k-cube $Q \in \mathcal{K}_k^d$ we associate an algebraic object $\widehat{Q}$ called an* elementary k-chain *of $\mathbb{R}^d$, where $\widehat{Q} : \mathcal{K}_k^d \to \mathbb{Z}$ is the function defined by*

$$\widehat{Q}(P) = \begin{cases} 1 & \text{if} \quad P = Q \\ 0 & \text{otherwise.} \end{cases}$$

We also define $\widehat{0} : \mathcal{K}_k^d \to \mathbb{Z}$ as the zero function, that is, $\widehat{0}(Q) = 0$ for all $Q \in \mathcal{K}_k^d$.

The set of all elementary k-chains of $\mathbb{R}^d$ is denoted by

$$\widehat{\mathcal{K}}_k^d := \left\{\widehat{Q} \mid Q \in \mathcal{K}_k^d\right\},$$

and the set of all *elementary chains* of $\mathbb{R}^d$ is defined by

$$\widehat{\mathcal{K}}^d := \bigcup_{k=0}^{\infty} \widehat{\mathcal{K}}_k^d.$$

Given an elementary cube Q, we refer to $\widehat{Q}$ as its *dual elementary chain*. Similarly, given an elementary chain $\widehat{Q}$, we refer to Q as its *dual elementary cube*. This is justified by the following proposition.

Proposition 2.1.6. *The map $\phi : \mathcal{K}_k^d \to \widehat{\mathcal{K}}_k^d$ given by $\phi(Q) = \widehat{Q}$ is a bijection.*

Proof. See [33]. □

The previous proposition tells us that there is a one to one correspondence between the elementary k-cubes (the topological objects) and the elementary k-chains (the algebraic objects). This means that we may be able to transfer conclusions about the algebraic objects to the topological ones through this correspondence. This is one of the fundamental ideas in homology theory. The next step is to put some algebraic structure on the algebraic objects (the elementary k-chains). This is done in the following definition.

Definition 2.1.7. *The group C_k^d of* k-dimensional chains *of $\mathbb{R}^d$ (k-chains for short) is the free abelian group generated by the elementary chains of $\mathcal{K}_k^d$. Thus the elements of C_k^d are function $c : \mathcal{K}_k^d \to \mathbb{Z}$ such that $c(Q) = 0$ for all but a finite number of $Q \in \mathcal{K}_k^d$.*

As it was mentioned in Chapter 1, the homology of a 2-dimensional region is meant to simply count the number of connected components (pieces) and the number of holes (loops). To start to understand how this is done let us look at the spaces in Figure 17 that are composed of elementary 0-cubes and 1-cubes. The picture on the left does not form a loop while the one on the right does. This is characterized essentially by the fact that the figure on the left has a boundary, in the topological (geometrical) sense, given by $\{A\} \cup \{B\}$. The picture on the right, on the other hand, does not have a boundary.

But we do not want to use topology to extract other topological information (like above, where the topological boundary gives us information about the existence of loops). We want to use algebra to extract such information. The first step in this direction is to precisely define what is meant by the algebraic boundary of a k-chain. The following definitions and notations are used to define the boundary operator.

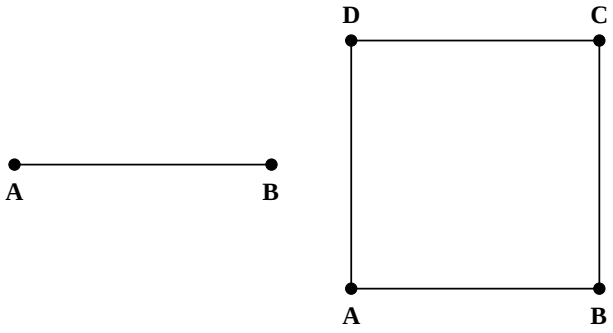

Figure 17: The picture on the left has a boundary, given by $\{A\} \cup \{B\}$, and so it does not form a loop. The picture on the right does not have a boundary, and so it forms a loop.

Definition 2.1.8. *Consider* $c_1,\ c_2 \in C_k^d$, *where* $c_1 = \sum_{i=1}^m \alpha_i \widehat{Q_i}$ *and* $c_2 = \sum_{i=1}^m \beta_i \widehat{Q_i}$. *The* scalar product *of the chains* c_1 *and* c_2 *is defined as*

$$\langle c_1, c_2 \rangle := \sum_{i=1}^{m} \alpha_i \beta_i.$$

Definition 2.1.9. *Given two elementary cubes* $P \in \mathcal{K}_{k_1}^{d_1}$ *and* $Q \in \mathcal{K}_{k_2}^{d_2}$, *set*

$$\widehat{P} \diamond \widehat{Q} := \widehat{P \times Q}.$$

This definition extends to arbitrary chains $c_1 \in C_{k_1}^{d_1}$ *and* $c_2 \in C_{k_2}^{d_2}$ *by*

$$c_1 \diamond c_2 := \sum_{P \in \mathcal{K}_{k_1},\ Q \in \mathcal{K}_{k_2}} \langle c_1, \widehat{P} \rangle \langle c_2, \widehat{Q} \rangle \widehat{P \times Q}.$$

The chain $c_1 \diamond c_2 \in C_{k_1+k_2}^{d_1+d_2}$ *is called the* cubical product *of* c_1 *and* c_2.

Proposition 2.1.10. *Let* $\widehat{Q}$ *be an elementary cubical chain of* $\mathbb{R}^d$ *with* $d > 1$. *Then there exist unique elementary cubical chains* $\widehat{I}$ *and* $\widehat{P}$ *with* $emb(I) = 1$ *and* $emb(P) = d - 1$ *such that*

$$\widehat{Q} = \widehat{I} \diamond \widehat{P}.$$

Proof. See [33]. □

Definition 2.1.11. *Given* $k \in \mathbb{Z}$, *the* cubical boundary operator *or* cubical boundary map

$$\partial_k : C_k^d \to C_{k-1}^d$$

is a homomorphism of free abelian groups, which is defined for an elementary chain $\widehat{Q} \in \widehat{\mathcal{K}}_k^d$ *by induction on the embedding number* d *as follows. Consider first the case* $d = 1$*. Then* Q *is an elementary interval and hence* $Q = [l] \in \mathcal{K}_0^1$ *or* $Q = [l, l+1] \in \mathcal{K}_1^1$ *for some* $l \in \mathbb{Z}$*. Define*

$$\partial_k \widehat{Q} := \begin{cases} 0 & \text{if } Q = [l], \\ \widehat{[l+1]} - \widehat{[l]} & \text{if } Q = [l, l+1]. \end{cases}$$

Now assume that $d > 1$*. Let* $I = I_1(Q)$ *and* $P = I_2(Q) \times \cdots \times I_d(Q)$*. Then by Proposition 2.1.10,*

$$\widehat{Q} = \widehat{I} \diamond \widehat{P}.$$

Define

$$\partial_k \widehat{Q} := \partial_{k_1} \widehat{I} \diamond \widehat{P} + (-1)^{k_1} \widehat{I} \diamond \partial_{k_2} \widehat{P},$$

where $k_1 = dim(I)$ *and* $k_2 = dim(P)$*. Finally, we extend the definition to all chains by linearity; that is, if* $c = \alpha_1 \widehat{Q}_1 + \alpha_2 \widehat{Q}_2 + \cdots + \alpha_m \widehat{Q}_m$*, then*

$$\partial_k c := \alpha_1 \partial_k \widehat{Q}_1 + \alpha_2 \partial_k \widehat{Q}_2 + \cdots + \alpha_m \partial_k \widehat{Q}_m.$$

In what follows we will simplify the notation ∂_k to ∂. Geometrically the boundary of a k-chain is just the alternating sum of its $(k-1)$-dimensional faces. Figure 18 illustrates this fact.

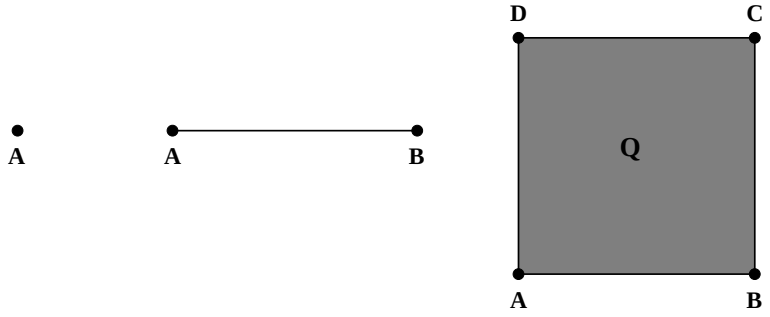

Figure 18: The boundary of the 0-chain $\widehat{A}$ (left) is $\partial(\widehat{A}) = \widehat{0}$, the boundary of the 1-chain $\widehat{[A, B]}$ (middle) is given by $\partial(\widehat{[A, B]}) = \widehat{B} - \widehat{A}$, and the boundary of the 2-chain $\widehat{Q}$ (right) is given by $\partial(\widehat{Q}) = \widehat{[A, B]} + \widehat{[B, C]} - \widehat{[D, C]} - \widehat{[A, D]}$.

Now we have the notion of the (algebraic) boundary of a k-chain, and that loops have no boundary (have boundary equal to zero). But having boundary equal to zero is not enough to characterize a loop, as we can see from Figure 19. The chain $\widehat{[A, B]} + \widehat{[B, C]} - \widehat{[D, C]} - \widehat{[A, D]}$ (the contour of the cube) has zero boundary in both pictures of Figure 19, but the one on the left characterizes a

loop (hole), while the one on the right does not. The reason $[\widehat{A,B}] + [\widehat{B,C}] - [\widehat{D,C}] - [\widehat{A,D}]$ on the picture on the right does not characterize a hole is because the hole is "filled in" by the 2-chain Q. Algebraically this is characterized by the fact that $\partial(\widehat{Q}) = [\widehat{A,B}] + [\widehat{B,C}] - [\widehat{D,C}] - [\widehat{A,D}]$.

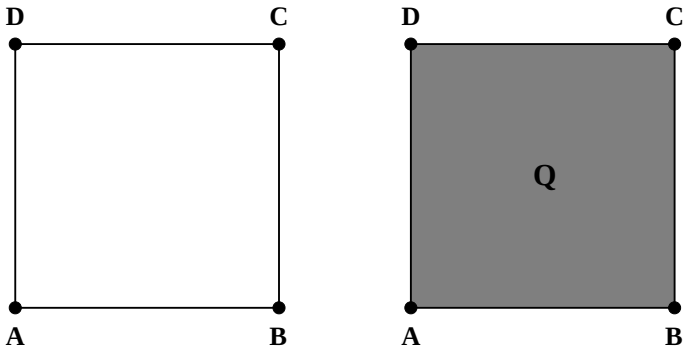

Figure 19: The chain $[\widehat{A,B}] + [\widehat{B,C}] - [\widehat{D,C}] - [\widehat{A,D}]$ have zero boundary in both pictures, but the one on the left characterizes a loop (hole), while the one on the right does not.

Therefore holes are characterized by chains that have boundary equal to zero, but are not themselves boundary of other chains. We therefore want to "count" the chains which have zero boundary, but are not boundaries. Let us first introduce some more notations.

Definition 2.1.12. *Let $X \subset \mathbb{R}^d$ be a cubical complex. Let $\widehat{\mathcal{K}_k}(X) := \{\widehat{Q} \mid Q \in \mathcal{K}_k(X)\}$. We define the set of k-*chains *of X as the subgroup $C_k(X)$ of C_k^d generated by the elements of $\widehat{\mathcal{K}_k}(X)$.*

Before we define homology we need the following proposition.

Proposition 2.1.13. *Let $X \subset \mathbb{R}^d$ be a cubical complex. Then*

$$\partial_k(C_k(X)) \subset C_{k-1}(X).$$

Proof. See [33]. □

As a consequence of this proposition we can give the following definition.

Definition 2.1.14. *The boundary operator of the cubical complex X is defined to be*

$$\partial_k^X : C_k(X) \to C_{k-1}(X)$$

obtained by restricting $\partial_k : C_k^d \to C_{k-1}^d$ to $C_k(X)$.

Let $X \subset \mathbb{R}^d$ be a cubical set. A k-chain $z \in C_k(X)$ is called a *k-cycle* in X if $\partial z = 0$. Thus the set of all k-cycles of X is the kernel of ∂_k^X, and so it is a subgroup of $C_k(X)$. We denote the set of all k-cycles by $Z_k(X)$.

A k-chain $z \in C_k(X)$ is called a *boundary* in X if there exists $c \in C_{k+1}(X)$ such that $\partial c = z$. Thus the set of all boundary elements in $C_k(X)$ is the image of ∂_{k+1}^X, and so it is also a subgroup of $C_k(X)$. We denote the set of all boundary elements in $C_k(X)$ by $B_k(X)$.

Using this notation we can rephrase the previous statement by saying that we want to "count" the elements of $Z_k(X)$ that are not in $B_k(X)$. In algebraic terms this is done by taking the quotient group of $Z_k(X)$ by $B_k(X)$, but in order for this to be possible we need $B_k(X)$ to be a subgroup of $Z_k(X)$. This is guaranteed by the following proposition.

Proposition 2.1.15.

$$\partial \circ \partial = 0.$$

Proof. See [33]. □

Due to the fact that $\partial^2 = 0$ (Proposition 2.1.15), we have that $B_k(X)$ is a subgroup of $Z_k(X)$. Therefore we can define their quotient group as below.

Definition 2.1.16. *The k^{th}* (cubical) homology group *of X is the quotient group*

$$H_k(X) := Z_k(X)/B_k(X).$$

The homology of X is the collection of all homology groups of X. The shorthand notation for this is

$$H_*(X) := \{H_k(X)\}_{k\in\mathbb{Z}}.$$

Before we discuss the algorithms used to compute homology, let us look at the geometrical interpretation of the homology groups of a cubical set X. For a cubical set $X \subset \mathbb{R}^d$ it can be shown that, for $i = 0, \ldots, d-1$, $H_i(X) = \mathbb{Z}^{\beta_i} \oplus \mathbb{Z}_{b_1} \oplus \mathbb{Z}_{b_2} \oplus \cdots \oplus \mathbb{Z}_{b_k}$, where β_i is a nonnegative integer, $\mathbb{Z}_b$ denotes the group of integers modulo b, $b_i > 1$ provided $k > 0$, and b_i divides b_{i+1} for $i \in \{1, 2, \ldots, k-1\}$ provided $k > 1$. For $i \geq d$ we have $H_i(X) = 0$ (see [33]). The integer β_i is called the ith *Betti number* of X, and the numbers $b_1, b_2, \ldots, b_k$ are the *torsion coefficients* of

$H_i(X)$. For spaces with dimension $d \leq 3$ we do not have the torsion coefficients, that is, we just have $H_i(X) = \mathbb{Z}^{\beta_i}$. The Betti numbers carry the following geometrical information: β_0 is equal to the number of connected components (pieces) of X (see [33, Theorem 2.59]); β_1 is equal the number of holes (loops) if $d = 2$ and equal the number of tunnels if $d = 3$; as for β_2 it is equal the number of voids (as the one inside a basketball) if $d = 3$. For a more detailed discussion see [33].

2.2 Algorithms to Compute Homology

In this section we discuss the algorithms used to compute homology. The computation of homology is done basically in two steps. The first step is the geometric cubical reduction [50], in which cubes are removed from the cubical complex in such a way that homology is preserved. This reduction is illustrated in Figure 20.

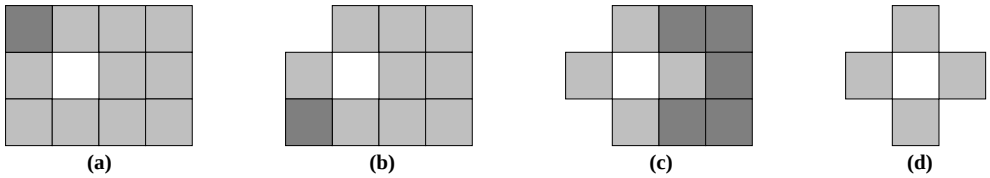

Figure 20: Example of cubical reduction. The shaded cube in (a) can be removed without changing the homology. After removing this cube we get the cubical complex in (b), where again the shaded cube can be removed to get the complex in (c). After removing all the shaded cubes in (c) we get the final complex (d) where no more cubes can be removed.

Before we describe the reduction algorithm we need to introduce some terminology. We say that a cubical complex $X \subset \mathcal{K}^d$ is *acyclic* if its homology is trivial (the same as that of a point), i.e., $H_0(X) = \mathbb{Z}$ and $H_i(X) = 0$ for $i > 0$. The *geometrical realization* of X is the set $|X| := \bigcup X \subset \mathbb{R}^d$. Using these notations we can describe the reduction algorithm [50, Algorithm 4.1].

Input : Cubical complex X
Output: Reduced cubical complex X

while *Exists* $Q \in X$ *such that* $Q \cap |X \setminus Q|$ *is acyclic* **do**
    $X := X \setminus \{Q\}$;
end

Algorithm 1: `CubicalReduction`.

The reduction algorithm is the fastest part of the whole process of homology computation, since to decide if a cube can be removed all one needs to know is which of its neighbors are present in the

cubical complex (as opposed to the next step in homology computation where we need information about the faces of all dimensions of the cubes, as it will be describe below). Once we know which neighbors are present we can easily decide if they form an acyclic complex or not, by computing their homology for example. In dimensions two and three we can create lookup tables to decide when a given cube is removable or not based on which of its neighbors are present. Figure 21 shows some sample 2-dimensional configurations. In dimensions higher than three the size of the lookup table would be too large for practical purposes.

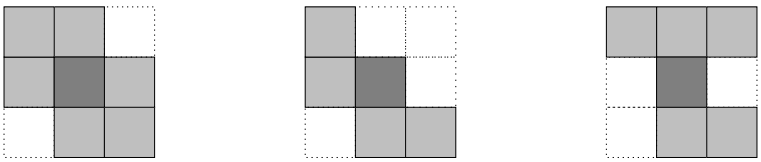

Figure 21: The center cube (dark shaded) is not removable in (a) and (c) since its present neighbors (light shaded cubes) do not form an acyclic complex. In (a) $H_1 = \mathbb{Z}$ and in (c) $H_0 = \mathbb{Z}^2$. It is removable in (b) since its neighbors do form an acyclic complex.

The cubical reduction usually decreases considerably the size of the complex, which makes the next step in the computations much faster. As it was mentioned before for the second step in the homology computations we need information about the faces of all dimensions of the cubes and the interconnections between them (see [34]). Before starting to describe the algorithms we need to introduce some notations.

Definition 2.2.1. *Let $X \subset \mathbb{R}^d$ be a cubical set. Given a k-chain $y \in C_k(X)$, the* coboundary *of y, denoted δy, is the set of $(k+1)$-chains defined by*

$$\delta y := \{z \in C_{k+1}(X) \mid y \in \partial z\}\,.$$

In what follows we will not distinguish between a k-cube and its dual k-chain, and we will refer to both as a k-cell. Given a k-cell z, the i-dimensional cells composing z are called the *i-faces* of z. For example the 2-cell $z = [0,1] \times [0,1]$ contains four 0-faces (the four vertices), four 1-faces (the four edges), and one 1-face (the cube $[0,1]^2$ itself). The data structure used to store the cubical complex X is a binary tree whose *levels* will be numbered from 0 (at the root) to M. Level M is said to be at the *bottom* of the tree and is referred to as the *depth* of the tree. We create this tree by

selecting a box B_0 such that B_0 contains the cubical complex X. This initial box is represented as the root of the tree. We then divide this box in half along the first component (x_1). Make a left child corresponding to the left half in case this half intersects X, and make a right child corresponding to the right side in case it intersects X. Now repeat the process for each node of the tree (for each of the last boxes created), only that now subdivide each box along the next component (along x_2 in the second step). Repeat this process until each box has unit size. Figures 22 and 23 illustrate this process.

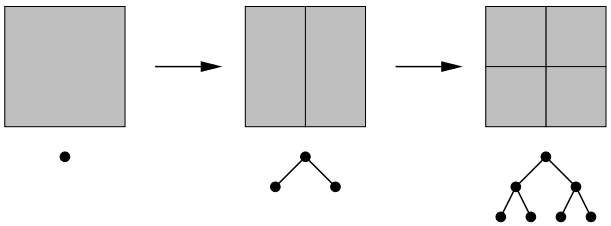

Figure 22: Example of a binary tree with depth $M = 2$ representing a cubical complex. The initial box (left) is represented by the node of the tree. The box is then subdivided and the newly created boxes are represented by nodes of the tree. The boxes in the final subdivision (right) are represented by the leafs of the tree.

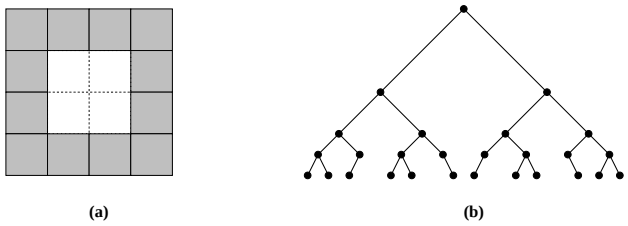

Figure 23: Tree with depth $M = 4$ (b) representing the cubical complex (a).

All the algorithms described next are from [34], and use two fundamental data types: cells and blocks. A *cell* is described by its dimension, boundary list, coboundary list, and simplification status which will be denoted by its *simplify-flag*. The *boundary list* of a k-cell, y, is the list of the $(k-1)$-cells in ∂y. Similarly the *coboundary list* of a k-cell, z, is the list of the $(k+1)$-cells in δz. A *block* represents a node in the binary tree and is composed of lists of cells of each dimension $0, \ldots, d$. In summary, the global data structure consists of a binary tree whose elements are blocks containing various lists of cells. We will first present all the algorithms, and then describe geometrically what each one does.

Input : Position at the bottom level of the binary tree
Output: Block containing a cubical d-cell and all its lower dimensional faces

Create vertices from position in binary tree;
Create faces of dimension $1, \ldots, d-1$;

Algorithm 2: `CreateCube.`

Input : Four subblocks of level $l-1$
Output: One unsimplified block at level l

Compare block boundaries and identify common cells;
Merge boundary and coboundary lists of common cells;

Algorithm 3: `ConcatenateBlocks.`

Input : Block of cubical complex
Output: Block containing only cells that can not be removed

```
1  Mark simplify-flag to true for all vertices not on the block boundary;
2  Mark simplify-flag to true for all cells containing a marked vertex;
3  for p = 0 to p = d − 1 do
4      while block cell list of dimension p is non-empty do
5          b = next cell with simplify-flag true;
6          if c ∈ δb then
7              X := δb − {c};
8              Y := ∂c − {b};
9              for each x ∈ X do
10                 replace b in ∂x by Y;
11             end
12             for each y ∈ Y do
13                 add X to δy;
14             end
15             Delete b and c;
16         end
17     end
18 end
19 while block cell list of dimension 0 is non-empty do
20     if v is interior to block then
21         delete v and δv from block cell lists;
22     end
23 end
```

Algorithm 4: `SimplifyBlock.`

Input : Node at current position in the tree
Output: Block at the input node containing all cells from branches below the input node which remain after recursive simplification

```
1  if Node at bottom level then
2  |  return
3  end
4  SimplifyBranch to the left;
5  SimplifyBranch to the right;
6  if both branch nodes are non-empty then
7  |  if current node level is a multiple of d then
8  |  |  ConcatenateBlocks ;
9  |  else
10 |  |  Store subblocks from both branch nodes;
11 |  end
12 end
13 if current node level is a multiple of d then
14 |  SimplifyBlock at this node;
15 end
```

Algorithm 5: `SimplifyBranch`.

Input : List of all bottom level positions in the tree describing the complex
Output: Simplified complex containing no cells with incidence number ± 1

```
1  CreateCube at left-most position in bottom level of the tree;
2  while new positions at bottom level do
3  |  Compute common node between current position and previous one;
4  |  SimplifyBranch to the left at common node;
5  |  CreateCube at current node;
6  end
7  SimplifyBlock at root node with all cells marked as simplifiable;
```

Algorithm 6: `ComputeHomology`.

Let us now describe geometrically what each one of the algorithms above does. The algorithm `ComputeHomology` starts by creating the cubes at the left-most position in the bottom of the tree, then it calls the algorithm `SimplifyBranch` on their parents, and after that it keeps creating the nodes at one level up the tree and calling `SimplifyBranch`. The algorithm `SimplifyBranch` on its hand essentially just calls `SimplifyBlock` to simplify the blocks and then calls the algorithm `ConcatenateBlocks` to concatenate the simplified blocks. Let us illustrate this whole process with one example. Initially `ComputeHomology` just creates the nodes at the bottom of the tree, this is essentially equivalent to subdividing the complex X in small subcomplexes as is illustrated in Figure 24. After that `ComputeHomology` will call `SimplifyBranch` to simplify each subcomplex.

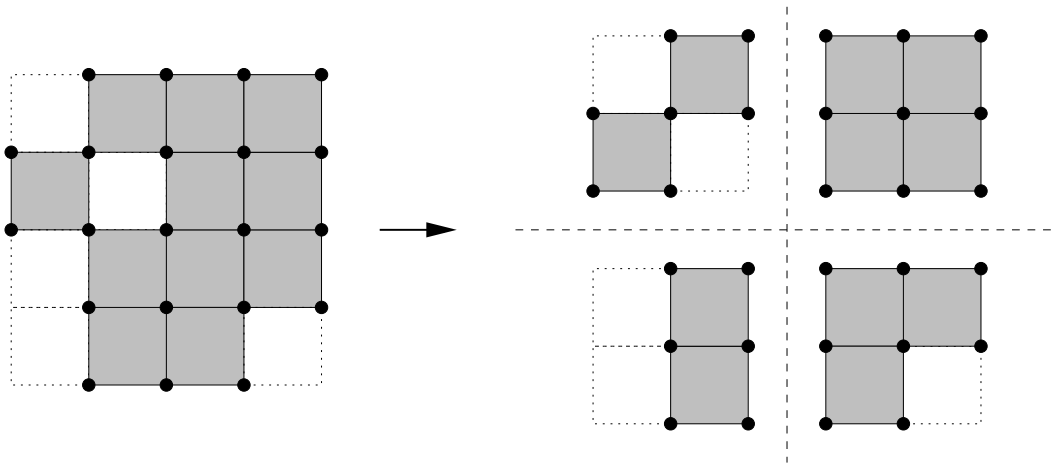

Figure 24: `ComputeHomology` will subdivide the complex on the left into the four complexes on the right and call `SimplifyBranch` to simplify them.

The algorithm `SimplifyBranch` will call `SimplifyBlock` to simplify each subcomplex, and then concatenate them. So let us now illustrate how `SimplifyBlock` would simplify the subcomplex on the top left of the right diagram in Figure 24. The steps taken by `SimplifyBlock` are shown in Figure 25. First `SimplifyBlock` tries to remove the internal vertices. In this case only the central vertex is internal in (a), so it is removed by collapsing the vertical edge above it to produce (b). At this point we no longer have a cubical complex, but rather a CW-complex (see [54]). In (b) there are no more internal vertices, so the next step is to try to remove internal edges. There are two removable internal edges, and their removal is shown in (c) and (d). In the final position (d) there is one internal edge, but it has no coboundary so it can not be removed. Therefore (d) is the simplified complex returned by `SimplifyBlock`.

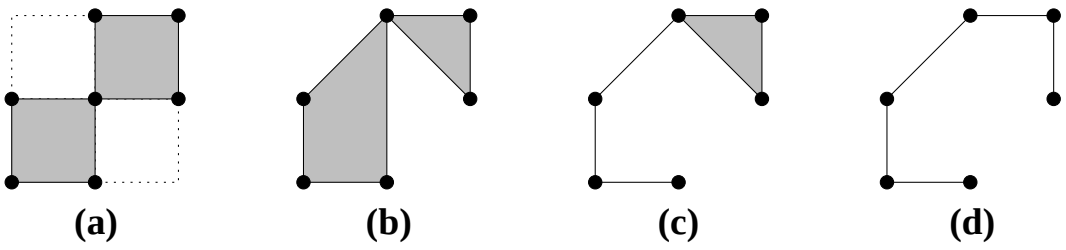

Figure 25: Complex in (a) is simplified to the complex in (d) by `SimplifyBlock`.

The result of `SimplifyBlock` in the four subcomplexes on the right of Figure 24 is shown on the

left of Figure 26. Once they have been simplified, `SimplifyBranch` will call `ConcatenateBlocks` to concatenate them. The result is shown on the right of Figure 26. Notice that `SimplifyBlock` does not remove cells on the boundary of the blocks, since they will be needed in the concatenation step.

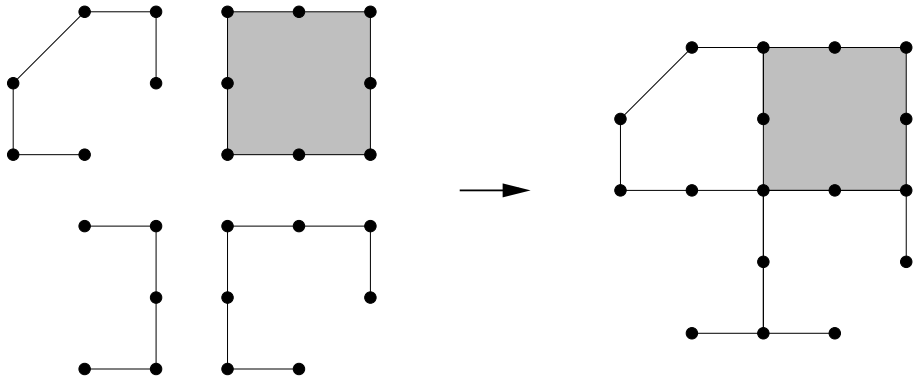

Figure 26: `ConcatenateBlocks` concatenates the four complexes on the left to the one on the right.

Once the four blocks have been concatenated, the algorithm `SimplifyBranch` will once again call `SimplifyBlock` to simplify the result. This process is illustrated in Figure 27, where several steps have been omitted. From (a) to (b) all the internal vertices are removed, and from (b) to (c) the only removable internal edge is removed. Notice that there are three internal edges in (c), but they are not removable, since they have no coboundary.

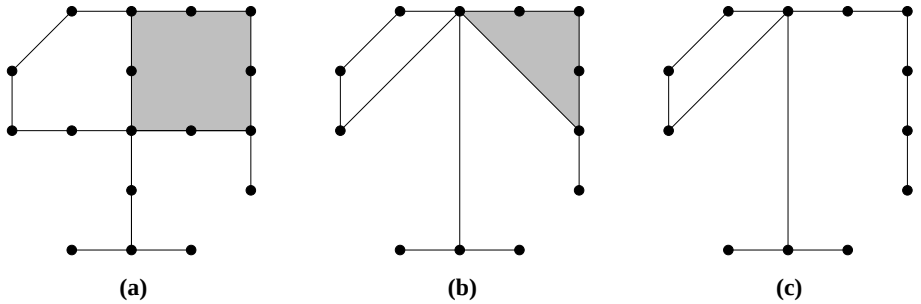

Figure 27: Complex in (a) is simplified to the complex in (c) by `SimplifyBlock`.

When we get the complex in Figure 27 (c) we exit the while loop in `ComputeHomology`. The next step is to call `SimplifyBlock` at this complex with all cells marked as simplifiable. We can do that because this is the entire complex (or what is left of it), and so we can remove boundary

cells, since we will not need to concatenate blocks anymore. This is illustrated in Figure 28, where several steps have been omitted. When we get to the final complex in Figure 28 (d), the ith Betti number is just the number of i-cells left. In this particular example we get $\beta_0 = 1$ and $\beta_1 = 1$, which is the correct homology of the initial complex (Figure 24 left).

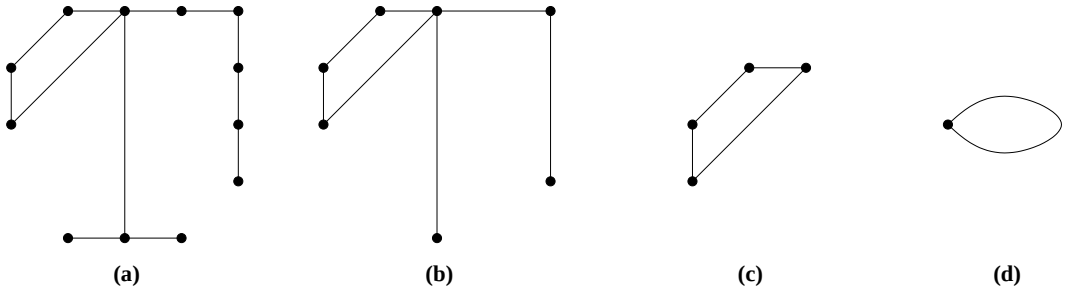

Figure 28: `SimplifyBlock` with all cells marked as simplifiable transform the complex in (a) into the complex in (d).

The procedure used to compute the homology groups of a cubical complex X is to use the algorithm `CubicalReduction` to reduce the initial cubical complex and to feed the resulting complex to `ComputeHomology`. It is important to note that in all the algorithms above only local computations are performed. The implementation of the algorithms take advantage of this fact and loads only part of the complex into memory at each step. This allows for computations with large cubical complexes, which do not fit into memory all at once. The implementation of the algorithms used in this thesis can be found at [35].

2.3 Correctness of Homology under Cubical Approximation

In this section we discuss how the cubical approximation may affect the correctness of the homology groups. The following example (from [33]) illustrates a case where the cubical approximation does not capture the correct homology of the object being approximated. Consider the two line segments in Figure 29 (a). They form only one component and no holes, so they have trivial homology. In Figure 29 (b) we show a cubical approximation of the two line segments, obtained by selecting all cubes that intersect them. Notice that the homology of the cubical approximation is non-trivial, since $H_1 = \mathbb{Z}$. Notice also that refining the grid does not solve the problem, as it is shown in Figure 30.

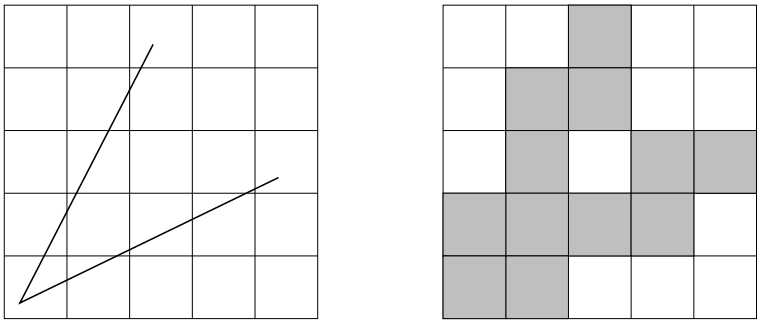

(a) **(b)**

Figure 29: The shaded cubes in (b) are a cubical approximation for the two line segments in (a). Notice that the cubical approximation does not capture the correct homology of (a).

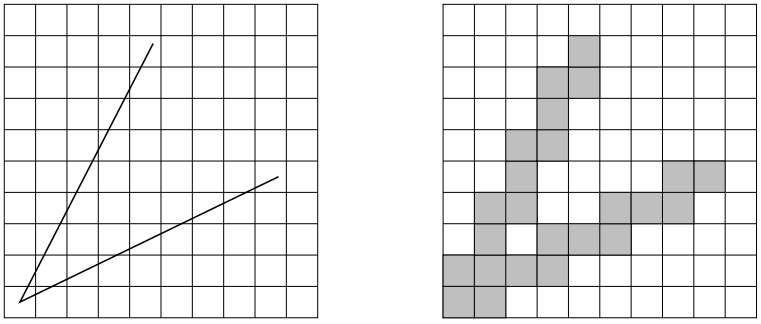

(a) **(b)**

Figure 30: Refinement of the grid used to construct the cubical approximation in Figure 29. Notice that even with the finer grid the cubical approximation still have the wrong homology.

This example shows us that the cubical approximation may not always capture the correct homology. So care should be taken when using a cubical approximation to compute homology. The problem in the previous example comes from the fact that Figure 29 (a) contains a corner point. If the object being approximated is smooth enough, then the correct homology can probably be obtained as long as we use a fine enough grid.

The previous discussion shows that, even when we have an exact representation of the object we want to compute the homology of, we may not be able to compute the correct homology. In this thesis we are computing homology of sets obtained experimentally (which therefore are noisy) and by numerically solving differential equations (which therefore contain numerical errors). We have then yet another source of possible errors in the homology computations. These are issues that should be taken into consideration when using the techniques presented in this thesis. Let us first

point out that assuring that the homology computations are correct in this context is a very hard problem, and will not be solved in this thesis. We will however discuss some results that suggest that, for the kind of spaces we consider here, it may be possible to compute the correct homology most of the time. For this purpose we will use recent results by Niyogi, Smale and Weinberger [57] on computing homology from random samples.

We first need to introduce some preliminary notations. Consider a compact Riemannian submanifold $M \subset \mathbb{R}^d$. Sample points $x_1, \ldots, x_n$ in the manifold according to a uniform probability measure on it. The set of points $\bar{X} := \{x_1, \ldots, x_n\}$ will be the data used to compute the homology of M, and we will next discuss conditions under which the correct homology can be obtained. Given the set $\bar{X}$ we consider euclidean balls, $B_\epsilon(x_i) \subset \mathbb{R}^d$, of center x_i and radius ϵ. We then define the open set $U \subset \mathbb{R}^d$ by

$$U := \bigcup_{x \in \bar{X}} B_\epsilon(x),$$

and investigate conditions under which the homology of U is the same as the homology of M. We associate to M a condition number, $1/\tau$, where τ is defined as the largest number having the property: The open normal bundle about M of radius r is embedded in $\mathbb{R}^d$ for every $r < \tau$. The condition number $1/\tau$ limits the curvature and nearness to self-intersection of the submanifold (see [57]). In Figure 31 we show some examples in which the condition number is large.

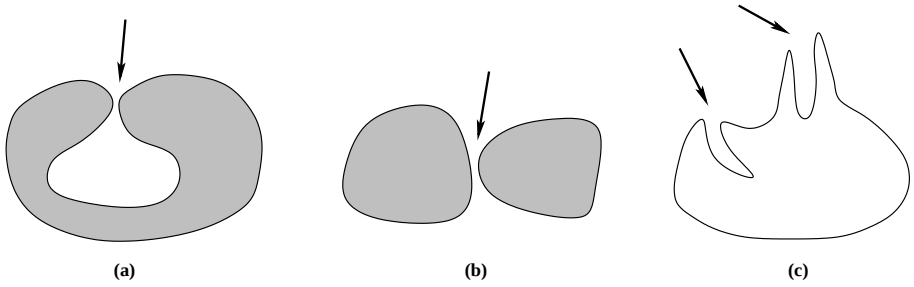

Figure 31: Examples of manifolds with large condition number due to a nearly self-intersecting component (a), two nearly intersecting components (b), and regions with high curvature (c). The arrows just indicates the regions of nearly intersection and high curvature. The submanifolds in (a) and (b) are 2-dimensional and the submanifold in (c) in 1-dimensional (all embedded in $\mathbb{R}^2$).

We then have the following theorem.

Theorem 2.3.1 ([57] Theorem 3.1). *Let M be a compact submanifold on $\mathbb{R}^d$ with condition number*

$1/\tau$. Let $\bar{X} = \{x_1, \ldots, x_n\}$ be a set of points drawn in i.i.d. (independently and identically distributed) fashion according to a uniform probability measure on M. Let $0 < \epsilon < \sqrt{\frac{3}{5\tau}}$, $0 < \delta < 1$, and $U = \cup_{x \in \bar{X}} B_\epsilon(x)$. Then for all

$$n > \beta_1 \left(\log(\beta_2) + \log(1/\delta)\right)$$

the homology of U is equal the homology of M with high confidence (probability $> 1 - \delta$). Here $\beta_1 := \frac{vol(M)}{(\cos(\theta))^d vol(B_\epsilon^d)}$ and $\beta_2 := \frac{vol(M)}{(\cos(\theta))^d vol(B_{\epsilon/8}^d)}$, where $vol(B_\epsilon^d)$ denotes the d-dimensional volume of a d-dimensional ball of radius ϵ, and $\theta := \arcsin(\frac{\epsilon}{2\tau})$.

The previous theorem says that if we take a large enough number of samples from the manifold, then we can recover its homology by computing the homology of a union of balls in the embedding space $\mathbb{R}^d$. When we generate patterns by thresholding a numerical solution of a differential equation, we select the grid points whose solution is above the threshold and color the corresponding cube (in the cubical grid used in the numerical integration) as part of the pattern. Therefore we are sampling the manifold (selecting the grid points above the threshold) and taking balls around the sampled points, just that in this case we use a metric where the balls are cubes. The problem is that the points we select (the sampled points) are not necessarily on the manifold. The numerical solution at a given point may be above the threshold, but the actual solution may not, due to numerical errors. But let us for the moment assume that we have the exact value of the solution at the grid points, that is, let us assume we have no numerical errors. Then we could try to apply the above theorem to guarantee that we can compute the correct homology. The problem is that we may not be able to satisfy the hypotheses of the theorem. One restriction we may have is that the region we want to compute the homology of may not be a manifold. This would be the case if we had, for example, a 2-dimensional region that forms a figure eight, that at a latter point in time separate into two disconnected regions. At the exact time when the two regions separate, the point at which they are connected is a corner point, and we therefore would not have a manifold. At this time the level curves would also have "infinite curvature" at this corner point. So we would again not be able to apply the previous theorem to this level set. One third problem we may have is that portions of time-varying patterns may collide, as it happens in the spiral wave patterns for example, and at the moment of the collision the condition number would be "infinity". Even in the cases where

we could apply the thorem, we would need to find bounds on the condition number $1/\tau$ to know how fine a grid (that is, how many points and how small the balls should be) we would need to obtain the correct homology. Finding bounds on $1/\tau$ for the level sets of a solution of a differential equation is a very hard problem that we will not attempt to solve in this thesis. Even though we can not apply the above theorem to all the regions we want to compute the homology of, it tells us that we may be able to obtain the correct homology in the cases when we do not have the problems mentioned above. In conclusion, even though we can not guarantee that we can compute the correct homology, the above theorem suggests that we make mistakes "only" when our regions are not nice and smooth.

The conclusions from last paragraph are all based on the assumption that we know the exact value of the solution at the grid points. This is, of course, not true if we are solving the differential equation numerically. In general we know that the numerical solution is a reasonable approximation to the actual solution. So we therefore need to be able to deal with the case where the sampled points are not exactly on the manifold, but are near it. The next theorem is a step in this direction. We now assume that the data is noisy in the sense that it is drawn from a probability distribution that is concentrated around (rather than on) the manifold. So we therefore assume that $\bar{X} = \{x_1, \ldots, x_n\}$ is a set of points in the tubular neighborhood of radius r around M, sampled according to a probability measure μ satisfying the following regularity conditions.

1. The support of μ is contained in the tubular neighborhood of radius r around M.

2. For every $0 < s < r$, we have that $\inf_{p \in M} \mu\left(B_s(p)\right) > k_s$, where k_s is a constant depending on s and independent of p.

Assuming the setting above we have the following theorem.

Theorem 2.3.2 ([57] Theorem 7.1). *Let M be a compact submanifold on $\mathbb{R}^d$ with condition number $1/\tau$. Let $\bar{X} = \{x_1, \ldots, x_n\}$ be a set of points, in the tubular neighborhood of radius r around M, drawn in i.i.d. fashion according to a probability measure μ satisfying the above regularity conditions. Let $0 < \delta < 1$, and $U = \cup_{x \in \bar{X}} B_\epsilon(x)$. Then for all*

$$n > \frac{1}{k}\left(\log(N_{r/2}) + \log(1/\delta)\right)$$

the homology of U is equal the homology of M with high confidence (probability $> 1-\delta$), as long as $r < \tau\left(\sqrt{9} - \sqrt{8}\right)$ and $\epsilon \in \left(\frac{(r+\tau)-\sqrt{r^2+\tau^2-6\tau r}}{2}, \frac{(r+\tau)+\sqrt{r^2+\tau^2-6\tau r}}{2}\right)$. Here $N_{r/2}$ is the $r/2$-covering number of the manifold M.

What this theorem tells us is that if we sample the points close enough to M, we know how close to M they are (we know r), and we know the condition number $1/\tau$, then we can estimate how many points we need to sample to get the correct homology. So in principle one could try use this theorem to justify the homology computations of data contaminated by numerical errors and/or experimental noisy. However, we would still have similar problems as the ones with the previous theorem. So we again can not directly apply this theorem to all of our regions, but it suggests that we may be able to get the correct homology if our regions are smooth enough and the noise and/or numerical errors are sufficiently small.

2.4 Why Homology?

In this section we discuss why one should use computational homology the analyze the kind of patterns discussed in this thesis. As we already mentioned in the introduction, in dimensions two and three one could use alternate ways to compute the number of components and loops.

First let us describe how the number of components can be computed without using homology. Given the cubical complex we define a graph which has one node for each cube in the complex, and we define a graph edge connecting two nodes if the corresponding cubes are neighbors (if they intersect). In this way the number of connected components in the graph is the same as the number of connected components in the cubical complex. Then we can just use standard graph algorithms to compute the number of connected components (see [15]). This method works for arbitrary dimensions and the available graph algorithms are faster than the homology computation algorithms. Therefore if all one cares about is the number of connected components, then there are methods more efficient than the homology algorithms presented here.

Next let us discuss how one can compute the number of holes (loops) in a 2-dimensional cubical complex. We can again define a graph whose edges are all the edges in the cubical complex which are the intersection of a cube in the complex and a cube in the complement, and that are not on the exterior boundary of the complex. The nodes of the graph will be the vertices on the cubical

complex corresponding to the selected edges. Defined this way the number of loops in the graph is the same as the number of holes in the complex (see [15]). Also in this case, more efficient algorithms are available.

Finally in dimension three one could compute the Euler characteristic, just by adding up the Euler characteristic of each cube. The Euler characteristic is equal $\beta_0 - \beta_1 + \beta_2$. So it provides us some information about the homology of the cubical complex.

The cases discussed above are information we can compute without using homology. Now if we are interested in higher dimensional objects, then we need to use homology. In Chapter 1 we discussed the homology computation of 2-dimensional spiral waves, and we argued that to understand the 2-dimensional patterns one need to compute the homology of 3-dimensional complexes (see Figure 15). So if we want to understand 3-dimensional spiral waves, the objects we need to analyze are 4-dimensional objects. Therefore computation of homology in dimension four may be necessary even to understand a system that produces 3-dimensional patterns. In this case other techniques are not available, and homology is necessary.

Another reason why homology may be preferable is to understand boundary effects. Consider the patterns in Figure 32. They show one of the patterns in Figure 8, where the number of components and the number of loops are highlighted.

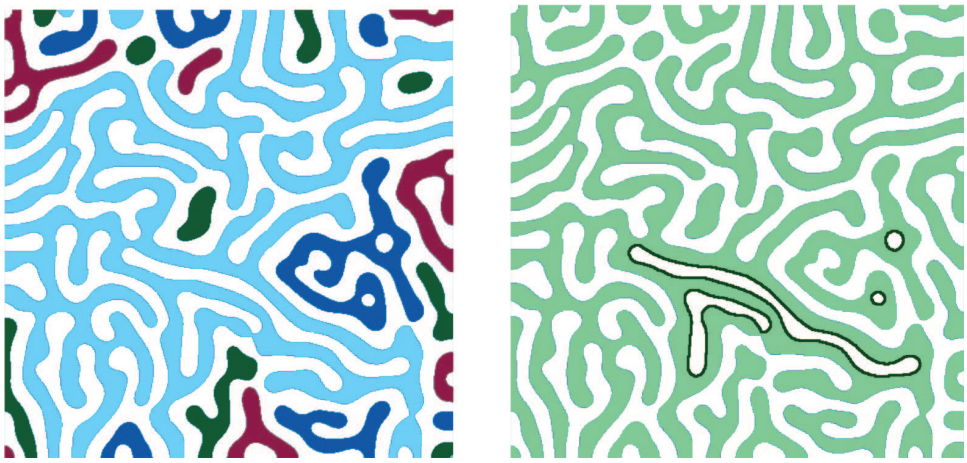

Figure 32: Betti numbers for the $X^+(t)$ region of the $\sigma = 0$ and $t = 0.0036$ snapshot from Figure 8. The left diagram shows the $\beta_0 = 26$ distinct components, with neighboring components distinguished by different colors. The right diagram indicates the boundaries of the $\beta_1 = 4$ loops.

The picture on the right of Figure 32 shows the $\beta_1 = 4$ loops in $X^+(t)$ (colored region). Notice that these loops enclose components of $X^-(t)$ (white region). Notice also that these enclosed components are the only ones that do not touch the boundary of the square. Therefore by using the homology of both regions we can compute the number of internal components and the number of components connected to the boundary. Denoting the number of internal components by $\beta_{int,0}$ and the number of boundary components by $\beta_{bdy,0}$, we have the formulas

$$\beta_{int,0}(X^+) := \beta_1(X^-), \quad \text{and} \quad \beta_{bdy,0}(X^+) := \beta_0(X^+) - \beta_{int,0}(X^+).$$

Analogous formulas are used for X^-. These formulas can also be generalized to higher dimensions. This shows that homology gives us an easy way to characterize internal and boundary effects. This is another reason why it may be useful to use homology. It is important to notice that the formulas above are correct only when the homology computations are correct. If there are mistakes in the homology groups (as discussed in the previous section), then the formulas above may not produce correct results.

The moral of this section is that homology theory provides a general framework for our proposed topological analysis of patterns, which will work in arbitrary dimensions. It also provides more information than other available methods (like the Euler characteristic for example). However if one is interested only in low dimensional complexes and/or wants to compute just the number of components or the Euler characteristic, then more efficient methods can be used.

CHAPTER III

SPIRAL DEFECT CHAOS IN RAYLEIGH-BÉNARD CONVECTION

3.1 Introduction

Characterization of geometric structures (patterns) in physical systems can give insight into underlying dynamics. For simple cases, pattern characterization is easily done with a few numbers (e.g. the lattice constants describing problems with crystalline symmetries). However encoding patterns becomes more difficult as patterns become more complex. Statistical approaches can be used to describe complex patterns in dynamically evolving systems [52, 18]; however, a general methodology for extracting geometric signatures from complex patterns has been lacking.

In this chapter we use homology to extract consistent and robust geometric properties from experimental observations of spatiotemporal complexity. Hydrodynamic systems readily produce complex spatiotemporal patterns [46], which are ideal for testing these techniques. We use Betti numbers to characterize dynamically relevant features in a weakly turbulent state of Rayleigh-Bénard convection (RBC) known as spiral defect chaos (SDC) (see [51] and Figure 34). In particular, we find that: (a) the geometric structures of asymptotic states of SDC are readily distinguishable as a function of a control parameter; (b) the entropy of the SDC attractors quantifies the evolution of the system through different geometric configurations; (c) the asymptotic global geometric configurations seems to evolve stochastically; (d) symmetry breaking in the flow patterns is readily detectable in cases where simple statistical measures (e.g., measurements of mean pattern volumes) are insensitive to pattern asymmetries; and (e) the boundary and bulk patterns can be distinguished.

3.2 Experimental Setup

The experiments were performed in Michael Schatz's laboratory at Georgia Tech. In these experiments convective flow is measured in a 0.069 cm deep horizontal layer of CO_2 gas at a pressure of 3.2 MPa in a convection cell bounded above by a 2.54 cm thick sapphire crystal (the top plate) and

below by a 5 cm in diameter and 0.6 cm thick gold coated aluminum mirror (the bottom plate). The lateral walls are circular, formed out of an annular stack of filter paper sheets 3.8 cm in diameter. An electrical resistive heater is used to heat the bottom mirror, and the top window is cooled by circulating chilled water at 21.2 ^{o}C. The container for the convection cell is an Aluminum cylinder 6.75 cm high with 6.93 cm inner diameter and 8.95 cm outer diameter. A schematic of the experiment is detailed in Figure 33.

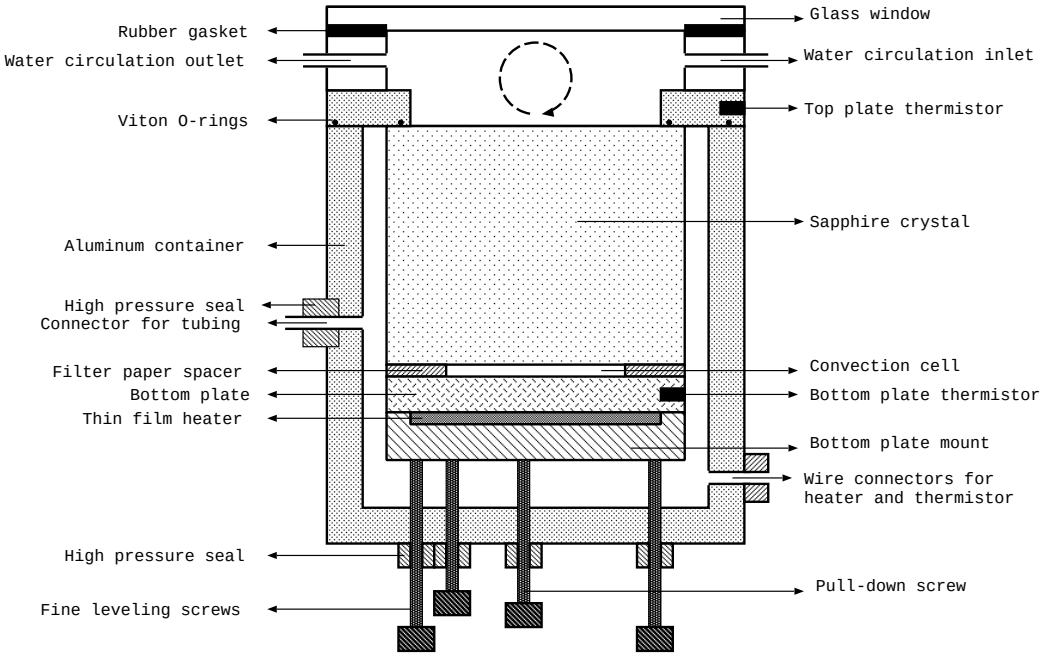

Figure 33: Schematic of the convection cell.

When the vertical temperature difference, ΔT, across the gas exceeds a critical temperature difference, $\Delta T_c \approx 4$ ^{o}C, the onset of fluid motion occurs. The flow organizes into a pattern of convective rolls where hot regions of the gas move upward and cold regions flow downward. The convection rolls become spatially disordered and exhibit complex time dependence when the system control parameter $\epsilon = (\Delta T - \Delta T_c)/\Delta T_c$ (the reduced Rayleigh number) is sufficiently large. For the present study, the patterns are observed for the order of $10^3\tau_\nu$ ($\tau_\nu \approx 2.1$ seconds is the vertical thermal diffusion time). We consider time series of 18000 images for each value of ϵ in the range 0.125 to 4.125 stepped in increments of 0.125. We will present more details (like images of the patterns and plots of time series of Betti numbers) for the $\epsilon \approx 1.0$ and $\epsilon \approx 2.0$, and the more general

results for the other values of ϵ mentioned above.

Shadowgraph visualization of the convecting flow yields intensity images, which are used to compute the topology of the rolls in SDC (Figure 34). The shadowgraph technique is sensitive to the refractive index variations in the gas, which represents the temperature profile of the flow [64]. The state of the flow is sampled at 11 Hz by capturing raw intensity images [Figures 34 (a) & (b)] using a 12-bit digital camera; a background image of the fluid below the onset of convection is then subtracted to remove optical nonuniformities (e.g., optical imperfections in the bottom plate). Digital Fourier filtering is then applied to remove high wavenumber components due to camera spatial noise. The Fourier filter consists in simply computing the Fourier transform of the images, and removing the 5% highest frequencies. This eliminates all small scale defects as shown in Figure 34. The data is then converted to binary values by thresholding at the median value of intensity. The resulting images [Figures 34 (c) & (d)], where black represents hot upflow and white represents cold downflow, are used as input to computation of homology. In what follows, $X(n, \epsilon)$ represents the n^{th} binary image in a time series at the reduced Rayleigh number ϵ. Moreover, $X^{hot}(n, \epsilon)$ and $X^{cold}(n, \epsilon)$ denote the hot flow and cold flow regions, respectively, of $X(n, \epsilon)$. It is worth noticing that the number of pixels in $X^{hot}(n, \epsilon)$ is equal to the number of pixels in $X^{cold}(n, \epsilon)$, i.e., hot and cold regions occupy the same area in the pattern.

3.3 Parameter Distinction and Symmetry Breaking

The sequence of Betti numbers can be used to clearly distinguish different complex states of SDC (Figure 35). For the Rayleigh numbers $\epsilon \approx 1.0$ and $\epsilon \approx 2.0$ Figure 35 shows a plot of the sequences of Betti numbers $\beta_i^{hot}(n, \epsilon)$ and $\beta_i^{cold}(n, \epsilon)$. Notice that the time average of the Betti numbers are different at different ϵ. One can also observe this difference in the main value of the Betti numbers in Figure 37 for several values of ϵ.

This difference in the mean values of the Betti numbers (Figure 37) reflects the instability mechanisms operating during the evolution of the complex spatiotemporal pattern in SDC. The dynamically significant events for the evolution occur in regions of local compression or dilatation of the roll structure. The compression leads to the merging of neighboring rolls while the dilatation results in the formation of a new roll in the pattern. Such local events change the topology of the pattern.

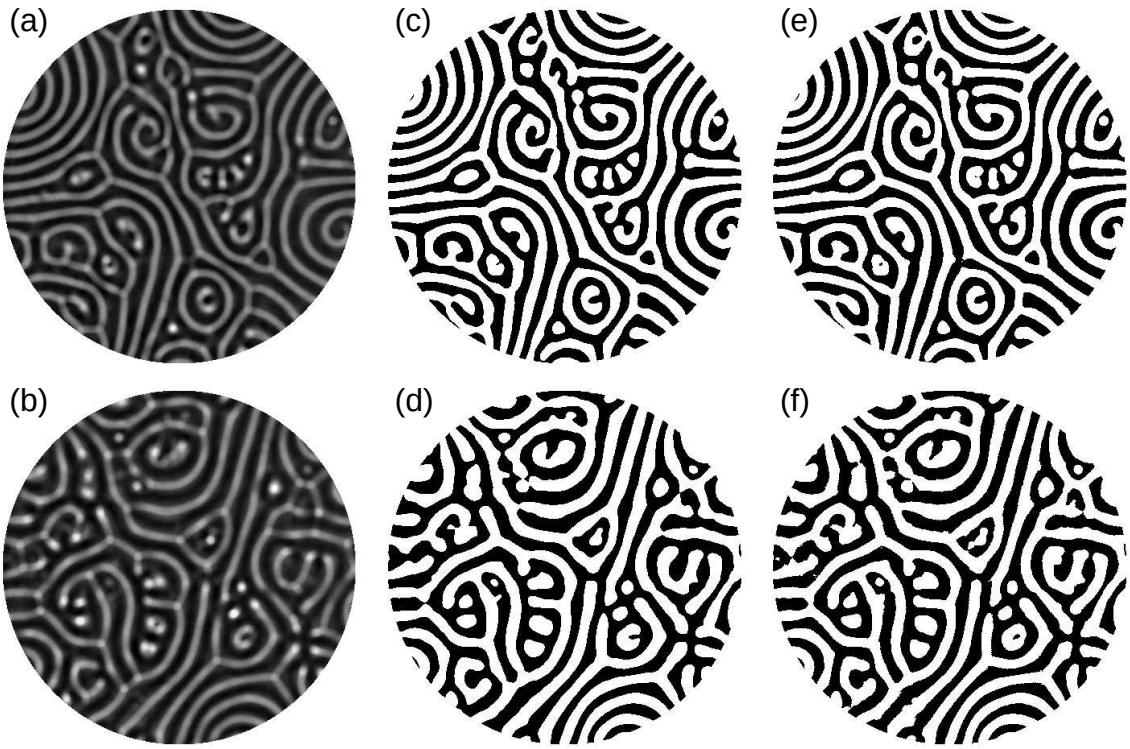

Figure 34: Shadowgraph images of spiral defect chaos convection patterns at reduced Rayleigh numbers $\epsilon \approx 1.0$ (a) and $\epsilon \approx 2.0$ (b) are converted to binary valued images [(c) and (d), respectively] by thresholding the data at the median value of intensity. In (c) and (d), the black regions correspond to hot upflow, and the white regions to cold downflow. Images (e) and (f) correspond to the images (c) and (d) respectively, before the Fourier filter is applied.

For instance, the merging of two rolls reduces the number of distinct rolls reducing β_0 by one. A pattern increasingly dominated by such instabilities would hence show an overall reduction in β_0 as different components link together locally at distinct locations. As the number of distinct rolls reduces, such linkages are often self-intersections of a roll. This manifests as an increase in the number of loops (β_1) in the pattern. The mechanisms characterizing the secondary instabilities for ideal straight rolls [6] have a similar structure and are known as the skew-varicose (compression) and the cross-roll (dilatation) instabilities. In spiral defect chaos such events are seen to be operational in regions localized by the curvature of the rolls.

The homology of the states exhibited by SDC uncovers a break in the symmetry between upflows and downflows. For an ideal Rayleigh-Bénard problem, as described by the Boussinesq equations [13], there is a midplane symmetry on the patterns. This symmetry of the flow (the Boussinesq

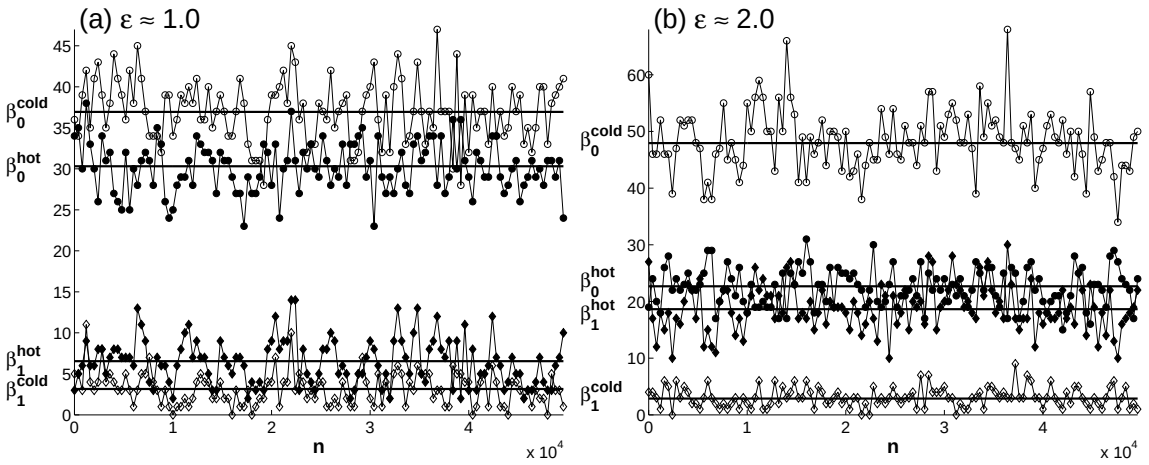

Figure 35: Time series of Betti numbers showing every 400th data point of the time evolution of the number of distinct components and holes in the regions X^{hot} (closed, black symbols) and X^{cold} (open, white symbols). Circles correspond to β_0 and diamonds to β_1. The horizontal lines indicate the mean values $\bar{\beta}_i(\epsilon)$ for the corresponding time series. Image (a) is for $\epsilon \approx 1.0$ and (b) for $\epsilon \approx 2.0$. The complete time series plots are qualitatively similar to the ones shown (see Figure 36), the data is partially sampled only for better visualization.

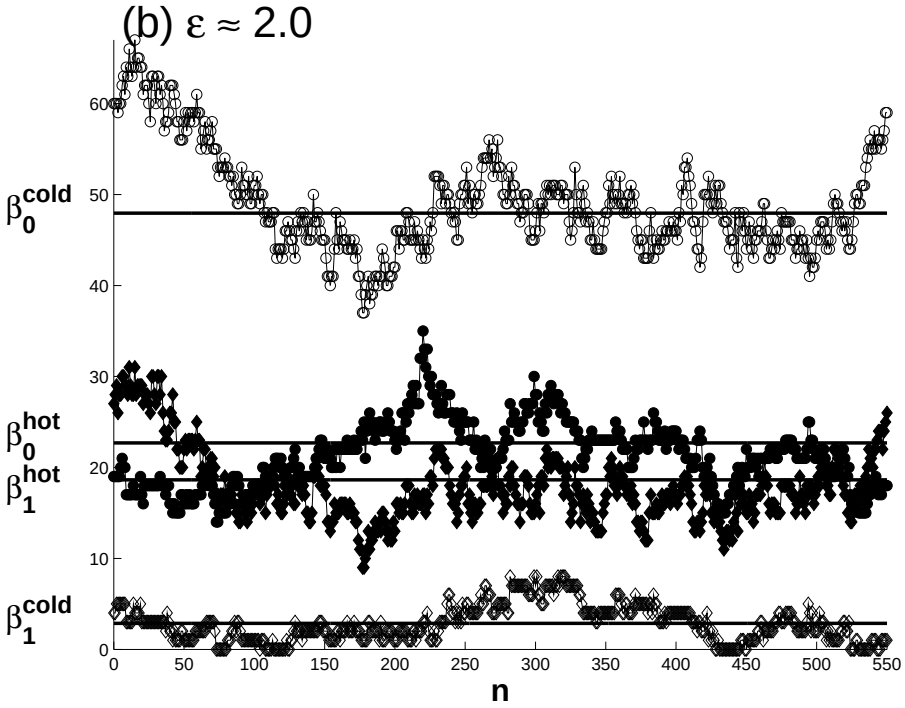

Figure 36: Plot of the first 550 points in the series of Figure 35 for $\epsilon \approx 2.0$, showing that the partially sampled data of Figure 35 is qualitatively similar to the whole time series.

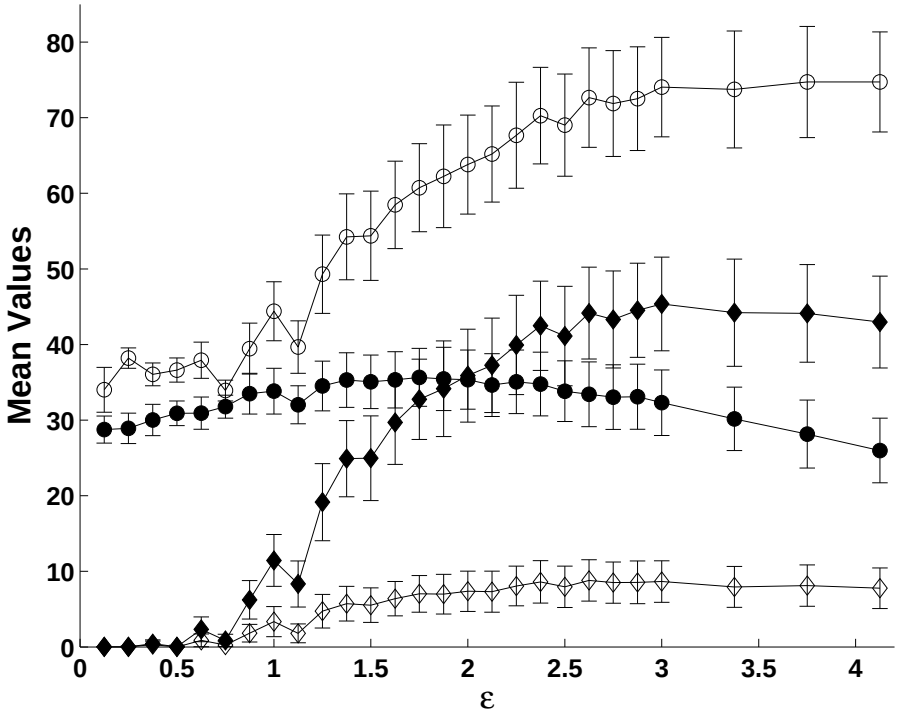

Figure 37: The mean values of the Betti number time series as a function of ϵ. The error bars indicate the standard deviation of the time series. Notice the asymmetry between hot upflow and cold downflow. Circles correspond to β_0 and diamonds to β_1. Closed symbols correspond to hot flows and open symbols to cold flows.

symmetry) in an ideal Rayleigh-Bénard problem suggests that the statistical properties of the patterns would be the same for X^{hot} and X^{cold}; in particular we should obtain $\bar{\beta}_i^{hot}(\epsilon) = \bar{\beta}_i^{cold}(\epsilon)$ for $i = 0, 1$. As Figure 37 indicates, in our experiments we found that that the mean values of the Betti numbers clearly distinguish between fluid regions comprised of hot and cold flows. Furthermore, this asymmetry is enhanced with an increase in the Rayleigh number. We suspect that the pattern homology serves as a sensitive detector of non-Boussinesq effects that are present due to the variation in physical properties of the fluid between the hot bottom layer and the cool top layer. The strength of non-Boussinesq effects in experiments can be estimated by a dimensionless parameter Q [6, 16] computed perturbatively at the primary instability for convection. In our experiments with CO_2, we find this parameter to be equal 0.54 near the onset of convection — thus indicating strong, $O(1)$, non-Boussinesq effects.

3.4 Entropy

At different parameter values, the state of SDC takes on different configurations. The set of Betti numbers describes the different patterns of rolls (states) attained by the system. A complete description of the homological configuration of the state is determined by the set of Betti numbers describing the hot and the cold regions.

We calculate the probability of being in a particular configuration from a long time series of Betti numbers for the evolution of the state. The probability is obtained by trivially counting the number of occurrences of the state defined by the vector $(\beta_0^{hot},\beta_1^{hot},\beta_0^{cold},\beta_1^{cold})$ over a long time series and normalizing by the total number of possible states. The probability distribution enables the computation of an entropy defined by

$$E = \sum_i p_i log(1/p_i),$$

where p_i denotes the probability of being in the state i, and the index i spans over all the different states attained by the system as characterized by the vectors of the form $(\beta_0^{hot},\beta_1^{hot},\beta_0^{cold},\beta_1^{cold})$. While the entropy is computed over the states attained by the system in a finite amount of time, its value seem to asymptote to a constant for long time series. In states where the components do not interact, the entropy reduces as a result of no fluctuations in the Betti numbers associated with defect formation. The entropy increases for attractors that show evolving topologies mediated through defects. The entropy of the system increases as a function of ϵ as is shown in Figure 38. This increase, however, is non-monotonic as one can observe dips in the entropy values.

The non-monotonic behavior of the entropy may indicate bifurcations. The second dip in the entropy occurs at $\epsilon = 1.25$ as indicated in Figure 38. Images corresponding to the values of ϵ just before, at, and just after $\epsilon = 1.25$ are shown Figure 3.4. The structure of the patterns seems to have a qualitative change from mostly parallel rolls at $\epsilon = 1.25$ to a more complex geometry at the other ϵ values, which confirms the possibility of a bifurcation taking place around $\epsilon = 1.25$. Similar phenomenon occurs at the value of ϵ corresponding to the other dip in the entropy plot.

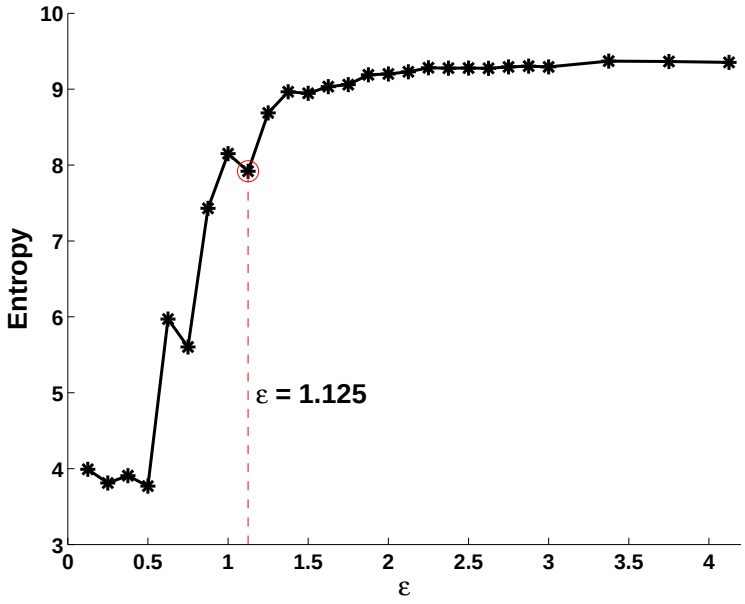

Figure 38: Entropy computed from the time series as a function of ϵ.

3.5 Stochastic Evolution

The evolution of complex geometries may be distinguished as being chaotic or stochastic from the time series of Betti numbers. In Chapter 5 we use the Betti numbers to uncover global chaotic evolution through the computation of the largest Lyapunov exponent. In our experiments on SDC we have been unsuccessful in extracting Lyapunov exponents using similar techniques. In the case of SDC a mechanism describing locally chaotic islands driving the complex dynamics has been proposed in [19, 20]. It is likely that the spatiotemporally localized nature of such instabilities in SDC decorrelates at a scale that is not effectively captured by the time series of Betti numbers; a succession of these local events interspersed across the system may cause effective stochastic evolution for the global geometric structure attained at the attractor. To first order we find it likely that the dynamics of fluctuations in the Betti numbers may be primarily stochastic in nature, as it is also suggested by the auto-correlation of the time series shown in Figure 40.

3.6 Boundary Effects

The pattern homology can also provide a well-defined way to separate boundary-driven effects from bulk phenomena in pattern forming systems. Typically, separating boundary behaviors from bulk

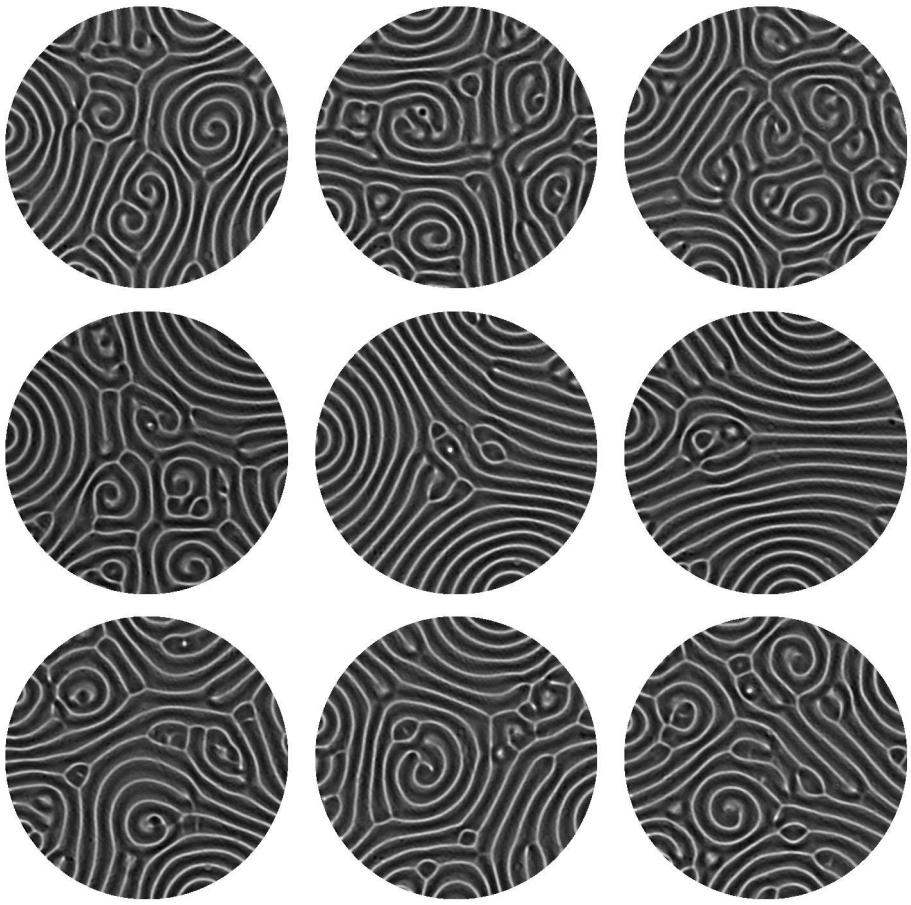

Figure 39: SDC patterns at different ϵ and for different times. The middle row is for $\epsilon = 1.25$ (which correspond to the second dip in the entropy plot of Figure 38), the top row corresponds to $\epsilon = 1.0$ (the value just before 1.25 in our experiments), and the bottom row corresponds to $\epsilon = 1.5$ (the value just after 1.25).

effects is done by setting a cutoff (say D), based on pattern correlation lengths, that measures the proximity to the boundary. Thus, patterns within D of the boundary are strongly influenced; patterns at distances $>> D$ are effectively free of boundary influences. Homology provides a different perspective: Boundary influence is measured not by *proximity* to the boundary but rather by *connectivity* to the boundary. By this criterion, regions in the bulk (at distances $>> D$) may still have substantial connections to the boundary. We have, for the first time in any pattern formation system, characterized this boundary connectivity in the specific case of spiral defect chaos. We see clear differences in boundary connectivity as the control parameter is changed. Using homology, we distinguish regions of a pattern as being part of the bulk if they are isolated from the boundary. One

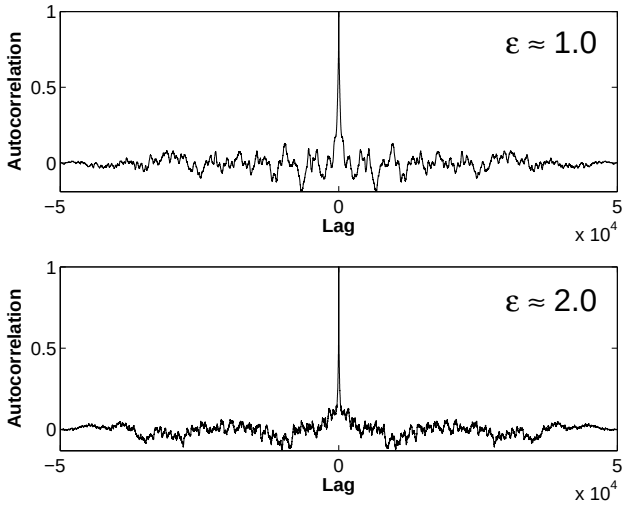

Figure 40: The autocorrelation for the time series of the number of holes (β_1) in a state of SDC. The spiked nature of the function suggests that the fluctuations are primarily stochastic with little correlation. The autocorrelation for β_0 has a similar spiked shape.

notices an asymmetry between the two components in this measure (Figure 41 and Figure 42) with a smaller number of components connected to the boundary as ϵ increases for hot rolls as opposed to being almost the same for cold rolls. This is also reflected in the number of components in the bulk, $\beta_0 - \beta_{bdy,0}$, where the ϵ dependence is primarily seen in the cold rolls.

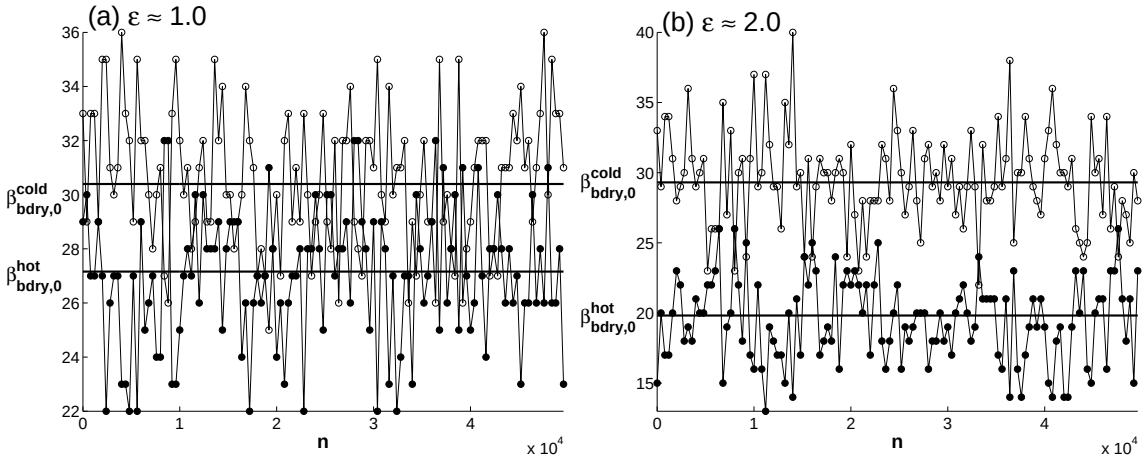

Figure 41: The number of components connected to the boundary for $\epsilon \approx 1.0$ (a) and $\epsilon \approx 2.0$ (b). As in Figure 43 closed circles represent X^{hot} and open circles represent X^{cold}. A sample from every 400th data point from the complete time series is displayed in the above figures.

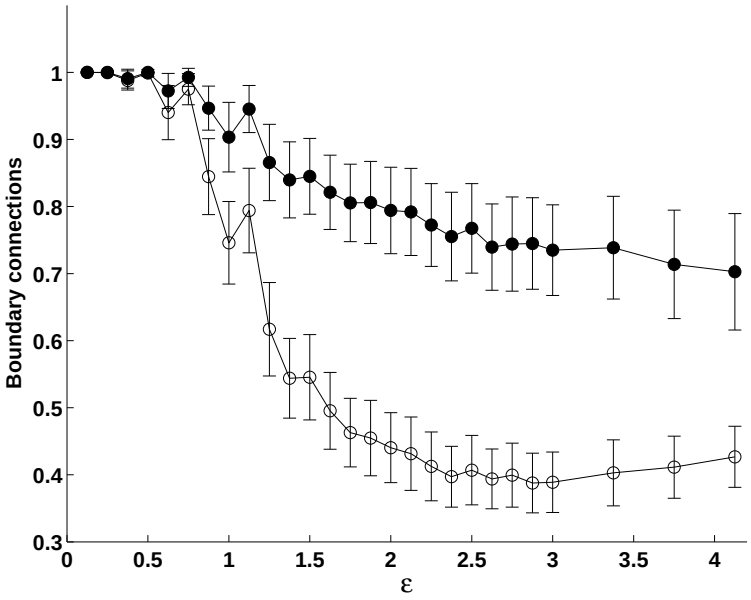

Figure 42: The number of components for hotflow (closed circles) and coldflow (open circles) connected to the boundary, normalized by the total number of such components. The error bars indicate the fluctuation in this number as seen over a long time series.

3.7 Computational Comments

We use the median value of intensity as the threshold just so that the hot and cold regions have the same area (same number of pixels). However the Betti number time series computed at slightly different thresholds (within up to about 10% of the median) present the same qualitative behavior.

Reducing the resolution of the images also does not change the qualitative features of the time series, although it does change the values of the Betti numbers for each image. We tested our computations with a reduction of up to a quarter of the resolution, and got the same qualitative results. Figure 43 and Figure 44 show such a resolution reduction, in which the Betti numbers change slightly.

We tested our entropy computations by repeating the computations using part of the data. By using just 50% of the data we get about 80% of the value of the entropy computed with the whole data. The result is the same if one uses the first half, the last half, or a portion in the middle of the time series.

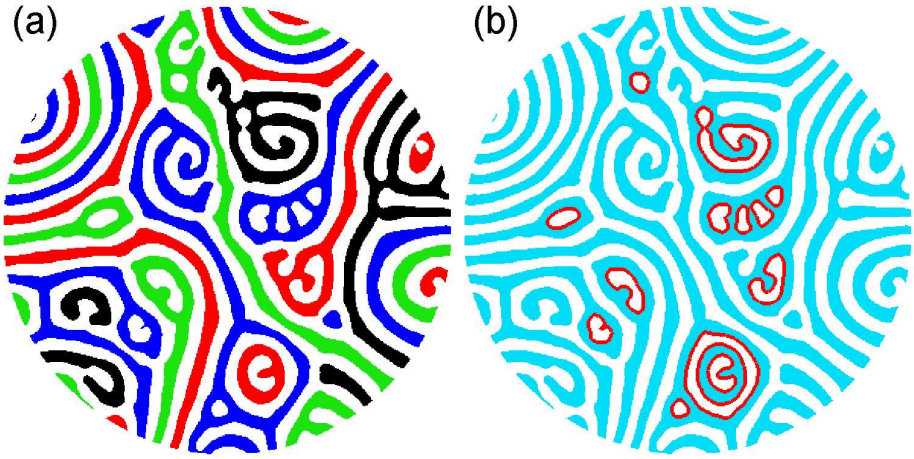

Figure 43: Betti numbers for the X^{hot} region shown in Figure 34 (c). Image (a) shows the $\beta_0^{hot} = 34$ distinct components, with neighboring components distinguished by different colors. Image (b) indicates the boundaries of the $\beta_1^{hot} = 13$ holes.

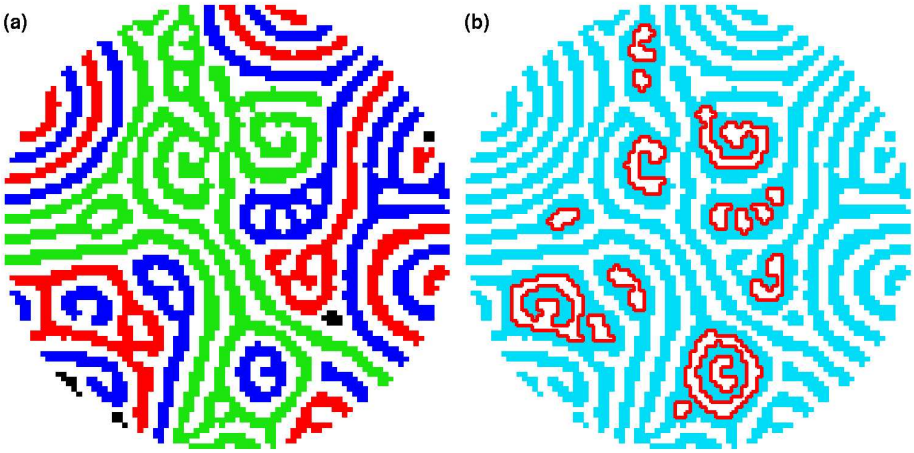

Figure 44: Images corresponding to Figure 43 with resolution reduced to a quarter. Observe that the Betti numbers change a bit for this particular image. Image (a) shows the $\beta_0^{hot} = 28$ distinct components, with neighboring components distinguished by different colors. Image (b) indicates the boundaries of the $\beta_1^{hot} = 17$ holes.

CHAPTER IV

PATTERN COMPLEXITY IN THE CAHN-HILLIARD THEORY OF PHASE SEPARATION

4.1 Introduction

As it was mentioned in Chapter 1, in this chapter we will use homology to extract geometric properties of microstructures generated by the Cahn-Hilliard-Cook model. Several authors have employed topological methods to obtain quantitative connectivity information on microstructures. See for example [1, 12, 28, 31, 32, 48], as well as the references therein. Without using homology, determining the Betti numbers of a complex 3-dimensional structure is far from computationally trivial. In fact, it was pointed out explicitly in [31] that "designing a computer program to directly count the handle density in a complex structure would be extremely difficult [31, p. 3419]." The authors therefore compute the number of handles indirectly, using techniques from digital topology [39]. These techniques relate the number of handles to the Euler characteristic of the structure, which can be computed easily in three space dimensions. Due to these computational issues, the easily computable Euler characteristic takes a predominant role in these studies. Yet, the Euler characteristic, which is the alternating sum of the Betti numbers, provides considerably less topological information than the complete set of Betti numbers. This is true even in the 2-dimensional case considered in this chapter. In Section 4.6 it will be shown that the Euler characteristic is closely related to boundary effects, whereas the Betti numbers also contain information on the bulk structure.

In this chapter, we propose a comparison method based on the geometric properties of the microstructures. The method will be illustrated for the microstructures generated during spinodal decomposition. These structures are fine-grained and snake-like, as shown for example in Figure 45. The microstructures are computed using two different evolution equations which have been proposed as models for spinodal decomposition: The seminal Cahn-Hilliard model, as well as its stochastic extension due to Cook.

The first model for spinodal decomposition in binary alloys is due to Cahn and Hilliard [7, 10]; see also the surveys [9, 29]. Their mean field approach leads to a nonlinear evolution equation for the relative concentration difference $u = \rho_A - \rho_B$, where ρ_A and ρ_B denote the relative concentrations of the two components, i.e., $\rho_A + \rho_B = 1$. The Ginzburg-Landau free energy is given by

$$E_\gamma(u) = \int_\Omega \left(\Psi(u) + \frac{\gamma}{2} |\nabla u|^2 \right) dx, \tag{8}$$

where Ω is a bounded domain, and the positive parameter γ is related to the root mean square effective interaction distance. The bulk free energy, Ψ, is a double well potential, typically

$$\Psi(u) = \frac{1}{4} \left(u^2 - 1 \right)^2. \tag{9}$$

Taking the variational derivative $\delta E_\gamma / \delta u$ of the Ginzburg-Landau free energy (8) with respect to the concentration variable u, we obtain the chemical potential

$$\mu = -\gamma \Delta u + \frac{\partial \Psi}{\partial u}(u),$$

and thus the Cahn-Hilliard equation $\partial u / \partial t = \Delta \mu$, i.e.,

$$\frac{\partial u}{\partial t} = -\Delta \left(\gamma \Delta u - \frac{\partial \Psi}{\partial u}(u) \right), \tag{10}$$

subject to no-flux boundary conditions for both μ and u. Due to these boundary conditions, any mass flux through the boundary is prohibited, and therefore mass is conserved. We generally consider initial conditions for (10) which are small-amplitude random perturbations of a spatially homogeneous state, i.e., $u(0, x) = m + \epsilon(x)$, where ϵ denotes a small-amplitude perturbation with total mass $\int_\Omega \epsilon = 0$. In order to observe spinodal decomposition, the initial mass m has to satisfy $(\partial^2 \Psi / \partial u^2)(m) < 0$.

One drawback of the deterministic partial differential equation (10) is that it completely ignores thermal fluctuations. To remedy this, Cook [14] extended the model by adding a random fluctuation term ξ, i.e., he considered the stochastic Cahn-Hilliard-Cook model

$$\frac{\partial u}{\partial t} = -\Delta \left(\gamma \Delta u - \frac{\partial \Psi}{\partial u}(u) \right) + \sigma \cdot \xi, \tag{11}$$

where

$$\langle \xi(t, x) \rangle = 0, \qquad \langle \xi(t_1, x_1) \xi(t_2, x_2) \rangle = \delta(t_1 - t_2) q(x_1 - x_2).$$

Here $\sigma > 0$ is a measure for the intensity of the fluctuation and q describes the spatial correlation of the noise. In other words, the noise is uncorrelated in time. For the special case $q = \delta$ we obtain space-time white noise, but in general the noise will exhibit spatial correlations. See also [41].

Both the deterministic and the stochastic model produce patterns which are qualitatively similar to the microstructures observed during spinodal decomposition [8]. Recent mathematical results for (10) and (11) have identified the observed microstructures as certain random superpositions of eigenfunctions of the Laplacian, and were able to explain the dynamics of the decomposition process in more detail [5, 44, 45, 61, 62, 72].

Even though both models are based on deep physical insight, they are phenomenological models. Many researchers have therefore studied how well the models agree with experimental observations. See for example [4, 24, 30, 49], as well as the references therein. Most of these studies have been restricted to testing scaling laws. Exceptions include for example Ujihara and Osamura [71], who perform a quantitative evaluation of the kinetics by analyzing the temporal evolution of the scattering intensity of small angle neuron scattering in Fe-Cr alloys. Another approach was pursued by Hyde et al. [31], who consider spinodal decomposition in Fe-Cr alloys. Using experimental data obtained by an atom probe field ion microscopy PoSAP analysis, they study whether the observed microstructures are topologically equivalent to the structures generated by several model equations.

The topological invariant used in [31] is the number of handles in the microstructure occupied by one of the two material phases, which is introduced as a characteristic measure for the topological complexity of percolated structures. Since moving a dislocation through a sponge-like interconnected microstructure generally requires cutting through the handles of the structure, the handle density can be viewed as an analogue of the particle density for systems containing isolated particles. From a theoretical point of view, the number of handles in a microstructure is a special case of the Betti numbers.

Our results are illustrated for the morphologies generated by the deterministic Cahn-Hilliard model (10) and the stochastic model (11). We show that knowledge of the Betti numbers can detect significant differences in the dynamic behavior of these two models. By combining the information provided by different Betti numbers, we are able to quantify boundary effects in finite size systems. In addition, our method can be used to detect fundamental changes in the microstructure topology

due to parameter variation, such as the transition from percolated structures to isolated particles. Many structure-property relationships in materials science are based on fundamental assumptions concerning the underlying microstructure, and our topological analysis can aid in unveiling the underlying topology.

4.2 Numerical Solution of the Stochastic Model

We begin with a brief description of the numerical method used for approximating the Cahn-Hilliard-Cook equation (11). In order to simplify the presentation, we only discuss the case of a 1-dimensional base domain $\Omega = (0, 1)$. The higher-dimensional situation can be treated analogously.

The deterministic part of the evolution equation (11) is approximated using a finite difference scheme with linearly implicit time-stepping. To this end, we choose a time step Δt and a spatial grid size N, and let $\Delta x = 1/N$. For any $k \in \mathbb{N}$ we let $t_k = k \cdot \Delta t$ and approximate the solution $u(t_k, \cdot)$ of (11) by the N-vector $U(t_k) = (U_1(t_k), \dots, U_N(t_k))$, where $U_n(t_k) \approx u(t_k, x_n)$ with $x_n = 1/(2N) + (n-1)/N$ for $n = 1, \dots, N$. The second derivative with respect to x is approximated using standard divided differences, i.e., the values of $u_{xx}(t, \cdot)$ are approximated by $LU(t)$, where L denotes the appropriate tridiagonal matrix. With this notation the numerical method for (11) can be written as

$$\frac{U(t_{k+1}) - U(t_k)}{\Delta t} = -\frac{\epsilon^2}{\Delta x^4} \cdot L^2 U(t_{k+1}) - \frac{1}{\Delta x^2} \cdot L f(U(t_k)) + \sigma \cdot \xi(t_k) \,,$$

which is equivalent to the linear system

$$\left(I + \frac{\epsilon^2 \Delta t}{\Delta x^4} L^2\right) U(t_{k+1}) = U(t_k) - \frac{\Delta t}{\Delta x^2} \cdot L f(U(t_k)) + \sigma \cdot \Delta t \cdot \xi(t_k) \,. \tag{12}$$

The numerical approximation of the noise term will be specified below. This scheme is a variation of linearly implicit schemes, as discussed for example in [26, 60]. In contrast to the methods described in these references, we only split off the bi-Laplacian part of the right-hand side. This ensures the invertibility of the matrix $(I + (\epsilon^2 \Delta t / \Delta x^4) \cdot L^2)$, regardless of the step size Δt. At the same time, we can still choose considerably larger step sizes than in the explicit case. See in particular Quarteroni and Valli [60, Section 12.2.2], where a method analogous to ours is analyzed.

We now turn our attention to the approximation of the noise term. The stochastic forcing term ξ in (11) is given as the generalized derivative of an infinite-dimensional Wiener process $W(t)$, $t \geq 0$,

which can be written as

$$W(t) = \sum_{\ell=1}^{\infty} \alpha_\ell \cdot \beta_\ell(t) \cdot \phi_\ell \ . \tag{13}$$

In this series representation, the stochastic processes β_ℓ denote independent real-valued Brownian motions, and the functions ϕ_ℓ, $\ell \geq 0$, are the eigenfunctions of the Laplacian on Ω subject to homogeneous Neumann boundary conditions. Notice that the sum in (13) excludes the constant eigenfunction ϕ_0. This is necessary to ensure that the stochastic Cahn-Hilliard equation remains mass conserving. The noise process $\xi = \partial_t W$ then satisfies

$$\Delta t \cdot \xi(t_k) \approx W(t_{k+1}) - W(t_k) = \sum_{\ell=1}^{\infty} \alpha_\ell \cdot (\beta_\ell(t_{k+1}) - \beta_\ell(t_k)) \cdot \phi_\ell \ . \tag{14}$$

The definition of Brownian motion implies that the random variable $\beta_\ell(t_{k+1}) - \beta_\ell(t_k)$ is normally distributed with mean 0 and variance $t_{k+1} - t_k = \Delta t$. Therefore, the scaled random variable $(\beta_\ell(t_{k+1}) - \beta_\ell(t_k))/\sqrt{\Delta t}$ is normally distributed with mean 0 and variance 1. As in [65], the series in (14) is approximated by its projection onto the span of the first $N-1$ eigenfunctions $\phi_1, \ldots, \phi_{N-1}$. Altogether, we approximate the noise term ξ by

$$\Delta t \cdot \xi(t_k) \approx \sum_{\ell=1}^{N-1} \alpha_\ell \cdot (\beta_\ell(t_{k+1}) - \beta_\ell(t_k)) \cdot \phi_\ell = \sqrt{\Delta t} \cdot \sum_{\ell=1}^{N-1} \alpha_\ell \cdot B_\ell \cdot \phi_\ell \ , \tag{15}$$

where the B_ℓ denote independent normally distributed random variables with mean 0 and standard deviation 1. Equations (12) and (15) constitute our numerical approximation of the evolution equation (11).

The above numerical scheme can be implemented efficiently using the fast Fourier transform. One can show that the eigenvectors of the tridiagonal matrix L can be obtained by evaluating the above-defined eigenfunctions ϕ_ℓ at each entry of the vector $x = (x_1, \ldots, x_N)$. The time-consuming part in the algorithm is the solution of a linear system of the form $AU = V$ at every timestep, where $A = I + (\epsilon^2 \Delta t / \Delta x^4) \cdot L^2$. Thus, by transforming the vector V into Fourier space using the discrete cosine transform, dividing component-wise by the eigenvalues of A, and then applying the inverse discrete cosine transform, the linear system $AU = V$ can be solved in time $O(N \log N)$. Notice that the noise approximation can easily be added to this scheme, before applying the inverse cosine transform. This is the reason for choosing the upper limit of the sum (15) as $N - 1$, instead of N.

The above description can easily be generalized to the 2-dimensional situation. The simulations in this chapter used an implementation in C in combination with the fast Fourier transform package

FFTW [21]. Moreover, we consider the case of cut-off noise, i.e., in (13) we choose $\alpha_\ell = 1$ for $\ell = 1, \ldots, N-1$, and $\alpha_\ell = 0$ for $\ell \geq N$. This guarantees a spatial correlation function q which closely approximates δ.

4.3 Homology and Betti Numbers

As it was indicated in the introduction we claim that homology provides a useful technique for identifying and distinguishing the evolving microstructures of (10) and (11). While we already described homology theory in Chapter 2, two points need to be discussed: (i) What structures do we want to understand the geometry of, and (ii) what additional information does homology provide when compared to existing methods of microstructure analysis?

Since we are interested in phase separation and $u(t, x)$ represents the relative concentration difference between the two materials at time t and location x, the simplest decomposition of the domain Ω consists of the two sets

$$X^+(t) := \{x \in \Omega \mid u(t, x) > m\} \quad \text{and} \quad X^-(t) := \{x \in \Omega \mid u(t, x) < m\} \ , \tag{16}$$

where m denotes a suitable threshold value, such as the total mass. In this situation, the sets $X^\pm(t)$ represent the regions in the material where one or the other element dominates. Of course, u is the solution of a (stochastic) nonlinear partial differential equation and hence we cannot expect to have an explicit representation of the sets $X^\pm$. For the simulations in this chapter, as indicated in Section 4.2, we use a finite difference scheme to numerically solve (10) and (11) and thus given the domain $\Omega = (0, 1) \times (0, 1)$ with a spatial grid size $N \times N$ we obtain values $U(t_k, x^1_\ell, x^2_n)$, where $x_j = 1/(2N) + (j-1)/N$. We give a geometric interpretation to this numerical grid via the squares $Q_{\ell,n} := [(\ell-1)/N, \ell/N] \times [(n-1)/N, n/N]$. In particular, we define a cubical approximation to $X^\pm(t)$ by

$$U^+(t_k) := \left\{Q_{\ell,n} \mid U(t_k, x^1_\ell, x^2_n) > m\right\} \quad \text{and} \quad U^+(t_k) := \left\{Q_{\ell,n} \mid U(t_k, x^1_\ell, x^2_n) < m\right\}$$

Figure 45 indicates sets $U^\pm(t_k)$ at various times steps for a particular solution to (10) and (11). It is easy to observe that patterns produced by $U^\pm(t_k)$ are complicated, time dependent, and appear at intermediate time steps to differ qualitatively for the deterministic and stochastic models. Before

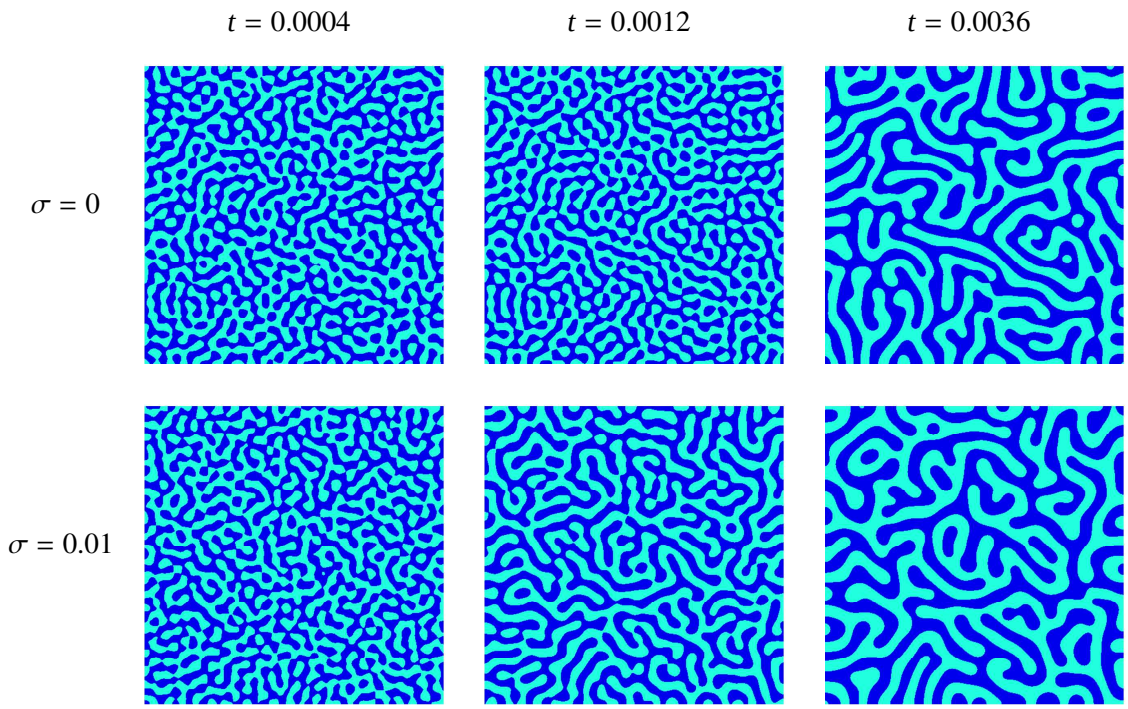

Figure 45: Microstructures obtained from the Cahn-Hilliard-Cook model (11). The top row shows solution snapshots for the deterministic case $\sigma = 0$, the bottom row is for noise intensity $\sigma = 0.01$. In both cases we used $\gamma^{1/2} = 0.005$ and $m = 0$. The set $X^+(t)$ defined in (16) is shown in dark blue.

moving on to describe how homology can be used to quantify these observations, notice that if the computations had been performed in a 3-dimensional domain, then the same approach could be used except that the 2-dimensional squares $Q_{\ell,n}$ would be replaced by 3-dimensional cubes.

4.4 Effects of Noise on the Pattern Morphology

In this section we use computational homology to study the effects of the stochastic forcing term in (11) on the temporal evolution of the pattern complexity. We consider the case of total mass $m = 0$ and Ψ as in (9), and to begin with restrict ourselves to $\gamma^{1/2} = 0.005$. The simulations are performed on the unit square $\Omega = (0, 1) \times (0, 1)$.

For varying values of the noise intensity σ, we numerically integrate the Cahn-Hilliard-Cook equation (11) starting from a random perturbation of the homogeneous state $m = 0$ with amplitude 0.0001 up to time

$$t_{end} = \frac{160\gamma}{\Psi''(m)^2}\,, \qquad \text{where} \qquad \Psi''(m) = 3m^2 - 1\,, \tag{17}$$

which in our situation reduces to $t_{end} = 0.004$. This time frame covers the complete spinodal

decomposition phase, as well as early coarsening. The domain is discretized by a 512×512-grid and the time interval $[0, t_{end}]$ is covered by $10,000$ integration steps. Every 50 time steps, the sets $X^{\pm}(t)$ introduced in the last section are determined, and finally their Betti numbers are computed using [35]. On a 2 GHz Dual Xeon Linux PC it took about 15 minutes to create the 402 sets $X^{\pm}(t)$ for $t/t_{end} = 0, 0.005, 0.010, \ldots, 0.995, 1$, as well as a total of 46 minutes to compute their Betti Numbers.

Figure 46 contains the results of these computations for two different values of the noise intensity. The solid red curves show the Betti number evolution for the deterministic case $\sigma = 0$, the dashed blue curves are for noise intensity $\sigma = 0.01$; the solution snapshots in Figure 45 are taken from these two simulations. At first glance, the graphs in Figure 46 are not surprising. For the initial time $t = 0$ both β_0 and β_1 are large, since the initial perturbation was chosen randomly on the computational grid. In fact, the actual values lie well outside the displayed range. The smoothing effect of (11) leads to a rapid decrease of the Betti numbers for times t close to 0, and coarsening behavior in the Cahn-Hilliard-Cook model is responsible for the decrease observed towards the end of the time window. All shown evolutions exhibit small-scale fluctuations, which are most likely artifacts caused by the cubical approximation of the sets $X^{\pm}(t)$. Even though these fluctuations are not necessarily desirable, they are a more or less automatic consequence of the numerical approximation of the partial differential equation (11).

Despite these similarities, there are some obvious differences between the deterministic and the stochastic evolution. In the deterministic situation, the initial complexity decay occurs sooner than in the stochastic case. In addition, it appears that the Betti numbers of $X^{+}(t)$ for $\sigma = 0.01$ decay more or less monotonically, provided we ignore the above-mentioned small-scale fluctuations. In contrast, in the deterministic case the initial decrease seems to be followed by a period of stagnation or even growth of the Betti numbers, see for example β_0 for $X^{+}(t)$ or β_1 for $X^{-}(t)$.

The observations made in the last paragraph could indicate fundamental differences between the deterministic and the stochastic Cahn-Hilliard model. However, these observations are based on a single randomly chosen initial condition, and it is therefore far from clear whether they represent behavior typical for either of the models. For this we have to observe ensembles of solutions for each of the models and study the statistics of their complexity evolutions. For the purposes of this chapter,

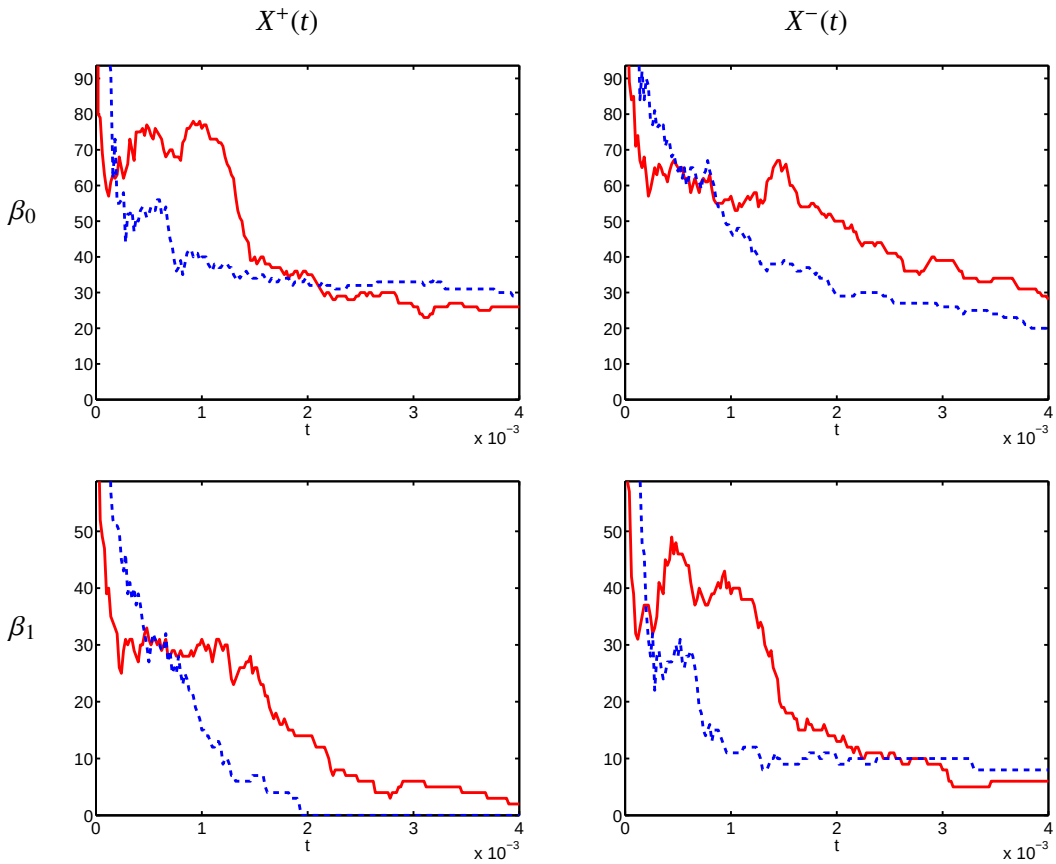

Figure 46: Evolution of the Betti numbers for the solutions of Figure 45. In each diagram, the solid red curve corresponds to $\sigma = 0$, the dashed blue curve is for $\sigma = 0.01$. In both cases we used $\gamma^{1/2} = 0.005$ and $m = 0$. The diagrams in the left column show the results for $X^+(t)$, the right column is for $X^-(t)$. The top row contains the evolutions of β_0, the bottom row shows β_1.

we concentrate on the averaged complexity evolution. Figure 47 shows the averaged Betti number evolution for six values of the noise intensity σ ranging from 0 to 0.1, in each case based on solution ensembles of size 100. The qualitative form of the complexity evolution curves differs substantially. For large noise the complexity decays monotonically, while it shows a surprising increase in the deterministic situation. The change between the two behaviors occurs gradually, and there seems to be a specific threshold σ_{cr} for the noise intensity beyond which monotone decay is observed. Notice also that despite the small ensemble size, the evolution curves of $X^+(t)$ and $X^-(t)$ are in good agreement, which for our choice of $m = 0$ and Ψ as in (9) has to be expected. In this sense, the ensemble behavior is a reflection of typical solution dynamics, reinforcing our above observations. An interesting mathematical question would be to determine the ensemble size necessary to obtain

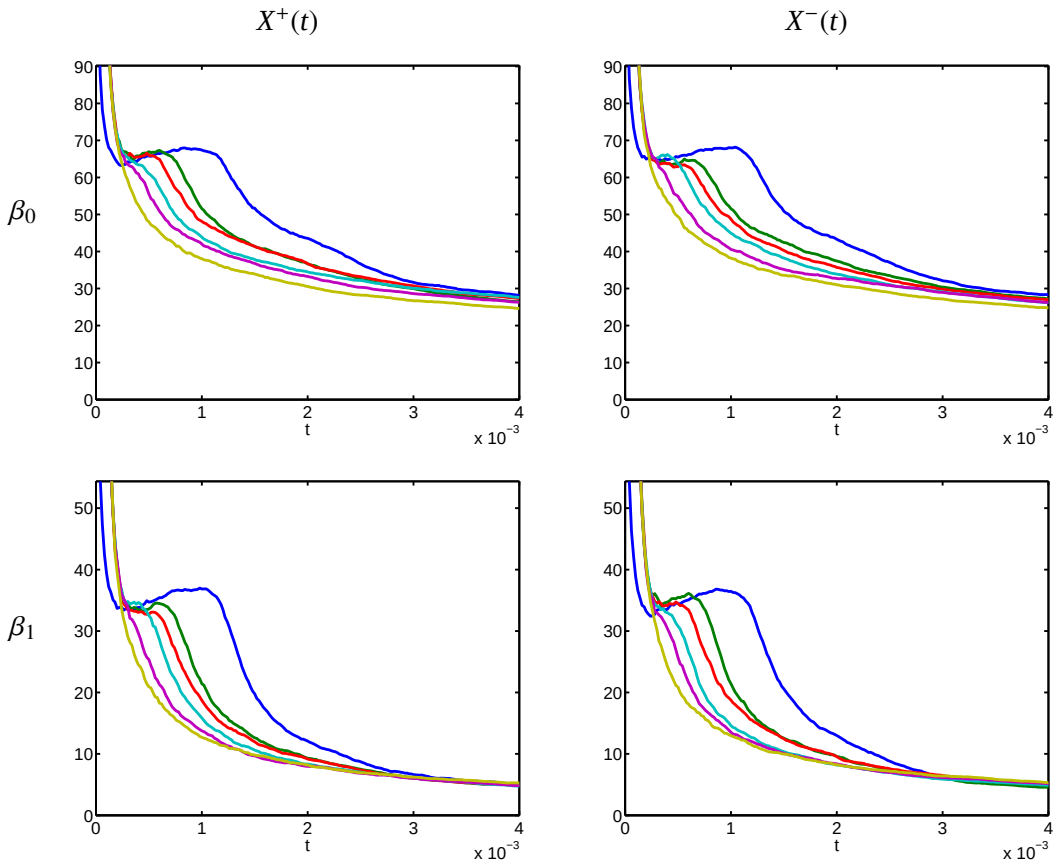

Figure 47: Evolution of Betti number averages for a sample size of 100, with $\gamma^{1/2} = 0.005$ and $m = 0$. In the top row at dimension level 60 the curves correspond to the values $\sigma = 0.1$, 0.03, 0.01, 0.003, 0.001, and 0, from left to right; analogously in the bottom row at level 25.

the symmetry of curves for $X^+(t)$ and $X^-(t)$ observed in Figure 47.

The simulations discussed so far consider the specific value $\gamma^{1/2} = 0.005$. We performed analogous simulations for various values of γ, for various grid sizes, and a variety of time steps. In each case, the time window extended from 0 to t_{end} as defined in (17). These results show that the behavior shown in Figure 47 is typical. In all cases, the time window covers the complete spinodal decomposition phase, as well as early coarsening; the resulting evolution curves for the deterministic case show the characteristic non-monotone behavior; for sufficiently large noise intensity we observe monotone decay. The only parameters changing with γ appear to be the absolute height of the evolution curves and (possibly) the critical noise intensity σ_{cr}. While these scalings will be addressed in more detail in Section 4.6, we close this section with a brief discussion of the dependence of σ_{cr} on γ.

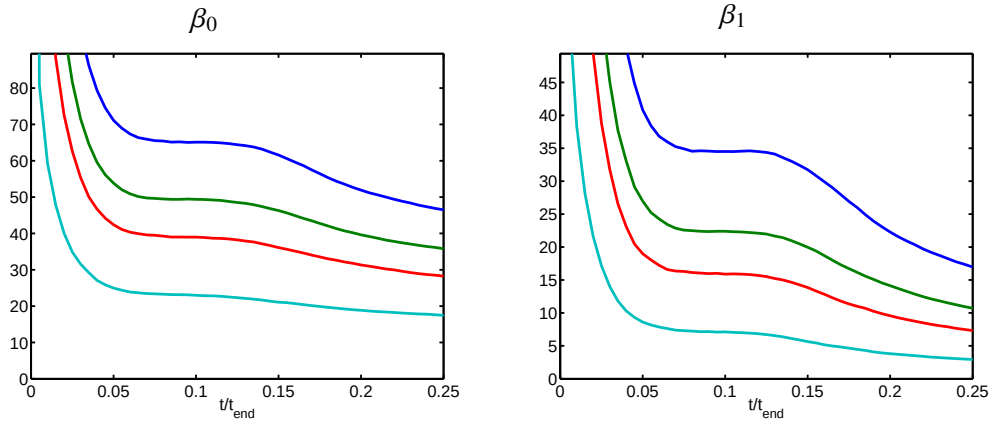

Figure 48: Betti number averages for $X^+(t)$ with varying $\gamma^{1/2} = \sigma$ and $m = 0$. From top to bottom the curves correspond to $\gamma^{1/2} = \sigma = 0.005$, 0.006, 0.007, and 0.01, respectively. The sample size for each of these simulations is $1,000$.

To get a more accurate picture of the monotonicity properties of the evolution curves we compute the averaged Betti number evolution from larger solution ensembles and for times up to only $t_{end}/4$. As before, t_{end} is given by (17), and we consider the case $m = 0$. The noise intensity σ is chosen equal to $\gamma^{1/2}$, and the ensemble size is taken as $1,000$. The results of these simulations for $\gamma^{1/2} = 0.005$, 0.006, 0.007, and 0.01 are shown in Figure 48. Notice that each of these curves exhibits monotone decay of the Betti numbers with a pronounced plateau, so one would expect that these curves are for values $\sigma \approx \sigma_{cr}$. Yet, it appears that the length of the plateau decreases with increasing γ. This latter observation could indicate that for the larger γ-values the noise intensities used in Figure 48 are too large. In fact, our scaling analysis in Section 4.6 will show that this is the case.

The results of this section demonstrate that Betti numbers can be used to quantitatively distinguish between microstructure morphologies generated by different models. Ultimately we hope that this quantitative information can be used to match models to actual experimental data. In fact, the limited experimental data in [31] seems to indicate that the handle density of the microstructures generated through spinodal decomposition decreases monotonically. Thus, these experimental results favor the stochastic Cahn-Hilliard-Cook model with sufficiently large noise intensity.

4.5 Morphology Changes due to Mass Variation

So far we restricted our study to the case of equal mass, i.e., we assumed $m = 0$. Yet, spinodal decomposition can be observed as long as $\Psi''(m) < 0$, which for our choice of Ψ is equivalent to $|m| < 3^{-1/2} \approx 0.577$. Total mass values outside this range lead to nucleation and growth behavior which produces microstructures consisting of isolated droplets — in contrast to the microstructures shown in Figure 45. In this section we use computational homology to quantify the pattern morphology changes during spinodal decomposition in the deterministic Cahn-Hilliard model (10) as the total mass is increased from $m = 0$ towards $m \approx 3^{-1/2}$.

Before presenting our numerical results, we have to address one technical issue. Even though the homogeneous state m is unstable as long as $\Psi''(m) < 0$, the strength of the instability changes with m. One can easily show that the growth rate of the most unstable perturbation of the homogeneous state is close to $\Psi''(m)^2/(4\gamma)$ [44]. Thus, as the total mass approaches the boundary of the spinodal region, the time frame for spinodal decomposition grows. In order to compare the pattern morphology for different values of the total mass we therefore scale the considered time window. As in the last section, we compute the solutions up to time t_{end} defined in (17), whose scaling is motivated by largest growth rate mentioned above.

How do changes in the total mass m affect the microstructures generated through spinodal decomposition? Figure 49 contains typical patterns for $m = 0, 0.1, \ldots, 0.5$. In each case, the pattern was generated by solving (10) up to time $t = 0.4 \cdot t_{end}$, with t_{end} as in (17). Notice that even though all of these microstructures are a consequence of phase separation through spinodal decomposition, the last two microstructures resemble the ones generated by nucleation and growth. In other words, Figure 49 indicates a gradual change from the highly interconnected structures observed in the equal mass case to the disconnected structures observed in nucleation.

In order to further quantify this gradual change, we use computational homology as in the last section. For $\gamma^{1/2} = 0.005$ and various values of m between 0 and 0.55 we computed the averaged Betti number evolution of the sets $X^{\pm}(t)$ in (16) from $t = 0$ up to time $t = t_{end}$. The resulting 2-dimensional surfaces are shown in Figure 50. To avoid the large Betti numbers close to the random initial state, these graphs do not include the times $t = 0$ and $t = 0.005 \cdot t_{end}$. Of particular interest

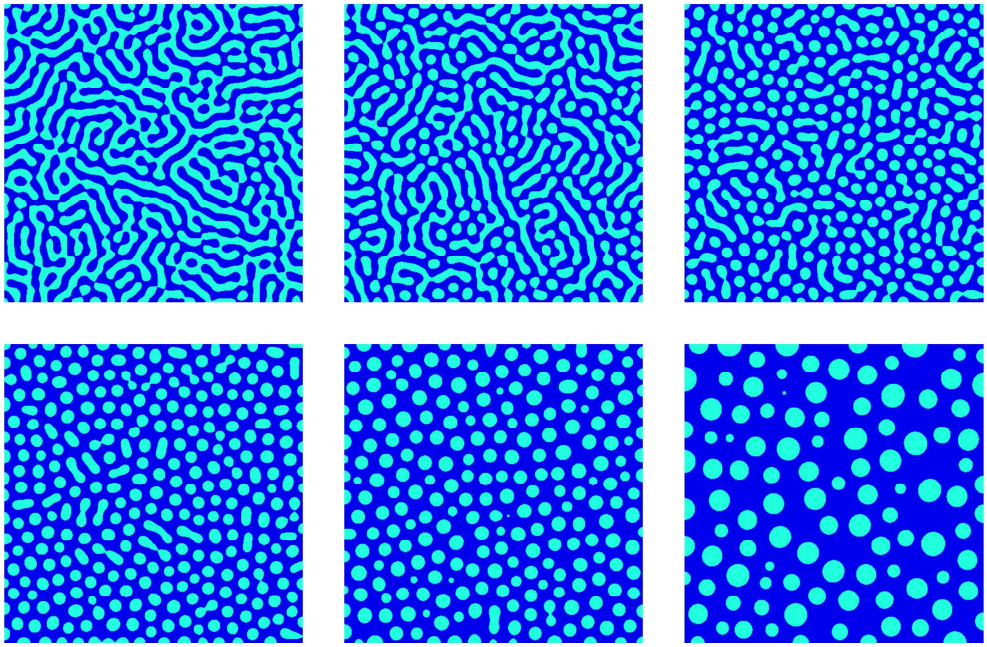

Figure 49: Microstructures obtained from the Cahn-Hilliard model (10) for $\gamma^{1/2} = 0.005$ for varying m. From top left to bottom right solution snapshots are shown for total mass $m = 0, 0.1, \ldots, 0.5$ at time $t = 0.4 \cdot t_{end}$, i.e., shortly after completion of the spinodal decomposition phase. The set $X^+(t)$ is shown in dark blue.

is the topology of the sets $X^+(t)$ which correspond to the dominant phase. The graphs in the left column of Figure 50 show that in terms of the quantitative topological information given by the averaged Betti numbers, one observes a gradual and continuous change from the interconnected microstructures for $m = 0$ to the nucleation morphology. In addition, the graph of β_0 for $X^+(t)$ indicates that for $t/t_{end} > 0.25$, i.e., after the completion of spinodal decomposition, and for $m > 0.2$ the dominant phase forms a connected structure; that is, the complementary phase breaks up completely. Yet, the typical droplet structure reminiscent of nucleation and growth behavior can only be observed for values of the total mass larger than 0.3. In the surfaces of Figure 50 this is reflected by the fact that for fixed time t, the Betti number β_1 of the dominant phase $X^+(t)$ continues to increase with m until $m \approx 0.3$. As the total mass approaches $3^{-1/2}$, the first Betti number then decreases again, corresponding to an increasing droplet size.

In addition to the results shown in Figure 50, we performed analogous simulations for $\gamma^{1/2} = 0.0025$, 0.0075, and 0.0100. In each case, the qualitative shape of the computed surfaces matched the one for $\gamma^{1/2} = 0.005$, only the absolute height of the surfaces changed. In fact, our computations

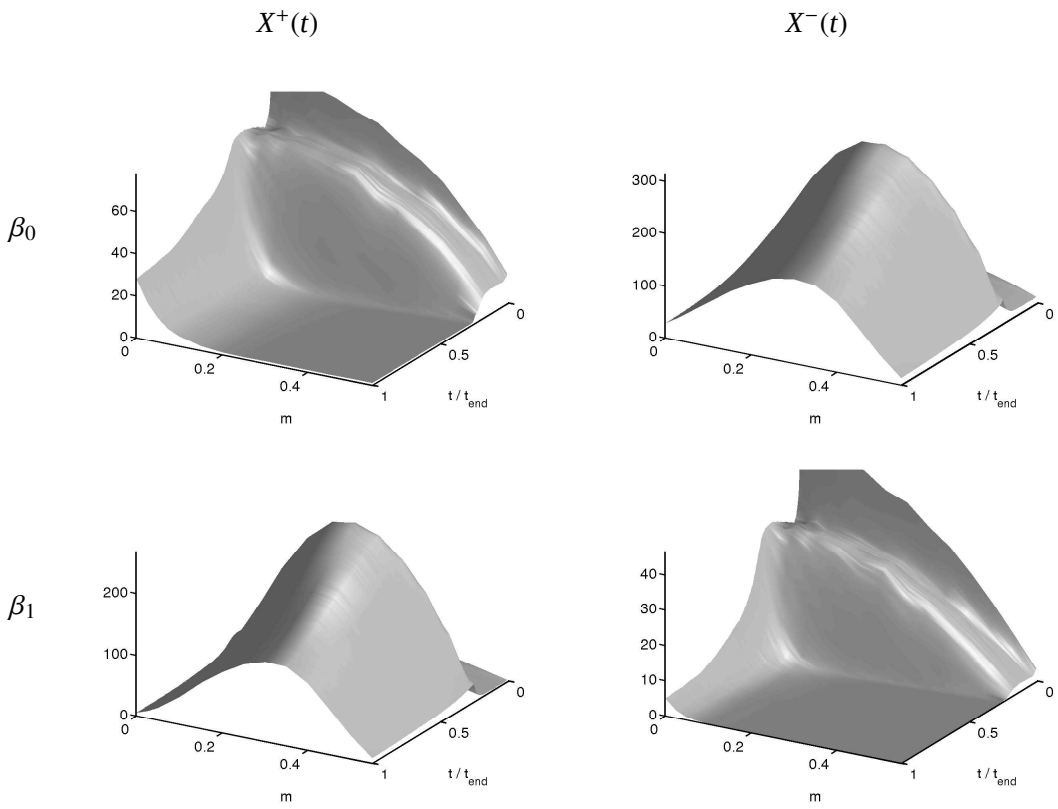

Figure 50: Evolution of Betti number averages for a sample size of 100, with $\gamma^{1/2} = 0.005$ and varying mass m. The left column corresponds to $X^+(t)$, the right one to $X^-(t)$; the top row contains the graphs for the 0-th Betti number, the bottom row for the first.

indicate that the units on the vertical axes of Figure 50 scale proportionally to γ^{-1} for these values of γ.

The computations of this section indicate how homology can be used to quantify global morphological changes, such as connectivity, due to mass variation. On a more general level, given a model of a particular material it would be interesting to seek correlations between macroscopic properties and the type of geometric information expressed in Figure 50. Such studies would be in the spirit of structure-property relationships which have been obtained for certain types of microstructures, such as for systems of isolated particles using particle distributions, or for interconnected structures [43, 42] using the notion of matricity. Comparisons of this nature would probably be of even greater importance in the case of 3-dimensional simulations, since visualization of these phenomena would be extremely complicated.

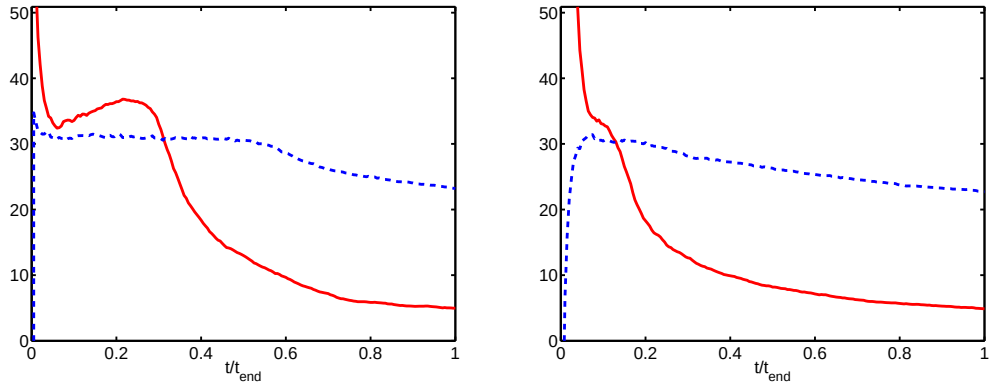

Figure 51: Averaged temporal evolution of the number $\beta_{\text{int},0}$ of internal components of the set $X^+(t)$, and of the number $\beta_{\text{bdy},0}$ of components of $X^+(t)$ touching the boundary of the base domain Ω. In each diagram, the solid red curve corresponds to $\beta_{\text{int},0}$, the dashed blue curve is for $\beta_{\text{bdy},0}$. The left diagram is for the deterministic case $\sigma = 0$, the right one for the stochastic case with noise intensity $\sigma = 0.01$. In both cases we used $\gamma^{1/2} = 0.005$ and $m = 0$.

4.6 Boundary Effects and Scalings

While our study so far concentrated on the Betti numbers β_0 and β_1, significant additional information can be obtained by combining the topological information for $X^+(t)$ with the information for the complementary sets $X^-(t)$. As it was discussed in Chapter 2 these information can be combined to obtain the number of components touching the boundary and the number of internal component of each of the structures. Let us denote the number of internal components of $X^+(t)$ by $\beta_{\text{int},0}(X^+(t))$ and the number of components touching the boundary of Ω by $\beta_{\text{bdy},0}(X^+(t))$. Similarly for $X^-(t)$.

For $\gamma^{1/2} = 0.005$ and $m = \sigma = 0$ the averaged temporal evolution of these quantities is shown in the left diagram of Figure 51, for a sample size of 100. While the number of internal components shows the typical non-monotone behavior described in the last sections, the number of boundary components remains basically constant, well into the coarsening regime. Notice also that due to $m = 0$ and our choice of Ψ, the ensemble averages of $\beta_1(X^+(t))$ and $\beta_1(X^-(t))$ have to be equal. Thus, the number $\beta_{\text{bdy},0}(X^+(t))$ of boundary components equals in fact the Euler characteristic of the set $X^+(t)$. Similarly, the right diagram of Figure 51 shows the evolutions of $\beta_{\text{int},0}$ and $\beta_{\text{bdy},0}$ for the corresponding stochastic case with $\sigma = 0.01$. While the number of internal components exhibits the monotone decay described in Section 4.4, the number of boundary components reaches the same level as in the deterministic situation, but starts its decay earlier.

In view of Figure 51, one can rightfully question the conclusions obtained so far. During the spinodal decomposition regime, $\beta_{\text{int},0}$ and $\beta_{\text{bdy},0}$ are comparable, further into the coarsening regime the number of boundary components clearly dominates. In order to validate our results of the last two sections, it is therefore necessary to consider various system sizes. If instead of the unit square we consider the domain $\Omega = (0, \ell) \times (0, \ell)$, then a combination of the spatial rescaling $x \mapsto x/\ell$ and the temporal rescaling $t \mapsto t\ell^2$ transforms both (10) and (11) into equations on the unit square, but with new interaction parameter γ/ℓ^2. In the stochastic case (11), the rescaling leaves the noise intensity σ unchanged. In other words, we can consider larger system sizes by considering smaller values of γ.

The results of such a system size scaling analysis are shown in Figure 52, where we consider both the deterministic case $\sigma = 0$ and the stochastic case with $\sigma = 0.01$ for $m = 0$ and a variety of γ-values. The resulting evolution curves for $\beta_{\text{int},0}$ have been multiplied by γ/γ_*, with $\gamma_*^{1/2} = 0.0015$, which is the smallest considered value of the interaction parameter. Thus, the left column of Figure 52 indicates a scaling of $\beta_{\text{int},0}$ proportional to γ^{-1}, i.e., proportional to the area of the underlying domain. For the number of boundary components shown in the right column of Figure 52, we used the scaling factor $(\gamma/\gamma_*)^{1/2}$. The diagram therefore indicates that $\beta_{\text{bdy},0}$ scales proportional to $\gamma^{-1/2}$, i.e., proportional to the length of the boundary of the domain. Due to the specific form of the involved scaling factors, the absolute numbers given on the vertical axes in Figure 52 are the correct component numbers for $\gamma^{1/2} = 0.0015$. In this situation, the number of internal components clearly dominates the number of boundary components throughout spinodal decomposition and early coarsening. Notice also that the results for the stochastic case indicate that the critical noise intensity σ_{cr} discussed at the end of Section 4.4 appears to be independent of the system size. This explains the findings of Figure 48.

While the scaling in the left column of Figure 52 shows more deviation than the one in the right column, these deviations are a consequence of the small system sizes for large values of γ. Yet, we find it remarkable that the non-monotone evolution of $\beta_{\text{int},0}$ can be observed even for $\gamma^{1/2} = 0.01$, despite the fact that in this case we have $\beta_{\text{int},0} \approx 0.5\beta_{\text{bdy},0}$ during spinodal decomposition and early coarsening, and that the amplification factor used to scale the interior component curve is $0.01^2/\gamma_* = 44.4$. We believe that the accuracy of the above scalings over the considered γ-range

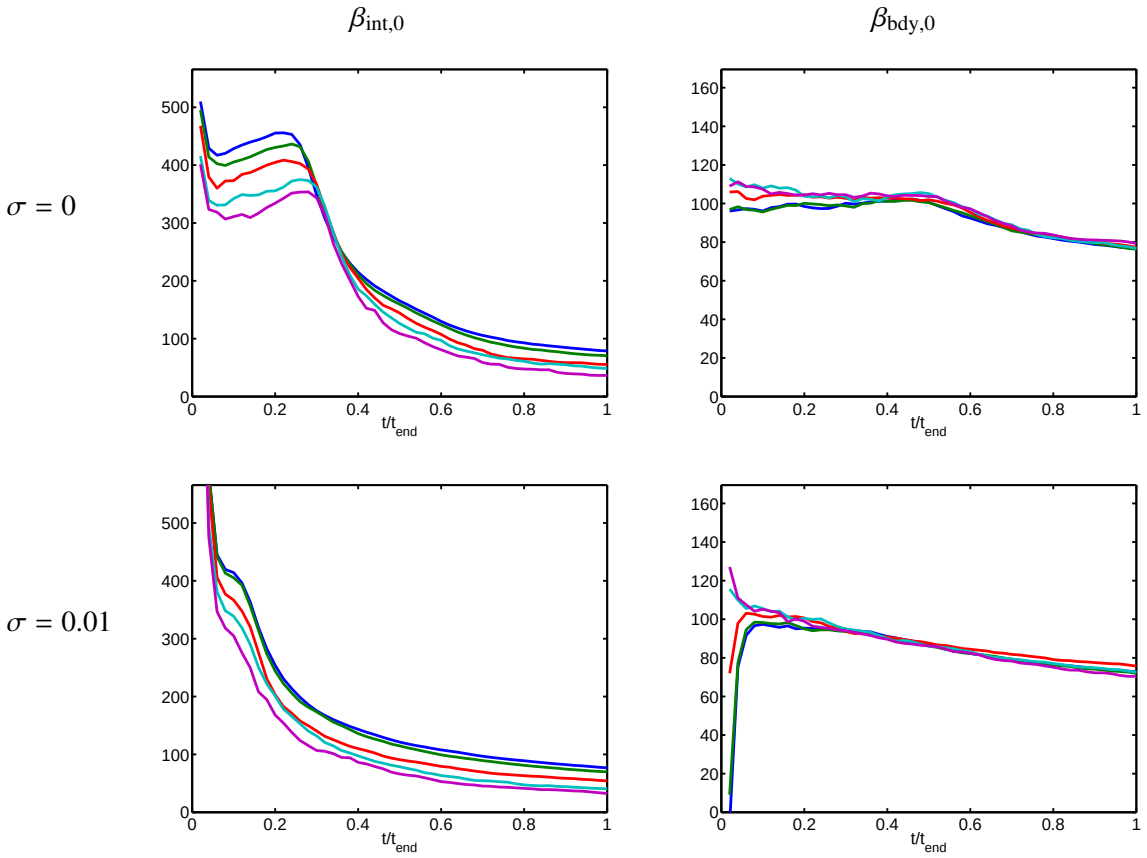

Figure 52: Evolution of internal and boundary component averages of $X^+(t)$ for varying γ and a sample size of 100, with $m = 0$. The top row shows the case $\sigma = 0$, the bottom row is for $\sigma = 0.01$. The left column is for the number of internal components and shows the evolutions of the scaled quantity $\beta_{\text{int},0} \cdot \gamma/\gamma_*$, with $\gamma_*^{1/2} = 0.0015$; from top to bottom in each of the diagrams the curves are for $\gamma^{1/2} = 0.0015, 0.0025, 0.005, 0.0075, 0.01$. The right column is for the number of components touching the boundary and shows the evolutions of the scaled quantity $\beta_{\text{bdy},0} \cdot (\gamma/\gamma_*)^{1/2}$, for the same values of $\gamma^{1/2}$.

indicates their validity also for smaller values of γ.

The results of this section demonstrate that the information provided by the collection of Betti numbers for $X^{\pm}(t)$ can be used to derive detailed quantitative statements about the relative sizes of boundary effects in finite size systems, when compared to internal (or bulk) effects. This is in sharp contrast to what can be extracted from other (easier computable) topological invariants, such as the Euler characteristic. In the above situation, the Euler characteristic only describes the number of boundary components, but can provide no insight into the number of internal components.

4.7 Conclusions and Future Directions

In this chapter we proposed the use of computational homology as an effective tool for quantifying and distinguishing complicated microstructures. Rather than discussing experimental data, we considered numerical simulations of the deterministic Cahn-Hilliard model, as well as its stochastic extension due to Cook. The obtained topological characterizations were used to (a) uncover significant differences in the temporal evolution of the pattern complexity during spinodal decomposition between the deterministic and the stochastic model, as well as to (b) establish the existence of a gradual transition of the spinodal decomposition microstructure morphology as the total mass approaches the boundary of the spinodal region. Furthermore, by combining different topological information, we managed to (c) obtain detailed information on boundary effects for various system sizes. In order to simplify our presentation, the results were presented in a 2-dimensional setting. Nevertheless, the computational tools are available for and effective in arbitrary dimensions.

We believe that the presented methods can serve as practical tools for assessing the quality of continuum models for phase separation processes in materials. This is achieved by providing quantitative topological information which can readily uncover differences in models as in (a). In addition, this quantitative information can be used to compare the computed microstructure topology to experimental observations. For example, the study in [31] determined the handle density of spinodally decomposing iron-chromium alloys. This quantity corresponds to the first Betti number, and the results of [31] indicate a monotone decay — which in combination with (a) favors the stochastic Cahn-Hilliard-Cook model over the deterministic one. Finally, combining topological information as in (c) makes it possible to quantify boundary effects, which are present in any finite size system.

A second possible application is the identification of model parameters based on the microstructure topology. For example, our considerations in (b) resulted in characteristic evolution curves as a function of the parameter m, as well as in scaling information with respect to γ. Combined, these graphs could be used to determine specific values of these parameters for certain experimental situations.

CHAPTER V

EXCITABLE MEDIA AND SPIRAL WAVES

5.1 Introduction

It is well established both numerically and experimentally that nonlinear systems involving diffusion, chemotaxis, and/or convection mechanisms can generate complicated time-dependent patterns. Specific examples include the Belousov-Zhabotinskii reaction [38, 68, 74, 76, 53], the Gray-Scott model [56, 55], the oxidation of carbon monoxide on platinum surfaces [78], slime mold [69], the cardiac muscle [75, 77, 40, 59] and excitable media [37, 79, 70]. Because this phenomenon is global in nature, obtaining a quantitative mathematical characterization that to some extent records or preserves the geometric structures of the complex patterns is difficult. In this chapter we will use homology to measure Lyapunov exponents that imply the existence of spatial-temporal chaos. We will also suggest a tentative step towards the classification and/or identification of patterns within a particular system.

We first consider the 1-dimensional Gray-Scott model to develop the geometric intuition behind our approach, then we analyze the FitzHugh-Nagumo system in a 2-dimensional domain.

5.2 The Gray-Scott Model

Consider the 1-dimensional Gray-Scott model

$$\begin{aligned} u_t &= d_1 u_{xx} - uv^2 + F(1-u) \\ v_t &= d_2 v_{xx} + uv^2 - (F+k)v \end{aligned} \tag{18}$$

with Neumann boundary conditions on the interval $\Omega = [0, 1.6]$. For this system we restrict our computations to a single set of parameter values: $d_1 = 2 \times 10^{-5}$, $d_2 = 10^{-5}$, $F = 0.035$, and $k = 0.05632$ at which complicated spatio-temporal dynamics has been reported [56, 55].

As it was mentioned in Chapter 1 we observe the dynamics of the patterns generated by (18) by thresholding the data, coloring the excited regions, and creating movies. Since each frame of the

movie is 1-dimensional, the dynamics can be better viewed as a plot in the 2-dimensional space-time domain. Figure 53 shows an example of a 2-dimensional pattern generated by (18).

5.2.1 Excited Space-Time Geometry

As indicated above, our goal is to understand and quantify the spatial and temporal geometry of patterns. For this purpose it is useful to think of the excited media as a subset of $\Omega \times [0, \tau]$, where the last direction represents time and τ is the length of the movie. If, as is the case in (18), Ω is 1-dimensional, then each colored pixel of Figure 53 can be viewed as a 2-dimensional cube. Thus the excited media is represented by a set E in $\mathbb{R}^2$ consisting of a finite union of cubes. Let $V_{i,k}$ denote the cube corresponding to the pixel x_i for the kth frame of the movie, then $E = \{V_{i,k} \mid v(x_i, t_k) \geq 0.23\}$. Observe that, viewed as a finite collection of cubes, E provides a combinatorial representation of the excited media. At the same time E is a subset of $\Omega \times [0, \tau]$ that approximates the geometry of the excited media in both space and time.

As it was mentioned in Chapter 1, we are trying to quantify both the spatial structures of the patterns and how they change with time. Conceptually, the simplest way to do this is to compute the topology of each frame of the movie and then measure the change. Unfortunately, this approach cannot measure the global interactions between the fronts of the patterns that occur at different points in time. The other extreme is to consider the topology of E itself. However, if the dynamics of the original system is chaotic, then it is recurrent, and hence for large τ much of the structure should be redundant.

For these reasons we introduce the notion of a *time block* $T_{n,b} := \{V_{i,k} \in E \mid n \leq k \leq n + b\}$. Figure 53 shows the time block $T_{1500,2000}$ for (18). Observe that $T_{n,0}$ represents the nth frame of the movie. For fixed b, $T_{n,b}$ captures the geometry of the pattern interactions over a given time range. We can see how this evolves by studying a sequence of time blocks of the form $\{T_{a(m-1),b} \mid m = 1, 2, \ldots, M\}$. Figure 53 shows the time block $T_{1500,2000}$, where the holes are highlighted. Notice that there is a simple relation between the holes in such patterns and the dynamics of (18). Consider the leftmost hole in Figure 53 for example; it arises from the division of one hump into two humps which separate for some amount of time and then coalesce together at a later point in time.

To compute the Betti numbers, for each $V_{i,k} \in E$, we define $Q_{i,k} := [i, i + 1] \times [k, k + 1]$. Let

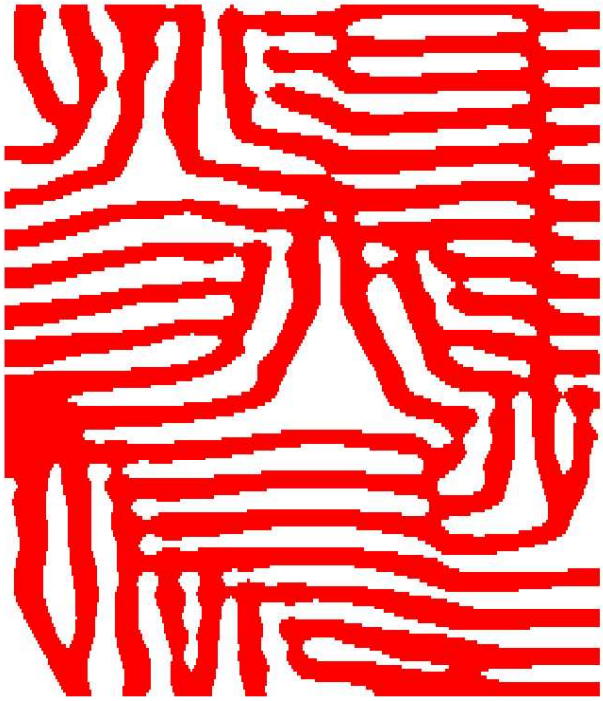

Figure 53: Time block $T_{1500,2000}$ for (18). The colored region indicates the evolution of the pattern of the excited media defined by $v \geq 0.23$.

$\mathbb{T}_{n,b} := \{Q_{i,k} \mid V_{i,k} \in T_{n,b}\}$. Then $H_i(\mathbb{T}_{n,b}) \cong H_i(T_{n,b})$. Because $\mathbb{T}_{n,b}$ is the union of unit cubes defined in terms of an integer lattice, it is a *cubical set*. Therefore we can use the algorithms discussed in Chapter 2 to compute their homology.

5.2.2 Topological Results

We will use the existence of a positive Lyapunov exponent to conclude the existence of spatial-temporal chaos. This Lyapunov exponent will be measured by means of a time series of Betti numbers.

To produce a time series that incorporates the spatial structure, we computed the Betti numbers of various $\mathbb{T}_{n,b}$. More precisely, we computed $\{H_*(\mathbb{T}_{300(m-1),10000}) \mid m = 1, 2, \ldots, 12000\}$ and hence obtained the Betti numbers $\beta_i(m)$ for $H_i(\mathbb{T}_{300(m-1),10000})$.

Our first observation was that $\beta_0(m)$ is piecewise constant taking on a limited number of fairly small values. However, the time series $B_{(300,10000)} := \{\beta_1(m) \mid m = 1, 2, \ldots, 12000\}$ proved to be quite interesting. A plot of the first 2000 points of this time series is shown in the Figure 54.

We make use of the following algorithm (see [36, 27]) to compute the maximal Lyapunov exponent from time series. Consider a time series $\{s_n \in \mathbb{R} \mid n = 0, \ldots, N\}$ obtained from some nonlinear dynamical system. Let

$$S(k) = \frac{1}{N} \sum_{n_0=1}^{N} \ln\Big[\frac{1}{|B_{n_0}|} \sum_{y_n \in B_{n_0}} |y_{n_0+k} - y_{n+k}|\Big] \tag{19}$$

where $y_n = (s_n, s_{n+1}, \ldots, s_{n+d-1})$ is a vector in the d-dimensional reconstructed space, and B_{n_0} is a η-neighborhood of y_{n_0}. If $S(k)$ exhibits a linear increase with identical slope for k greater than a given k_0 and for a reasonable range of η, then this slope can be taken to be an estimate for the maximal Lyapunov exponent.

Using this algorithm we obtained a maximal Lyapunov exponent of approximately 0.037 for this time series, which confirms the existence of spatio-temporal chaos (see [56, 55]).

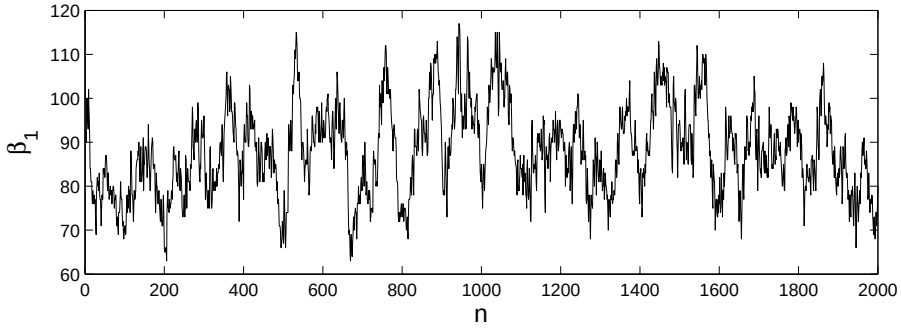

Figure 54: Plot of the time series $\{\beta_1(m) \mid m = 1, 2, \ldots, 2000\}$ of Betti numbers generated by the time blocks described above. This time series has a maximal Lyapunov exponent approximately equal to 0.037.

5.3 The FitzHugh-Nagumo Model

With the intuition developed in the previous example, we now turn to the 2-dimensional FitzHugh-Nagumo system

$$\begin{aligned} u_t &= \Delta u + \epsilon^{-1} u(1-u)(u - \tfrac{v+\gamma}{\alpha}) \\ v_t &= u^3 - v. \end{aligned} \tag{20}$$

on the rectangular domain $\Omega = [0, 80] \times [0, 80]$. We study (20) at $\alpha = 0.75$, $\gamma = 0.06$ and vary the parameter ϵ.

We numerically solved (20) using code of Barkley [2, 17, 3]. Again, dynamics of the patterns of the variable u is most easily observed by producing a movie of the thresholded data. Figure 55

shows some snapshots of such a movie at different values of the parameter ϵ. In particular, for $1/\epsilon \leq 12.5$ the movies indicate complicated spatial and temporal patterns.

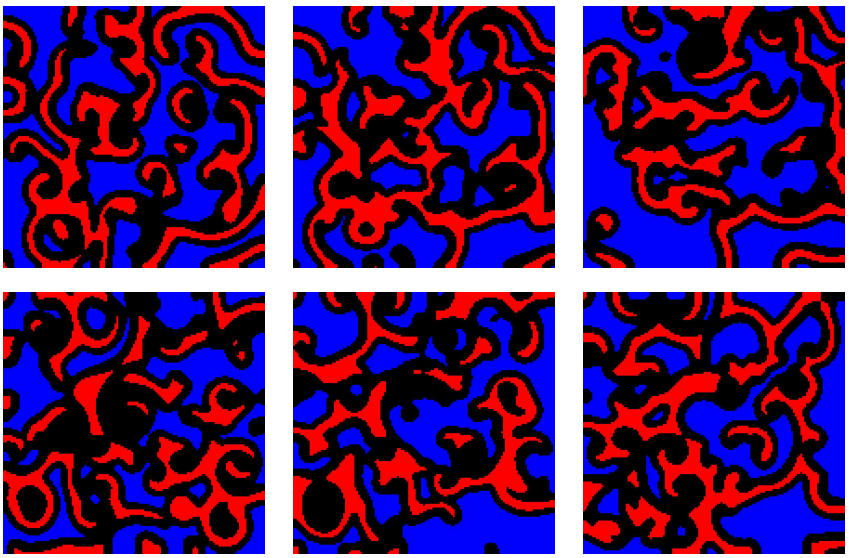

Figure 55: Wave patterns generated by (20). The light gray (red) region corresponds to excited points ($u \geq 0.9$), dark gray (blue) to the quiescent region ($u \leq 0.1$), and black to the reaction zone ($0.1 < u < 0.9$). The top row is for $1/\epsilon = 11.5$ and the bottom row is for $1/\epsilon = 12.0$.

For (20) the excited media is represented by $E = \{V_{i,j,k} \mid u(x_i, y_j, t_k) \geq 0.9\}$, and for each $V_{i,j,k} \in E$ we define the 3-dimensional cube $Q_{i,j,k} := [i, i+1] \times [j, j+1] \times [k, k+1]$. We then define the time block $T_{n,b}$ and the corresponding $\mathbb{T}_{n,b}$ similarly to what was done for (18).

5.3.1 Benchmark Results

The mathematical basis for the phase space reconstruction techniques in time series analysis is essentially Takens' embedding theorem [67, 63]. In this theorem the observable is assumed to be a smooth function. In our case the observables are the Betti numbers, which are integers, and so our observables are not even continuous. For this reason we feel that it is important to compare our approach against the following more standard Lyapunov exponent computation. We fixed (i, j) such that $(x_i, y_j) = (11.4286, 21.4286)$ and produced a time series $\{u(x_i, y_j, t_k) \mid k = 0, \ldots, K\}$. We obtained estimates for the maximal Lyapunov exponents as indicated in Figure 57. We obtained essentially the same result for several grid points (x_i, y_j).

From these computations we conclude that, for those values of ϵ at which the maximal Lyapunov

exponent is positive, (20) exhibits temporally chaotic dynamics. However, it is important to observe that this computation completely ignores the spatial complexity of this system.

5.3.2 Topological Results

Just as in the Gray-Scott model, we again produce a time series by computing the Betti numbers of various time blocks $\mathbb{T}_{n,b}$. More precisely, we computed $\{H_*(\mathbb{T}_{10(m-1),1000}) \mid m = 1, 2, \ldots, 10000\}$ and hence obtained the Betti numbers $\beta_i(m)$ for $H_i(\mathbb{T}_{10(m-1),1000})$.

Again $\beta_0(m)$ was piecewise constant taking on a limited number of fairly small values. Moreover, $\beta_2(m) \equiv 0$ so that there were no enclosed cavities in E. However, the time series $B_{(10,1000)} := \{\beta_1(m) \mid m = 1, 2, \ldots, 10000\}$ proved again to be chaotic. Typical plots are indicated in Figure 56.

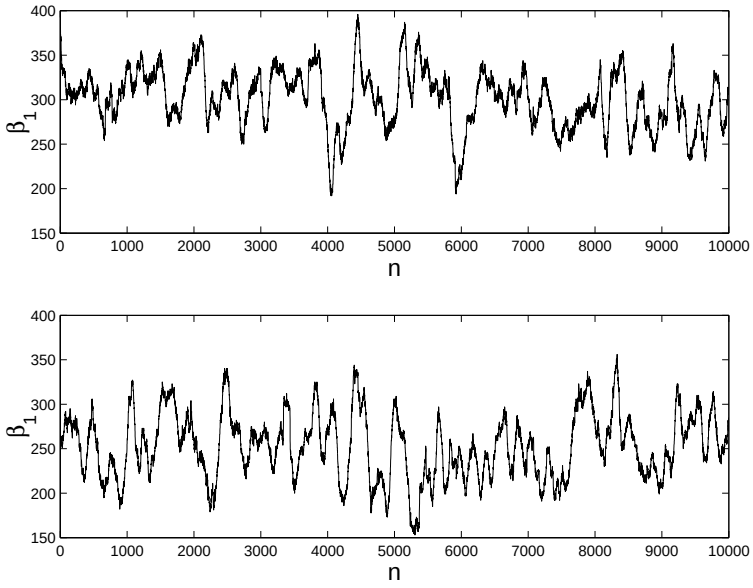

Figure 56: Plot of the time series $\{\beta_1(m) \mid m = 1, 2 \ldots, 10000\}$ of Betti numbers corresponding to the patterns in Figure 55. The top figure is for $1/\epsilon = 11.5$ and the bottom is for $1/\epsilon = 12.0$.

The first thing we can observe is that even though the patterns in Figure 55 seems to be very similar, the Betti numbers show striking differences. The mean values, for example, of the time series in Figure 56 differ.

We computed the maximal Lyapunov exponent for the time series $B_{(10,1000)}$. Figure 57 provides a plot of the maximal Lyapunov exponent as a function of $1/\epsilon$.

There are three important points to be made. The first is the near agreement between the ranges

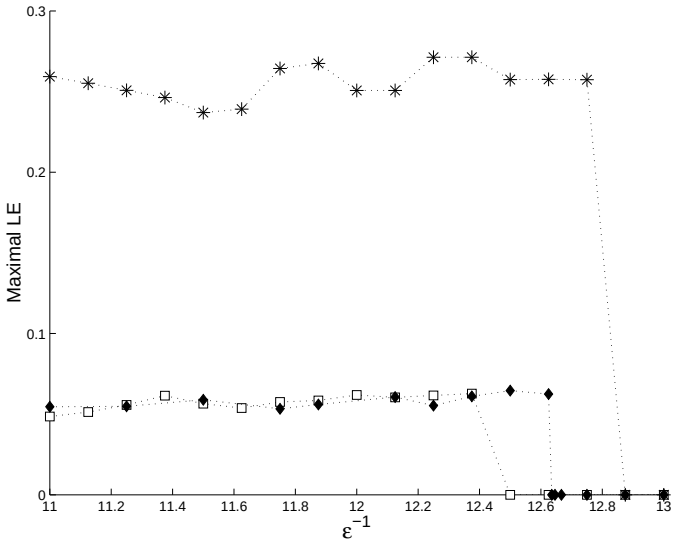

Figure 57: Maximal Lyapunov exponents, as a function of $1/\epsilon$, from the time series generated by fixing the point $(x_i, y_j) = (11.4286, 21.4286)$ in the domain and solving (20) for 30,000 time steps (stars). The diamonds and the squares are the Lyapunov exponents of time series of Betti numbers $B_{(10,1000)}$ computed using different initial conditions. For points where the Lyapunov exponent computation was not conclusive, the Lyapunov exponents were set to zero.

of ϵ on which the maximal Lyapunov exponents are positive and zero. This suggests that computing the Lyapunov exponent from homological data is an acceptable approach. The second is that we can now conclude that the system exhibits *spatial-temporal chaotic* behavior. This follows from the fact that this chaotic time series is defined in terms of the Betti numbers β_1, since $\beta_1(m) \neq 0$ implies that the topology of $T_{10(m-1),1000}$ is nontrivial and $\beta_1(m) \neq \beta_1(m')$ implies that the topology of $T_{10(m-1),1000}$ differs from that of $T_{10(m'-1),1000}$. The fact that the Lyapunov exponent from the homological data goes to zero sooner than that computed from a single point can be explained by the fact that the latter measures temporal chaos only and the homological data measures spatial structures as well. Thus it is possible that the spatial-temporal chaos disappears before the purely temporal chaos does. The third point is the observation that, as in the case of a fixed (x_i, y_i), the maximal Lyapunov exponent appears to be essentially constant as a function of $1/\epsilon$ until it drops to zero. This implies that Lyapunov exponents do not provide a useful measurement for characterizing the value of ϵ at which the simulation is being performed. On the other hand, plotting the average value of β_1, as is done in Figure 58, results in an almost monotone curve. Thus, in principle, by computing the average of the Betti numbers we can determine the parameter value ϵ of the simulation. Computing

the average of the Betti numbers is much cheaper than computing the maximal Lyapunov exponent, because, as is indicated in Figure 58, it can be computed with a shorter time series.

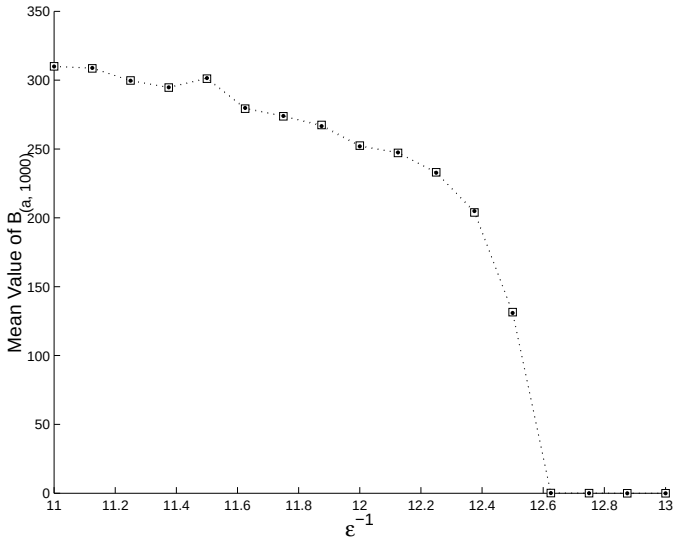

Figure 58: Mean values of the time series $B_{(10,1000)}$ used to compute the Lyapunov exponents in the top picture (squares), and the mean values of the time series $B_{100,1000} = \{\beta_1(m) \mid m = 1, 2, \ldots, 100\}$ (dots), as functions of $1/\epsilon$.

We also computed the entropies of the time series used to compute the Lyapunov exponents in Figure 57. The results are shown in Figure 59. The results are in agreement with the Lyapunov exponents computation. The entropies were computed by the method described in Chapter 3 using the 2-dimensional time series $\{(\beta_0(m), \beta_1(m)) \mid m = 1, 2, \ldots, 10{,}000\}$ for the Betti number time series and using the time series $\{u(t_k) \mid k = 1, 2, \ldots, 30{,}000\}$, where $u(t_k)$ represents the solution of (20) on the point (x_i, y_j) at time t_k. The fact that the Lyapunov exponents and the entropies of the time series of Betti numbers for the two initial conditions differ may be an indication of the existence of two attractors. The fact that there is a dip in entropy value may be an indication of a bifurcation.

5.4 Computational Comments

The above mentioned results depend upon the choice of a and b for the time blocks $T_{a(m-1),b}$. For the examples presented in this chapter, the choices $a = 300$ and $b = 10000$ for (18), and $a = 10$ and $b = 1000$ for (20) seem to be satisfactory. However, we cannot at this point in time suggest useful heuristics for a particular choice. The principal issues are as follows. If b is small, then β_1 is small.

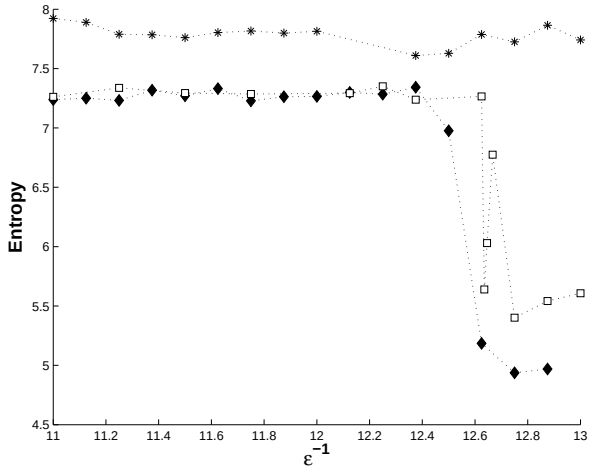

Figure 59: Entropy, as a function of $1/\epsilon$, from the time series generated by fixing the point $(x_i, y_j) = (11.4286, 21.4286)$ in the domain and solving (20) for 30,000 time steps (stars). The diamonds and the squares are the entropies of time series of Betti numbers $B_{(10,1000)}$ computed using different initial conditions. The entropies were computed using the same time series that were used to compute the Lyapunov exponents in Figure 57.

Since the Betti numbers are integers, this implies that we do not have enough significant figures to compute Lyapunov exponents. If b is large then the cost of computing $H_1(\mathbb{T}_{n,b})$ becomes impractical. Since the system is chaotic, choosing a too large results in decorrelation of subsequent Betti numbers. On the other hand, if a is too small the local change in the Betti numbers is insignificant. It should be noted that, for computing the mean value of the Betti numbers for (20), we were able to use $a = 100$ because strong correlation is not necessary.

The typical running time for generating one of the 10,000 points time series used in Figure 58 is about 12 CPU hours or 52 wall time hours in a Beowulf cluster with 30 Pentium 4, 2.4 GHz processors. On the other hand, each of the 100 points time series requires only 0.12 CPU hours or 0.5 wall time hours.

The numerical method used to solve (20) consists of a semi-implicit finite difference algorithm, on a equally spaced grid $\{(x_i, y_j) \mid i, j = 0, \ldots, N\}$ covering Ω. We used $N = 280$ in the computations of Lyapunov exponents for a fixed grid point (x_i, y_j), and $N = 140$ in all the other computations. This algorithm uses the fact that if the solution at a point (x_i, y_j) is small, it will remain small in the next step to speed up the algorithm. So there is a small numerical parameter δ such that

$u(x_i, y_j, t_{k+1}) = 0$ if $u(x_i, y_j, t_k) < \delta$. An implementation of this algorithm, EZ-Spiral, can be found at [3]. In this chapter we used a modified version of this program. We used $\delta = 10^{-4}$, and the time step $\Delta t = 0.0653$. Given the coarse grid (with $N = 140$) this method can not be guaranteed to accurately solve (20). On the other hand sample calculations at slightly finer grids did not result in qualitatively different results. In part this is due to the fact that homology is fairly robust with respect to small perturbations. Therefore, small numerical errors are not expected to lead to changes in the homology groups.

REFERENCES

[1] Arns, C. H., Knackstedt, M. A., Pinczewski, W. V., and Mecke, K. R., "Euler-Poincare characteristics of classes of disordered media," *Physical Review E*, vol. 63, no. 3, p. 031112, 2001.

[2] Barkley, D., "A model for fast computer simulation of waves in excitable media," *Physica D*, vol. 49, no. ?, pp. 61–70, 1991.

[3] Barkley, D., "EZ-Spiral: A code for simulating spiral waves." `http://www.maths.warwick.ac.uk/~barkley/`, 2002.

[4] Binder, K., "Kinetics of phase separation," in *Stochastic Nonlinear Systems* (Arnold, L., ed.), pp. 62–71, Berlin: Springer-Verlag, 1981.

[5] Blömker, D., Maier-Paape, S., and Wanner, T., "Spinodal decomposition for the Cahn-Hilliard-Cook equation," *Communications in Mathematical Physics*, vol. 223, no. 3, pp. 553–582, 2001.

[6] Busse, F. H., "The stability of finite amplitude cellular convection and its relation to an extremum principle," *J. Fluid Mech.*, vol. 30, no. 4, pp. 625–649, 1967.

[7] Cahn, J. W., "Free energy of a nonuniform system. II. Thermodynamic basis," *Journal of Chemical Physics*, vol. 30, pp. 1121–1124, 1959.

[8] Cahn, J. W., "Phase separation by spinodal decomposition in isotropic systems," *Journal of Chemical Physics*, vol. 42, pp. 93–99, 1965.

[9] Cahn, J. W., "Spinodal decomposition," *Transactions of the Metallurgical Society of AIME*, vol. 242, pp. 166–180, 1968.

[10] Cahn, J. W. and Hilliard, J. E., "Free energy of a nonuniform system I. Interfacial free energy," *Journal of Chemical Physics*, vol. 28, pp. 258–267, 1958.

[11] Cahn, J. W. and Hilliard, J. E., "Free energy of a nonuniform system III. Nucleation in a two-component incompressible fluid," *Journal of Chemical Physics*, vol. 31, pp. 688–699, 1959.

[12] Cerezo, A., Hetherington, M. G., Hyde, J. M., and Miller, M. K., "A topological approach to materials characterisation," *Scripta Metallurgica et Materialia*, vol. 25, pp. 1435–1440, 1991.

[13] Chandrasekhar, S., *Hydrodynamic and hydromagnetic stability*. The International Series of Monographs on Physics, Clarendon Press, Oxford, 1961.

[14] Cook, H., "Brownian motion in spinodal decomposition," *Acta Metallurgica*, vol. 18, pp. 297–306, 1970.

[15] Cormen, T. H., Leiserson, C. E., Rivest, R. L., and Stein, C., *Introduction to algorithms*. Cambridge, MA: MIT Press, second ed., 2001.

[16] Cross, M. C. and Hohenberg, P. C., "Pattern formation outside of equilibrium," *Rev. Modern Phys.*, vol. 65, no. 3, pp. 851–1112, 1993.

[17] Dowle, M., Mantel, R. M., and Barkley, D., "Fast simulations of waves in three-dimensional excitable media," *Internat. J. Bifur. Chaos Appl. Sci. Eng.*, vol. 7, no. 11, pp. 2529–2545, 1997.

[18] Ecke, R. E., Hu, Y., Mainieri, R., and Ahlers, G., "Excitation of spirals and chiral symmetry breaking in rayleigh-bénard convection," *Science*, vol. 269, no. 5231, pp. 1704–1707, 1995.

[19] Egolf, D. A., Melnikov, I. V., and Bodenschatz, E., "Importance of local pattern properties in spiral defect chaos," *Phys. Rev. Lett.*, vol. 80, no. 15, pp. 3228–3231, 1998.

[20] Egolf, D. A., Melnikov, I. V., Pesch, W., and Ecke, R. E., "Mechanisms of extensive spatiotemporal chaos in rayleigh-bénard convection," *Nature*, vol. 404, no. 6779, pp. 733–736, 2000.

[21] Frigo, M. and Johnson, S. G., "FFTW: An adaptive software architecture for the FFT," *Proc. ICASSP 1998*, vol. 3, pp. 1381–1384, 1998.

[22] Gameiro, M., Mischaikow, K., and Kalies, W., "Topological characterization of spatial-temporal chaos," *Phys. Rev. E*, vol. 70, no. 3, p. 035203, 2004.

[23] Gameiro, M., Mischaikow, K., and Wanner, T., "Evolution of pattern complexity in the cahn-hilliard theory of phase separation," *Acta Materialia*, vol. 53, no. 3, pp. 693–704, 2005.

[24] Garcke, H., Niethammer, B., Rumpf, M., and Weikard, U., "Transient coarsening behaviour in the Cahn-Hilliard model," *Acta Materialia*, vol. 51, no. 10, pp. 2823–2830, 2003.

[25] Golubitsky, M., Swift, J. W., and Knobloch, E., "Symmetries and pattern selection in rayleigh-benard convection," *Physica D*, vol. 10D, pp. 249–276, 1984.

[26] Hairer, E. and Wanner, G., *Solving Ordinary Differential Equations II*. Berlin: Springer-Verlag, 1991.

[27] Hegger, R., Kantz, H., and Schreiber, "TISEAN." `http://www.mpipks-dresden.mpg.de/~tisean/`, 2000.

[28] Hilfer, R., "Review on scale dependent characterization of the microstructure of porous media," *Transport in Porous Media*, vol. 46, no. 2-3, pp. 373–390, 2002.

[29] Hilliard, J. E., "Spinodal decomposition," in *Phase Transformations* (Aaronson, H. I., ed.), pp. 497–560, Metals Park, Ohio: American Society for Metals, 1970.

[30] Hyde, J. M., Miller, M. K., Hetherington, M. G., Cerezo, A., Smith, G. D. W., and Elliott, C. M., "Spinodal decomposition in Fe-Cr alloys: Experimental study at the atomic level and comparison with computer models — II. Development of domain size and composition amplitude," *Acta Metallurgica et Materialia*, vol. 43, pp. 3403–3413, 1995.

[31] Hyde, J. M., Miller, M. K., Hetherington, M. G., Cerezo, A., Smith, G. D. W., and Elliott, C. M., "Spinodal decomposition in Fe-Cr alloys: Experimental study at the atomic level and comparison with computer models — III. Development of morphology," *Acta Metallurgica et Materialia*, vol. 43, pp. 3415–3426, 1995.

[32] Ioannidis, M. A. and Chatzis, I., "On the geometry and topology of 3D stochastic porous media," *Journal of Colloid and Interface Science*, vol. 229, no. 2, pp. 323–334, 2000.

[33] Kaczynski, T., Mischaikow, K., and Mrozek, M., *Computational Homology*, vol. 157 of *Applied Mathematical Sciences*. New York: Springer-Verlag, 2004.

[34] Kalies, W., Mischaikow, K., and Watson, G., "Cubical approximation and computation of homology," *Conley Index Theory. Banach Center Publications*, vol. 47, pp. 115–131, 1999.

[35] Kalies, W. and Pilarczyk, P., "Computational homology program." `http://www.math.gatech.edu/~chom/`, 2004.

[36] Kantz, H. and Schreiber, T., *Nonlinear Time Series Analysis*, vol. 7 of *Cambridge Nonlinear Science Series*. Cambridge: Cambridge University Press, 1997.

[37] Keener, J. P., "Waves in excitable media," *SIAM J. Appl. Math.*, vol. 39, pp. 528–548, 1980.

[38] Keener, J. P. and Tyson, J. J., "Spiral waves in the belousov-zhabotinskii reaction," *Physica D*, vol. 21, pp. 307–324, 1986.

[39] Kong, T. Y. and Rosenfeld, A., "Digital topology. Introduction and survey," *Computer Vision, Graphics and Image Processing*, vol. 48, no. 3, pp. 357–393, 1989.

[40] Krinsky, V. and Pumir, A., "Models of defibrilation of cardiac tissue," *Chaos*, vol. 8, no. 1, pp. 188–203, 1998.

[41] Langer, J. S., "Theory of spinodal decomposition in alloys," *Annals of Physics*, vol. 65, pp. 53–86, 1971.

[42] Lessle, P., Dong, M., Soppa, E., and Schmauder, S., "Simulation of interpenetrating microstructures by self-consistent matricity models," *Scripta Materialia*, vol. 38, no. 9, pp. 1327–1332, 1998.

[43] Lessle, P., Dong, M., and Schmauder, S., "Self-consistent matricity model to simulate the mechanical behaviour of interpenetrating microstructures," *Computational Materials Science*, vol. 15, no. 4, pp. 455–465, 1999.

[44] Maier-Paape, S. and Wanner, T., "Spinodal decomposition for the Cahn-Hilliard equation in higher dimensions. Part I: Probability and wavelength estimate," *Communications in Mathematical Physics*, vol. 195, no. 2, pp. 435–464, 1998.

[45] Maier-Paape, S. and Wanner, T., "Spinodal decomposition for the Cahn-Hilliard equation in higher dimensions: Nonlinear dynamics," *Archive for Rational Mechanics and Analysis*, vol. 151, no. 3, pp. 187–219, 2000.

[46] Manneville, P., *Dissipative structures and weak turbulence*. Perspectives in Physics, Boston, MA: Academic Press Inc., 1990.

[47] Massey, W. S., *A basic course in algebraic topology*, vol. 127 of *Graduate Texts in Mathematics*. New York: Springer-Verlag, 1991.

[48] Mendoza, R., Alkemper, J., and Voorhees, P. W., "The topology of coarsened microstructures," in *Solidification Processes and Microstructures: A Symposium in Honor of Wilfried Kurz* (Rappaz, M., Beckermann, C., and Trivedi, R., eds.), pp. 123–129, TMS, 2004.

[49] Miller, M. K., Hyde, J. M., Hetherington, M. G., Cerezo, A., Smith, G. D. W., and Elliott, C. M., "Spinodal decomposition in Fe-Cr alloys: Experimental study at the atomic level and comparison with computer models — I. Introduction and methodology," *Acta Metallurgica et Materialia*, vol. 43, pp. 3385–3401, 1995.

[50] Mischaikow, K., Mrozek, M., and Pilarczyk, P., "Graph approach to the computation of the homology of continuous maps," *Preprint*, 2005.

[51] Morris, S. W., Bodenschatz, E., Cannell, D. S., and Ahlers, G., "Spiral defect chaos in large aspect ratio rayleigh-bénard convection," *Phys. Rev. Lett.*, vol. 71, no. 13, pp. 2026–2029, 1993.

[52] Morris, S. W., Bodenschatz, E., Cannell, D. S., and Ahlers, G., "The spatio-temporal structure of spiral-defect chaos," *Phys. D*, vol. 97, no. 1-3, pp. 164–179, 1996.

[53] Müller, S. C., Plesser, T., and Hess, B., "Two-dimensional spectrophotometry and pseudocolor representation of chemical patterns," *Naturwissenschaften*, vol. 73, pp. 165–179, 1986.

[54] Munkres, J. R., *Elements of algebraic topology*. Menlo Park, CA: Addison-Wesley Publishing Company, 1984.

[55] Nishiura, Y. and Ueyama, D., "Self-replication, self-destruction, and spatio-temporal chaos in the gray-scott model," *Forma*, vol. 15, pp. 281–289, 2000.

[56] Nishiura, Y. and Ueyama, D., "Spatio-temporal chaos for the gray-scott model," *Physica D*, vol. 150, pp. 137–162, 2001.

[57] Niyogi, P., Smale, S., and Weinberger, S., "Finding the homology of submanifolds with high confidence from random samples," *Preprint*, 2005.

[58] Paul, M., "Mark paul's web page." `http://www.me.vt.edu/mpaul/`, 2005.

[59] Pumir, A., Plaza, F., and Krinsky, V., "Effect of an externally applied electric field on excitation propagation in the cardiac muscle," *Chaos*, vol. 4, no. 3, pp. 547–555, 1994.

[60] Quarteroni, A. and Valli, A., *Numerical Approximation of Partial Differential Equations*. Berlin: Springer-Verlag, 1994.

[61] Sander, E. and Wanner, T., "Monte Carlo simulations for spinodal decomposition," *Journal of Statistical Physics*, vol. 95, no. 5–6, pp. 925–948, 1999.

[62] Sander, E. and Wanner, T., "Unexpectedly linear behavior for the Cahn-Hilliard equation," *SIAM Journal on Applied Mathematics*, vol. 60, no. 6, pp. 2182–2202, 2000.

[63] Sauer, T., Yorke, J. A., and Casdagli, M., "Embedology," *J. Statist. Phys.*, vol. 65, no. 3-4, pp. 579–616, 1991.

[64] Settles, G. S., *Schlieren and Shadowgraph Techniques*. Experimental Fluid Mechanics, New York: Springer-Verlag, 2001.

[65] Shardlow, T., "Numerical methods for stochastic parabolic PDEs," *Numerical Functional Analysis and Optimization*, vol. 20, no. 1-2, pp. 121–145, 1999.

[66] Spanier, E. H., *Algebraic topology*. New York: Springer-Verlag, 1981.

[67] Takens, F., "Detecting strange attractors in turbulence," in *Dynamical systems and turbulence, Warwick 1980 (Coventry, 1979/1980)*, vol. 898 of *Lecture Notes in Math.*, pp. 366–381, Berlin: Springer, 1981.

[68] Tyson, J. J., *A quantitative account of oscillations, bistability, and travelling waves in the Belousov-Zhabotinskii reaction*, pp. 92–144. New York: John Wiley, 1985.

[69] Tyson, J. J., Alexander, K. A., Manoranjan, V. S., and Murray, J. D., "Cyclic-amp waves during aggregation of *dictyostelium* amoebae," *Physica D*, vol. 34, pp. 193–207, 1989.

[70] Tyson, J. J. and Keener, J. P., "Singular perturbation theory of travelling waves in excitable media (a review)," *Physica D*, vol. 32, pp. 327–361, 1988.

[71] Ujihara, T. and Osamura, K., "Kinetic analysis of spinodal decomposition process in Fe-Cr alloys by small angle neutron scattering," *Acta Materialia*, vol. 48, no. 7, pp. 1629–1637, 2000.

[72] Wanner, T., "Maximum norms of random sums and transient pattern formation," *Transactions of the American Mathematical Society*, vol. 356, no. 6, pp. 2251–2279, 2004.

[73] Wei, J., "Existence, stability and metastability of point condensation patterns generated by the gray-scott system," *Nonlinearity*, vol. 12, pp. 593–616, 1999.

[74] Winfree, A. T., "Rotating chemical reactions," *Sci. Am.*, vol. 230, no. 6, pp. 82–95, 1974.

[75] Winfree, A. T., "Sudden cardiac death: a problem in topology," *Sci. Am.*, vol. 248, no. 5, pp. 144–161, 1983.

[76] Winfree, A. T., "The prehistory of the belousov-zhabotinskii oscillator," *J. Chem. Educ.*, vol. 61, pp. 661–663, 1984.

[77] Witowski, F., Leon, L., Penkoske, P., Giles, W., and M. Spano, W. Ditto, A. W., "Spatiotemporal evolution of ventricular fibrillation," *Nature*, vol. 392, pp. 78–82, 1998.

[78] Yamamoto, S. Y., Surko, C. M., Maple, M. B., and Pina, R. K., "Pulse propagation in the catalytic oxidation of carbon monoxide on platinum," *Phys. Rev. Lett.*, vol. 74, no. 20, pp. 4071–4074, 1995.

[79] Zykov, V. S., *Modelling of Wave Processes in Excitable Media*. Manchester: Manchester University Press, 1988.